Endoscopic Optical Imaging and Analysis of In-Cylinder Flow and Flame Propagation in Spark-Ignited Engines

Von der Fakultät für Ingenieurwissenschaften,
Abteilung Maschinenbau und Verfahrenstechnik der

Universität Duisburg-Essen

zur Erlangung des akademischen Grades

eines

Doktors der Ingenieurwissenschaften

Dr.-Ing.

genehmigte Dissertation

von

Syahar Shawal
aus
Penang, Malaysia

1. Gutachter: Univ.-Prof. Dr. Sebastian Kaiser
2. Gutachter: Univ.-Prof. Dr. Christof Schulz

Tag der mündlichen Prüfung: 05.07.2024

Declaration

I hereby declare that except where specific reference is made to the work of others, the contents of this dissertation are original and have not been submitted in whole or in part for consideration for any other degree or qualification in this, or any other university. This dissertation is the result of my work and includes nothing which is the outcome of work done in collaboration, except where specifically indicated in the text.

Syahar Shawal

2024

Acknowledgments

First and foremost, praise and thank God, for His showers of blessings throughout my research work to complete this thesis successfully. I extend my appreciation to the Malaysia Government for the provision of my Ph.D. scholarship.

I wish to express my profound and sincere appreciation to my supervisor, Univ.-Prof. Dr. Sebastian A. Kaiser. His guidance and the opportunity to be part of his research group at the Institute for Energy and Materials Processes (EMPI) - Reactive Fluids, University Duisburg-Essen, have been invaluable. His dynamic leadership, visionary approach, sincerity, and motivation have been truly inspirational. Under his tutelage, I acquired the methodology for conducting research and presenting its findings with clarity. Working and studying under his mentorship has been a privilege and an honour. I extend my gratitude to the management team of the EMPI, with a special mention to Professor Dr. Christof Schulz, the head of the Institute, for their support throughout my academic journey.

My heartfelt thanks go to my parents for their unwavering love, prayers, care, and sacrifices that have nurtured and prepared me for my future. To my wife, daughters, and son, I am deeply thankful for their love, understanding, prayers, and unwavering support that propelled me to complete this research. I also express my gratitude to my sisters and brothers for their support and invaluable prayers.

I would like to express my appreciation to my friends and research colleagues: Christian Meffert, Dr.-Ing Philipp Barth, Dr.-Ing Sebastian Wiemann, Dr. Daniel Fuhrmann, Dr.-Ing Patrick Kranz, Dr.-Ing Martin Goeschutz, Dr.-Ing Muhammad Ali Shahbaz, Kai Banke, and Dr.-Ing Niklas Jung, for their consistent encouragement and support. I extend special thanks to Natascha Schlösser, Jörg Albrecht, and Dieter Hermanns for their constant technical support and encouragement throughout this research. Lastly, my gratitude extends to all individuals who directly or indirectly supported me in accomplishing this research work.

Syahar Shawal, 2023

Summary

The flame propagation in different spark-ignited engines was recorded with various imaging systems via endoscopic and full optical access. Images for hundreds of consecutive combustion cycles were analysed together with pressure-derived heat release rates and mass fraction burnt (MFB) to obtain relationships between engine output and the physical properties associated with flame propagation. Combined crank-angle resolved imaging of flame propagation and cycle-resolved measurement of flow-field was performed to improve the understanding of the effects of bulk in-cylinder flow on spark and turbulent flame propagation behaviours.

The first part of the thesis describes the development of an algorithm with automatic dynamic thresholding to detect the line-of-sight projected flame boundary despite artifacts caused by the spark and the large dynamic range in image brightness across each time series. The unsupervised and computationally inexpensive algorithm segments a sequence of such images into three levels which correspond to spark, flame, and background. The main idea is to exploit the images' correlation in time to predict a suitable binarization threshold from the previous image, and the threshold is then corrected based on the now estimated foreground. The algorithm is adapted with a noise reduction model based on Fast Fourier Transformation (FFT) to minimize the existing periodic pattern noise from the high-speed CMOS detector. The algorithm was compared with two standard segmentation methods from the literature. Also, the robustness of the scheme was examined with a set of raw data images captured from various imaging systems and engines through endoscopic and full optical access.

The second part of the thesis compares selected imaging systems used to visualize flame propagation in engine cylinder via endoscopic and full optical access. This work investigates the image quality achievable with a large-aperture endoscope system and high-speed cameras in terms of detecting the premixed flame boundary in spark-ignited engines by chemiluminescence. The imaging systems compared here were cinematography with a CMOS camera, both with and without an intensifier, the latter variation being used in a four-cylinder automotive engine as well as in a single-cylinder motorcycle engine. A fundamental problem in evaluating the systems' efficacy is that it is not clear what constitutes "correct" detection of the flame boundary. To help clarify this question, the endoscopic results are compared among each other and to a "best-case scenario", which was

unintensified high-speed imaging with a large-aperture commercial camera lens in an engine with full optical access.

Finally, stroboscopic particle image velocimetry (PIV) and Mie-scattering imaging were conducted to map the velocity vectors of flow-field and to obtain 2-D planar details of the flame front on the vertical tumble plane that could not be identified by chemiluminescence imaging due to the projected line-of-sight nature of the latter technique. Combined high-speed flame chemiluminescence and double-frame PIV imaging were also conducted to study the relationship between flow field and turbulent flame growth.

Zusammenfassung

In verschiedenen Ottomotoren wurde die Flammenausbreitung mit verschiedenen Bildgebungssystemen über endoskopischen und voll-optischen Zugang aufgenommen. Die Bilder der turbulenten Flammenausbreitung für hunderte von aufeinanderfolgenden Verbrennungszyklen wurden zusammen mit aus dem Druck abgeleiteten Wärmefreisetzungsraten und Massenanteilverbrennungsprofilen (MFB) analysiert, um Beziehungen zwischen der Thermodynamik und den mit der Flammenausbreitung verbundenen physikalischen Eigenschaften zu erhalten. Es wurde eine kombinierte kurbelwinkelaufgelöste Abbildung der Flammenausbreitung und eine zyklusaufgelöste Messung des Strömungsfeldes durchgeführt, um die Auswirkungen der Massenströmung im Zylinder auf das Verhalten der Funken und der turbulenten Flammenausbreitung besser zu verstehen.

Der erste Teil der Arbeit beschreibt die Entwicklung eines Algorithmus mit automatischer dynamischer Schwellenwertbildung zur Erkennung der durch die Sichtlinie projizierten Flammengrenze trotz der durch den Funken verursachten Artefakte und des großen dynamischen Bereichs der Bildhelligkeit. Der Algorithmus ist unüberwacht und rechnerisch kostengünstig, um eine Sequenz solcher Bilder in drei Stufen zu segmentieren, die dem Funken, der Flamme und dem Hintergrund entsprechen. Die Flammenbilder wurden als Eingabe verwendet, um den Schwellenwert des Bildes auf der Grundlage eines Prädiktor-Korrektor-Schemas (PC) zu berechnen und vorherzusagen. Die Hauptidee besteht darin, die zeitliche Korrelation der Bilder auszunutzen, um einen geeigneten Binarisierungsschwellenwert aus dem vorherigen Bild vorherzusagen. Der Algorithmus wird mit einem Rauschunterdrückungsmodell auf der Grundlage der schnellen Fourier-Transformation (FFT) angepasst, um das vorhandene periodische Musterrauschen des Hochgeschwindigkeits-CMOS-Detektors zu minimieren. Der Algorithmus wurde mit zwei bekannten unterschiedlichen Methoden verglichen und deren Auswirkungen auf die Erkennung von Zeichen in Szenenbildern untersucht. Die Robustheit des Binarisierungsschemas wurde mit einem Satz von Rohdatenbildern untersucht, die von verschiedenen bildgebenden Systemen und Motoren durch endoskopischen und vollständigen optischen Zugang erfasst wurden.

Der zweite Teil der Arbeit beschreibt bildgebende Systeme, die zur Visualisierung der Flammenausbreitung im Motorzylinder durch endoskopischen und volloptischen Zugang verwendet

werden. In dieser Arbeit wird untersucht, welche Bildqualität mit einem Endoskopsystem mit großer Blende und Hochgeschwindigkeitskameras im Hinblick auf die Erkennung der vorgemischten Flammengrenze in funkengezündeten Motoren durch Chemilumineszenz erreicht werden kann. In der vorliegenden Arbeit wurden Hochgeschwindigkeitskamerasysteme zusammen mit dem Endoskopsystem in zwei Serienmotoren eingesetzt, um die zeitaufgelöste Flammenausbreitung zu quantifizieren. Bei den Systemen handelte es sich um Cinematographie mit einer CMOS-Kamera, sowohl mit als auch ohne Verstärker, wobei letztere Variante sowohl in einem Vierzylinder-Automotor als auch in einem Einzylinder-Motorradmotor eingesetzt wurde. Ein grundlegendes Problem bei der Bewertung der Wirksamkeit der Systeme besteht darin, dass nicht klar ist, was eine "korrekte" Erkennung der Flammengrenze ausmacht. Um diese Frage zu klären, werden die endoskopischen Ergebnisse untereinander und mit einem "Best-Case-Szenario" verglichen, bei dem es sich um eine nicht verstärkte Hochgeschwindigkeitsaufnahme mit einem handelsüblichen Kameraobjektiv mit großer Apertur in einem Motor mit vollem optischen Zugang handelt.

Im letzten Abschnitt wurden stroboskopische Particle Image Velocimetry (PIV) und Mie-Streuung durchgeführt, um die Geschwindigkeitsvektoren des Strömungsfeldes abzubilden und 2D-Details der Flammenfront auf der vertikalen Tumble-Ebene zu erhalten, die mit der Chemilumineszenz-Bildgebung aufgrund der projizierten Sichtlinie der letzteren Technik nicht identifiziert werden konnten. Es wurden auch kombinierte Hochgeschwindigkeits-Chemilumineszenz- und Doppelbild-PIV-Aufnahmen durchgeführt, um die Beziehung zwischen Strömungsfeld und turbulentem Flammenwachstum zu untersuchen.

Table of Contents

Declaration ii
Acknowledgments iii
Summary iv
Zusammenfassung vi
Table of Contents viii
Nomenclature 2
Chapter 1 Introduction 1
1.1 Motivation 1
1.2 Research objectives 4
1.3 Thesis outline 5
Chapter 2 Literature review 7
2.1 Background: Spark-ignition engines 7
2.1.1 Combustion process 7
2.1.2 Heat release analysis of cylinder pressure data 8
2.1.3 Cyclic variations in combustion 11
2.1.4 In-cylinder flow field 12
2.2 Engine combustion and flow diagnostics 14
2.2.1 Optical access to the combustion chamber 14
2.2.2 Chemiluminescence 19
2.2.3 Flame growth imaging 20
2.2.4 Particle-image velocimetry (PIV) 29
2.3 Image segmentation of flame propagation in SI engines 32
2.3.1 Image pre-processing 32
2.3.2 Thresholding 32
2.3.3 Edge detection 34
2.3.4 Image post-processing 36
2.4 Application of image segmentation in engine research 36
Chapter 3 Engine test bench with endoscopic access 38
3.1 Engine test facility 38
3.2 Endoscopic imaging system 40
3.2.1 Hybrid endoscope 42

3.2.2 Laser endoscope 43
Chapter 4 Automated flame detection: 'Predictor-corrector' scheme 44
4.1 Structure of image data sequence 45
4.2 General segmentation procedure 45
4.3 Filtering process 46
4.3.1 Spatial filtering 46
4.3.2 Frequency filtering 46
4.4 Predictor-corrector thresholding scheme (PC) 49
4.4.1 Working principle 49
4.5 Qualitative and quantitative results 52
4.5.1 Projected burnt area detection 52
4.5.2 Sensitivity analysis 55
4.6 Multi-level thresholding via forward and backward analysis 58
4.7 Algorithm robustness 60
4.7.1 Variation of camera and lens aperture 60
4.7.2 Comparison with existing edge detection schemes 62
Chapter 5 High-speed imaging of flame chemiluminescence using selected imaging systems via endoscopic and full optical access 65
5.1 Experimental setup 66
5.1.1 Engines 66
5.1.2 Imaging system 67
5.1.3 Pressure trace analysis 70
5.2 Results and discussion 70
5.2.1 Example images series 71
5.3 Quantitative results 77
5.3.1 Inter-experiment comparison 77
5.3.2 Projected burnt area, equivalent flame speed, and correlation with pressure-trace analysis for HS2 80
Chapter 6 Combined endoscopic phase-locked PIV and HS flame propagation imaging 85
6.1 Experimental setup 85
6.2 Cyclic variations and correlation with pressure-derived heat release 88
6.2.1 Mie-scattering for flame-front detection vs. high-speed chemiluminescence imaging 88
6.2.2 Correlation between flame propagation speed and pressure-derived mass burn function 92
6.3 Relationship between in-cylinder flow field and turbulent flame propagation 94
6.3.1 Flow-field vector calculation in PIVlab 94
6.3.2 Cycle-to-cycle variations of the in-cylinder flow-field 95
6.3.3 Impact of flow structure on spark arc and turbulent flame propagation 97
Chapter 7 Conclusions and outlook 103

7.1 Conclusions 103
7.2 Outlook 106
References 107
Author contributions 121

Nomenclature

AFR	-	Air fuel ratio
BDC	-	Bottom dead center
CA	-	Crank angle
CA5	-	Crank angle at which 5% mass fraction are burned
CCD	-	Charged-coupled device
CCV	-	Cycle-to-cycle variation
CL	-	Chemiluminescence
CMOS	-	Complementary metal oxide sensor
DISI	-	Direct injection spark ignition
FFT	-	Fast Fourier transformation
FPS	-	Frames per second
HCCI	-	Homogeneous charge compression ignition
IMEP	-	Indicated mean effective pressure
LOS	-	Line-of-sight
MFB	-	Mass fraction burned
PC	-	Predictor-corrector scheme
RoHR	-	Rate of heat release
SI	-	Spark ignited (or spark ignition)
TDC	-	Top dead center
VIS	-	Visible

Chapter 1 Introduction

1.1 Motivation

Improving the global efficiency of modern spark-ignited engines is one of the major concerns in automotive research. With strict CO_2 emissions regulation for passenger vehicles and customer demand for more efficient fuel consumption, automotive manufacturers have no option but to invest in R&D for powertrain systems. In December 2018, the EC, European Parliament and European Council finally reached an agreement to reduce CO_2 emissions by 37.5% by 2030 for new passenger cars and 31% for vans, compared to the current target of 95 grams per kilometre for 2021. Both types of vehicles will also be subject to a temporary CO_2 reduction target of 15% (14 grams per kilometre) by 2025, as shown in Figure 1.

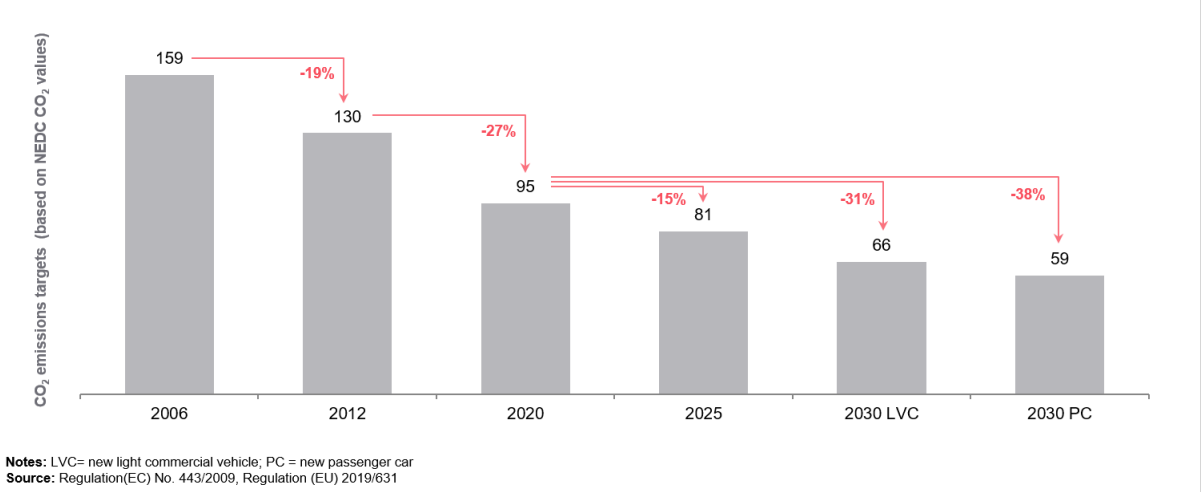

Figure 1: Development of the European emission target from 2006 to 2030. [1]

According to these standards, it is required for an automaker to not exceed a fleet average of 95 grams of CO_2 per kilometre. This emission regulation standard makes Electrical Vehicle (EV) popular as this mode of transportation is seen as capable to extensively reduce the greenhouse gas emissions produced by the transportation sector. Although electric vehicles (EVs) seem to be the future automotive technology, the current constraints such as battery technology (energy density), charging

infrastructure, and storage give the impression that this technology will not spread globally in the short term, especially in developing and third world countries [2, 3].

Researchers and engine manufacturers have been researching new technologies and methods in an effort to meet these stringent emissions targets. Advanced combustion technology such as homogeneous charge compression ignition (HCCI) has great potential for NO_x reduction and fuel consumption, with practically a similar performance as that of SI combustion [4, 5]. Advanced optical diagnostic techniques can help researchers and automotive engineers gain a deeper understanding of in-cylinder processes in internal combustion engines. In recent years, high-speed imaging technology has stimulated significant progress in imaging-based measurement techniques. This technique allows for detailed visualization of the event being studied by obtaining a series of image frames captured at high temporal and spatial resolution. The improved high-speed technology has encouraged researchers to discover and explore new and exciting insights into the underlying physical mechanisms of flow-related phenomena. In the field of engine research, high-speed imaging techniques have been widely used in optical research engines for various in-cylinder processes studies such as charge mixing, ignition, flame propagation, and soot particle formation to enhance the engine's efficiency and reduce particulate matter emission [6-12].

The development of imaging with high repetition rate gives opportunities to study in details ignition processes which bridges the gap between early and later combustion phases in engine. The utilization of high-speed imaging and image analysis methods in optical research engines has assisted the engine research and development, providing a detailed analysis of mixture formation, ignition, and combustion processes such as the occurrence of misfires and partial burn cycles [13-15]. These methods also have been used to investigate the effects of alternatives fuels in spark-ignition and compression-ignition engines [16, 17]. In fact, the current ignition and turbulent flame propagation models for simulation and modelling studies were verified with the data obtained from experimental works in optical research engines [10, 11, 18, 19].

Early flame-front propagation has been investigated in research engines with full optical access for quite some time. Ignition and early flame kernel (10-12°CAaIT) play important roles in determining the physical behaviour of fully-developed turbulent flame propagation in the engine cylinder. Their variations in terms of orientation, direction and location due to the effect of in-cylinder flow motion can lead to cycle-to-cycle variation in combustion process. Determining the correlation between spark stretching and flow motion (direction and velocity) can be a useful tool for identifying good and poor combustion cycles. This correlation then can be related to the thermodynamics properties of the engine cycle such as pressure curve, mass burned fraction (MBF), and indicated

mean effective pressure (IMEP). However, in research engines with large-scale optical access, less mechanical strength, reduced cooling, and altered thermal conductivity limit the operating range in speed and load. Furthermore, the in-cylinder flow, with its influence on flame wrinkling and convective flame displacement, can be different from a production engine due to modifications needed to create optical access, for example, greatly increased crevice volumes [20].

The emphasis in endoscopic access is on minimizing the impact on operating conditions, i.e., keeping thermodynamics, heat transfer, and speed/load range as close as possible to that of an all-metal engine. Therefore, engines with endoscopic access never yield the same degree of freedom in terms of optical diagnostics. Additionally, most endoscopes employed for in-cylinder imaging were not originally designed for such use but are essentially modified medical instruments. Their light-collection efficiency is modest and most cannot be used in the ultraviolet (UV). This limits their use to processes generating much detectable light like Mie scattering from sprays [21, 22] or flame luminosity and soot formation in Diesel engines [22-26]. Also demonstrated were two-colour visualization of soot luminosity to obtain the spatio-temporally resolved flame temperature [27, 28] and particle image velocimetry (PIV) [29]. These are all techniques that can rely on high levels of light in the visible spectrum. However, premixed combustion in spark-ignition (SI) engines emits relatively little light, much of it in the UV. Endoscopic access has been used to image SI combustion, for example, to reconstruct the three-dimensional movement of the flame [30], flame visualisation under very high thermal load in a racing engine [31], and more recently to identify pre-ignition kernels [32]. Each of these investigations met its goals, but the spatial resolution of the custom-built imaging systems was rather limited - maybe still best in Ref.[30], but the equipment was very specialized.

This study aims to contribute knowledge of diagnostics techniques for visualising and detecting premixed flame propagation in spark-ignited engines through chemiluminescence and laser-based techniques. The developed detection algorithm was applied on a different set of image data recorded from various imaging systems and engines. The sophisticated algorithm enables quantitative information to be extracted from a high-speed series of images, such as flame contour, flame area, and flame propagation speed. Together with the corresponding cycles' pressure traces, a wealth of detailed information on combustion can be acquired in little time. Analysis of flame structures and in-cylinder flow fields/turbulence can help explain engine performance and efficiency trends. The recent development of a now commercially available UV-transparent endoscope with relatively large aperture [33] enabled the detection of weak signals from premixed combustion [34] or laser-induced fluorescence in the UV [35] with the good resolution obtainable by off-the-shelf scientific cameras.

Using this endoscopic system in a production engine, in the present study we compare premixed "flame-front" detection via different detector options with measurements in an optical engine. The current work is based entirely on cinematographic CMOS high-speed imaging, both with and without an intensifier. The kHz repetition rate of CMOS camera systems enables following the flame development in each single cycle with sub-crank-angle temporal resolution.

However, CMOS cameras that are designed for these very high frame rates exhibit much more (and in some cases less repeatable) read-out noise than cameras based on CCDs or noise-optimized "slow" CMOS detectors. Similarly, image intensifiers for kHz repetition rates degrade image resolution, dynamic range, and photometric accuracy even more than their "slow" counterparts for applications with typical video rates of up to 100 Hz [36]. In view of these limitations that high-speed camera systems currently have, the present work explores how well premixed combustion imaging can be performed with the relatively small optical access granted by endoscopes.

1.2 Research objectives

The objectives of the experimental work conducted within the framework of this thesis were:

1. Develop a robust, and unsupervised image segmentation algorithm that enables the statistical analysis of combustion from endoscopic high-speed imaging.
2. Investigate the image quality achievable with a large-aperture endoscope system and high-speed cameras in terms of detecting the premixed flame boundary in spark-ignition engines by chemiluminescence imaging.
3. Investigate the influence of the in-cylinder flow field on the spark channel, early flame kernel formation, and turbulent flame propagation in a production engine through endoscopic access.

1.3 Thesis outline

In addition to Chapter 1, this thesis consists of six chapters:

Chapter 2 - A literature review that covers the fundamental concepts of combustion and turbulent flow in spark ignition engines. The focus is placed on optical diagnostic methods, and instrumentation for visualizing the turbulent flow field and premixed combustion in spark-ignition engines. This chapter provides a comprehensive discussion of experimental findings from the literature concerning the impact of turbulent flow on ignition and turbulent flame propagation. Additionally, this chapter explores image thresholding and segmentation, along with their associated challenges and limitations.

Chapter 3 - This chapter presents a description of the BMW engine test bench at the EMPI, University of Duisburg-Essen. It outlines the primary engine modifications undertaken to establish additional ports for optical access. The chapter also provides a detailed explanation of the endoscopes employed in the experiments as diagnostic tools for image detection, as well as the optics involved in laser-sheet formation. Moreover, the instrumentation employed for data acquisition, such as in-cylinder pressure and temperature, is described.

Chapter 4 - This chapter offers an in-depth description of the novel binarization algorithm for detecting flame boundaries. It introduces the general image processing procedures and fundamental principles of thresholding methods with reference to the MATLAB programming language. The algorithm is subsequently subjected to testing across a wide spectrum of image qualities to assess its robustness. Additionally, the algorithm's reliability is evaluated by comparing it to other edge detection techniques.

Chapter 5 - Within this chapter, the endoscopic high-speed imaging of flame propagation using various imaging systems is discussed and compared to those images acquired through the large optical access in a research engine. The image quality in terms of flame detection from these high-speed imaging systems is discussed. The spatial information of flame propagation is then extracted through binarization for combustion and correlation analysis.

Chapter 6 – This chapter presents a combined measurement of flow field and flame propagation in a production engine through endoscopic access. It details the integration and utilization of phase-locked particle image velocimetry (PIV) and high-speed broadband flame chemiluminescence detection. Combustion cycles recorded are categorized into 'fast' and 'slow' cycles based on their CA10. The evaluation of two-dimensional flow velocity is conducted through mean-averaged analysis with subsequent discussion on cyclic variations in combustion and flow fields. Correlation between flow

structure, and turbulent flame speed is established and presented. The chapter also delves into endoscopic flame detection using line-of-sight and laser-sheet techniques.

Chapter 7- The conclusions of the current work are summarized, together with recommendations for future studies.

Chapter 2 Literature review

This chapter covers the fundamental concepts of combustion and turbulent flow in spark-ignition engines. The focus is placed on optical diagnostic methods, and instrumentation for visualizing the turbulent flow field and premixed combustion flame in spark-ignition engines. This chapter provides a comprehensive discussion of experimental findings from the literature concerning the impact of turbulent flow on ignition, and turbulent flame propagation. Additionally, this chapter discusses the potential of passive and active diagnostic techniques in obtaining valuable optical insights into in-cylinder flow behaviour and flame front propagation. Furthermore, it explores image thresholding and segmentation, along with their associated challenges and limitations.

2.1 Background: Spark-ignition engines

2.1.1 Combustion process

Combustion of the fuel/air mixture, which takes place in the engine cylinder, is one of the processes that controls engine power, efficiency, and emissions. In port fuel injection (PFI) engines, the fuel is mixed with air in the engine's intake system. The air/fuel mixture is compressed by piston movement upwards and the electric discharge from the spark plug initiates combustion. The ignition process, which takes place at the end of the compression stroke, initially forms a laminar flame kernel, transferring thermal energy to the unburned mixture regions. This develops into a turbulent flame, which spreads in a spherical shape until it reaches the combustion chamber walls on the piston and the cylinder head.

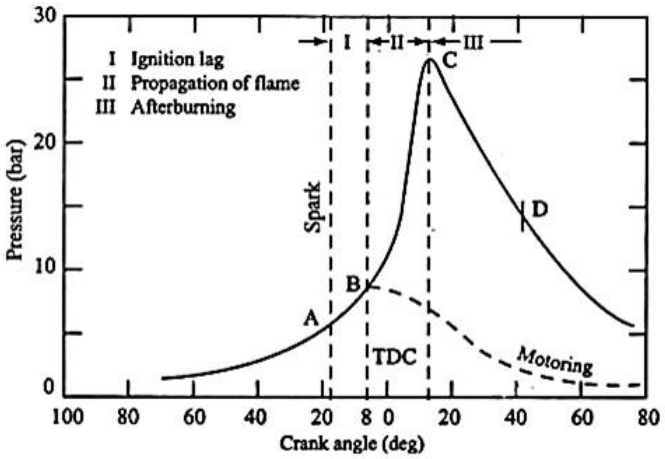

Figure 2: Combustion phases in spark-ignition engine. [37]

The combustion process in spark-ignition engines can be divided into three stages and can be illustrated as in Figure 2: ignition and early flame kernel development stage (A-B), turbulent flame propagation stage (B-C), and flame termination stage (C-D) [37, 38].

Stage A-B: The air/fuel mixture in the combustion chamber is ignited by the spark plug at the end of the compression stroke. The spark creates a high-energy plasma kernel that ignites the surrounding mixture. After ignition, a small flame kernel is formed near the spark plug electrode. The flame kernel rapidly expands outward from the ignition source due to the high pressure and temperature in the combustion chamber. It ignites the adjacent air-fuel mixture, initiating the combustion process.

Stage B-C: As the flame kernel expands, it forms a flame front that propagates through the remaining unburned mixture. Turbulent flow in the combustion chamber enhances the flame propagation by continuously mixing fresh mixture with the burned gases, promoting rapid combustion. The flame front experiences wrinkling and folding due to the turbulent flow. These wrinkles increase the flame surface area, promoting faster combustion and heat release.

Stage C-D: In this stage, the turbulent flame front reaches the combustion chamber walls, where it interacts with the surfaces and gradually extinguishes (flame quenching). The combustion process is considered complete when the flame front has consumed the available fuel-air mixture.

2.1.2 Heat release analysis of cylinder pressure data

The pressure trace analysis is primarily used to characterize the combustion process in an engine. The recorded pressure traces are used to obtain the combustion rate information and also as an indicator for cyclic variability of engine combustion. The simplest approach to evaluate this important parameter is by performing single-zone heat release analysis which is based on 1st law of

thermodynamics [39, 40]. As shown in Figure 3, the combustion chamber system is considered a closed system when both the inlet and exhaust valves are closed (i.e., for compression, combustion, and expansion).

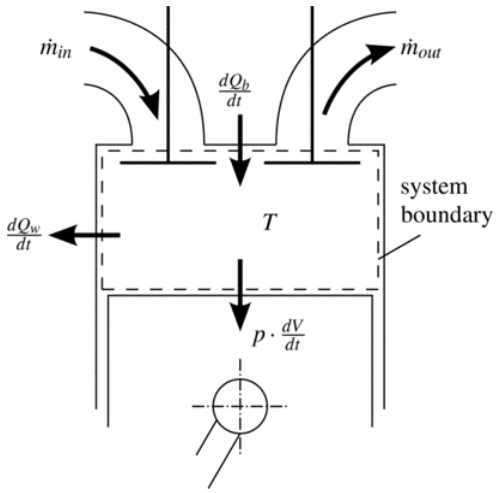

Figure 3: Schematic diagram of energy balance in an engine. [38]

The energy equation for the above process is written as:

$$\frac{dQ_b}{dt} - \frac{dQ_w}{dt} = \frac{dU}{dt} + \frac{dW}{dt} \tag{2.1}$$

where $\frac{dQ_b}{dt}$ denotes the heat generated by fuel through combustion process, $\frac{dQ_w}{dt}$ represents heat transferred to walls by means of in-cylinder gasses, $\frac{dU}{dt}$ describes the change in internal energy of the system while $\frac{dW}{dt}$ gives the rate of work transferred from the system.

Upon derivation and neglecting mass flow into the crevice, the heat release rate (HRR) based on a zero-dimensional single-zone model is written as:

$$\frac{dQ_b}{dt} = \frac{\gamma}{\gamma - 1} p \frac{dV}{dt} + \frac{1}{\gamma - 1} V \frac{dp}{dt} + \frac{dQ_w}{dt} \tag{2.2}$$

where the term $\frac{dQ_b}{dt}$ represents the gross heat release rate, p the cylinder gas pressure, t crank angle, V the instantaneous volume, and gamma, γ is the ratio of specific heats. For gasoline fuel at an equivalence ratio of ϕ =1, a linear function of the mean charge temperature for a specific heat ratio is expressed as [40-42]:

$$\gamma(T) = 1.345 - (4.78 \text{ x } 10^{-5}) * T \tag{2.3}$$

where the mean charge temperature, T in Kelvin (K).

The term $\frac{dQ_w}{dt}$ represents the convective heat transfer rate to the combustion chamber walls and is expressed as:

$$\frac{dQ_w}{dt} = Ah_c(T - T_w) \tag{2.4}$$

where A is the chamber surface area, T is the mean gas temperature based on ideal gas law, T_w is the mean wall temperature, and h_c is the heat transfer coefficient and is determined by Woschni's correlation as Ref.[43]:

$$h_c = 3.26D^{-0.2}p^{0.8}T^{-0.55}w^{0.8} \tag{2.5}$$

where D is the cylinder bore taken as the characteristic length and w is a local average gas velocity in the cylinder. The average cylinder gas velocity (m/s) determined for a four-stroke, water-cooled engine without swirl is expressed as:

$$w = C_1\bar{S} + C_2\frac{V_dT_r}{p_rV_r}(p - p_m) \tag{2.6}$$

where V_d is the displacement volume, p is the instantaneous cylinder pressure, p_r, V_r, T_r are the working fluid pressure, volume, and temperature at inlet valve closing, and p_m is the motored cylinder pressure as the same crank angle as p.

For the gas exchange period: $C_1 = 6.18$, $C_2 = 0$

For the compression period: $C_1 = 2.28$, $C_2 = 0$

For the combustion and expansion process: $C_1 = 2.28$, $C_2 = 3.24 \times 10^{-3}$

The Combustion Heat Release (CHR) is obtained from the integral of the HRR curve:

$$CHR = \int_{\theta=IVO}^{\theta=IVC}(HRR)d\theta \tag{2.7}$$

where IVO is the open intake valve and IVC is the closed intake valve.

The Mass Fraction Burned (MFB) is the normalized integral of the heat release rate:

$$MFB = \frac{\int_{\theta=IVO}^{\theta=IVC}(HRR)d\theta}{m_fQ_{LHV}\eta_c} \tag{2.8}$$

where m_f is the mass of fuel, Q_{LHV} is the lower heating value of fuel, and η_c is the combustion efficiency.

2.1.3 Cyclic variations in combustion

The variations in in-cylinder peak pressure, indicated mean effective pressure (IMEP), and combustion duration of individual cycles have been recognized as indicators of cycle-to-cycle variations (CCV) in SI engines [38, 39].

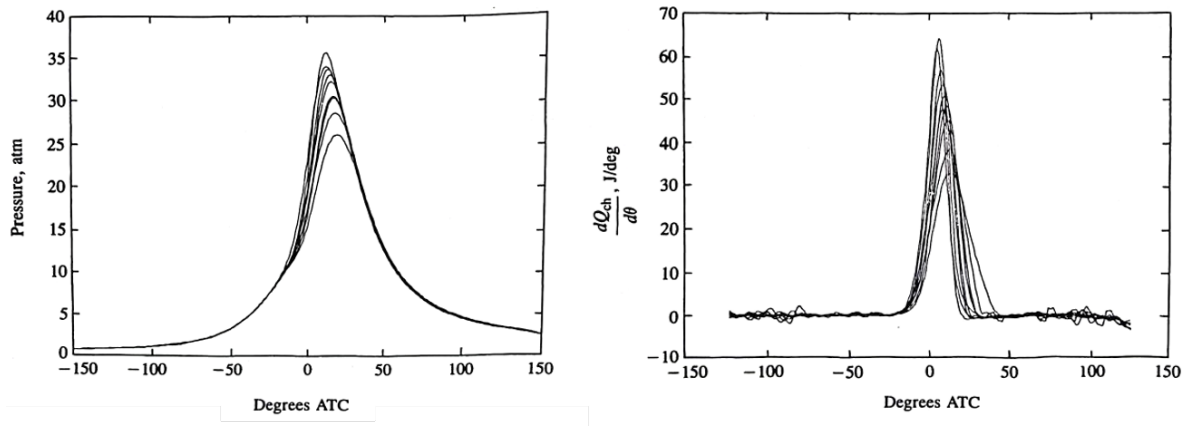

Figure 4: Cyclic variation in cylinder pressure (left) and in gross heat release (right). [39]

The cyclic variability is contributed by the random fluctuations in equivalence ratio and flow field due to the turbulent nature of the flow in the cylinder. These spatio-temporal fluctuations contribute to an inhomogeneous mixing of air and fuel, random convection of the spark kernel away from the electrodes, variation in flame kernel position, and these subsequently cause variation in the turbulent flame growth rate [44, 45]. Variations in the combustion duration revealed that some cycles have a faster combustion process than others.

Keck et al. [46] suggested that cycle-to-cycle variations in the growth rate and location of the flame kernel at very early times are the major cause of cycle-to-cycle pressure variations in spark-ignition engines.

Aleiferis et al. [47] studied the cyclic combustion variations and air/fuel ratio of the reacting mixture in a lean-burn research engine. The OH and CH chemiluminescence signals were measured and used to evaluate the in-cylinder equivalence ratio of the mixture and examine its contribution to the flame growth speed and the cyclic variability in the crank angle by which 5% of the fuel mass was burned (CA5). It was found that the in-cylinder equivalence ratio of the mixture exhibited large variations on a cycle-to-cycle basis and consistently produced negative correlation coefficients with the CA5. In another study, Aleiferis et al. [48] investigated the effects of initial flame kernel growth on the cyclic variability of IMEP and CA5. The results showed large cycle-to-cycle variations in flame size, shape,

and location. The projected burnt areas at 40°CA after ignition timing was found to correlate with coefficients as high as -0.96 with crank angle of 5% mass fraction burned and 0.85 with IMEP.

2.1.4 In-cylinder flow field

In spark-ignition engines, fuel and oxidizer are mixed by turbulence in a period before the electrical spark ignites the mixture. Turbulent flows enhance the rate of mixing compared to molecular diffusion as a result of local fluctuations in the flow field. In the engine cylinder, the flow undergoes a complicated combination of turbulent shear layers, recirculating regions, and boundary layers that cause unsteady turbulent flow and may exhibit substantial cycle-to-cycle fluctuations [38]. In-cylinder flows are highly influenced by orientation of intake, shape of combustion chamber (pent roof), engine speed, etc. [38, 49].

In a steady turbulent flow, the instantaneous local fluid velocity, U is decomposed into two components, a mean velocity component and a fluctuating component. This technique is referred to as the Reynolds decomposition, as shown in Figure 5. Thus, the instantaneous velocity, U is written as:

$$U(t) = \overline{U} + u'(t) \tag{2.9}$$

where t is time, the mean velocity, $\overline{U}$ is the time average of $U(t)$, and $u'(t)$ is the fluctuating component.

$$\overline{U} = \frac{1}{\Delta t}\int U(t)dt \tag{2.10}$$

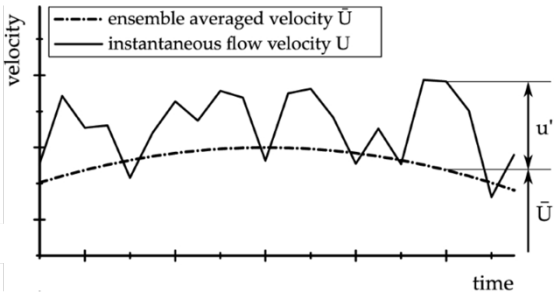

Figure 5: Definition of steady turbulent flow by average velocity $\bar{U}$ and a fluctuation velocity *u'*. [50]

However, in IC engines, the mean velocity of the flow at any point in the cycle, as well as turbulent fluctuations about that specific cycle's mean flow varies from cycle to cycle. Hence, the application of Reynolds decomposition can lead to an error. Another approach used in quasi-periodic flow is ensemble-averaging (EA) or phase-averaging.

The instantaneous velocity for crank-angle position θ in a particular cycle i is written as:

$$U(\theta,i) = \bar{U}(\theta,i) + u'(\theta,i) \tag{2.11}$$

Where $\bar{U}(\theta,i)$ and $u'(\theta,i)$ are the mean and fluctuating velocity components. By taking into account the cyclic variations, the ensemble-averaged velocity at the same crank angle position is calculated as:

$$\bar{U}_{EA}(\theta) = \frac{1}{N}\sum_{i=1}^{N} U(\theta,i) \tag{2.12}$$

Where N is the number of cycles in dataset.

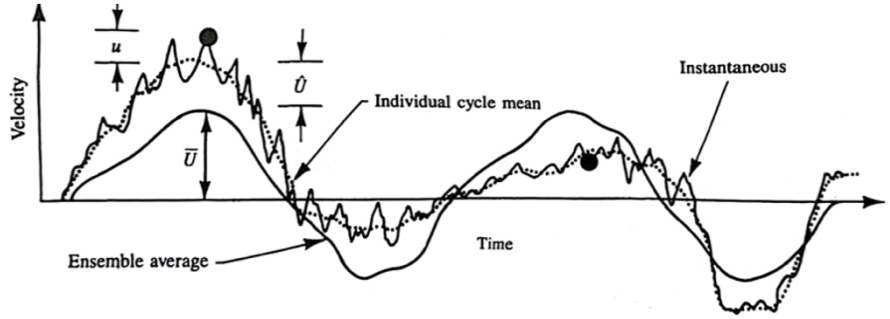

Figure 6: Velocity variation at a crank-angle position in the cylinder. Dots indicate measurements of instantaneous velocity at the same crank angle. Ensemble-averaged velocities obtained by averaging over a number of cycles are shown as a solid smooth line. [38]

The difference between the mean velocity in a particular cycle and the ensemble-averaged velocity over many cycles is defined as the cyclic variation in mean velocity:

$$\hat{U}(\theta,i) = \bar{U}(\theta,i) - \bar{U}_{\mathrm{EA}}(\theta) \tag{2.13}$$

The instantaneous velocity in E2.12 can be written as three components as shown in Figure 6.

$$U(\theta,i) = \bar{U}_{\mathrm{EA}}(\theta) + \hat{U}(\theta,i) + u'(\theta,i) \tag{2.14}$$

Researchers have shown that tumble-generated flow and high turbulence intensity provide a strong influence on the turbulent kinetic energy and subsequently increase flame kernel growth, flame propagation speed, and reduce the combustion period [20, 51, 52]. Le Coz et al. [53] studied the influence of large-scale (low-frequency velocity) and small-scale (high-frequency velocity) turbulent flow fields on the cyclic variations of the initial flame at the time from ignition to the 5% mass burned fraction. The study showed that the cyclic variations of large-scale fluid motion in the electrode gap mainly contribute to the cycle-to-cycle variations of the early combustion phase. However, the wrinkling by small-scale turbulence only accelerates the combustion process during the propagation phase. Aleiferis et al. [54] performed an optical study in a research engine to investigate the effect of

large-scale flame distortion, as well as small-scale wrinkling on the subsequent timing of 5% mass fraction burned on a cycle-to-cycle basis. It was suggested that on the tumbling plane of the flow, a high convection velocity was preferable up to 30°CA after ignition timing. The recorded images showed that the flame always preserved its shape while propagating, even if it had been initiated with a highly convoluted shape. The study also showed a strong correlation between the flame growth rate and the crank angle of 5% mass fraction burned. Le et al. [55] showed that flame propagation is strongly influenced by the general flow field and large-scale eddies, which can enhance and guide the flame propagation.

Some studies have shown that the in-cylinder flow near the spark plug correlates with the early flame growth rate, which indicates that stronger flow promotes shorter combustion duration. Optical diagnostics in research optical engines have shown that strong tumble flow in the vicinity of the spark plug at the time of ignition causes the plasma arc to stretch [10, 56-58]. However, all these studies were performed in research engines with large optical access in which the influence of tumble flow on flame wrinkling and convective flame displacement could be different from a production engine due to the modifications needed to create optical access [59]. Although many efforts have been made to identify the relations between in-cylinder flow field and the combustion process, most of these studies only present correlation findings based on a few selected cycles and are not exhaustive. There is still a research gap related to the correlation between flow field and flame propagation parameters such as flame centroids position and flame growth rate, especially in a realistic production engine environment.

2.2 Engine combustion and flow diagnostics

2.2.1 Optical access to the combustion chamber

Optical access to the combustion chamber is required to enable the investigation of in-cylinder flow and combustion phenomena through optical techniques. The passive measurements, i.e., combustion flame visualization through the combustion chamber sufficiently require one optical access. However, for active measurements, i.e., laser-based optical techniques, at least two optical accesses are required for camera detection and laser beam respectively. In single-cylinder research engines, the full optical access to the combustion chamber is created either through the top (cylinder head), bottom (piston crown), or side (glass liner) of the engine. On the other hand, minimum modification is made on a production engine to create optical access through an endoscopic system or fiber optic system.

Optical research engine

Research engines with large optical access allow a complete view of the entire combustion chamber from different views. The optical access has enabled complex qualitative and quantitative non-intrusive measurements to study in-cylinder processes such as mixing process, fluids flow, combustion, and emission phenomena [48, 54, 60]. The main advantages of this design features are it allow a wide range of diagnostics to be applied and provide maximum possible illumination at the test section for imaging-based measurement techniques. However, typically optical engines are designed to operate at low to medium-range speed and torque. A large modification on engine cylinder to provide maximum optical access to the combustion chamber has a significant impact on engine combustion characteristics [61]. The reason for this is that the thermal conductivity of quartz or sapphire is lower than metal. The differences in thermal conductivity can lead to significant differences in engine heat transfer characteristics. Moreover, optical engines typically have very large crevices volumes which allows flames to actively burn within the piston crevice [62]. Therefore, optical engines are not considered to be fully representative of all-metal production engines. A comprehensive study of the differences between optical and all-metal engines was carried out in [59].

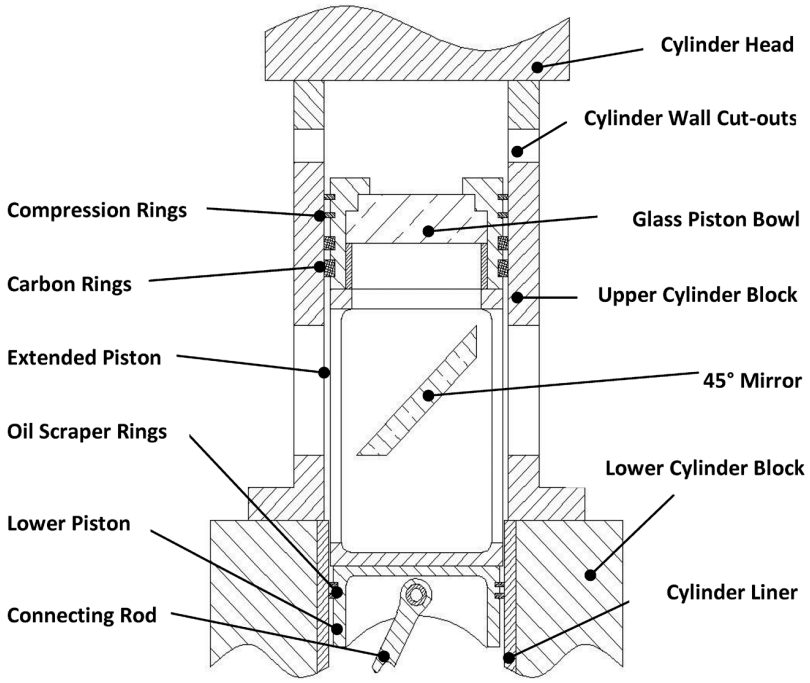

Figure 7: An optical research engine with an extended piston. [63]

Endoscope

Endoscopic access to the combustion chamber enables powerful optical diagnostic applications with minimum modifications to the engine, reducing the impact on operating conditions, i.e., keeping thermodynamics, heat transfer, and speed/load range as close as possible to that of an all-metal engine. A typical diameter for an endoscope is from 7 mm to 10 mm and it provides a much higher optical resolution compared to the optical fibres. In the past, the application of traditional endoscopes in engine diagnostics have been used for visualizing in-cylinder phenomena such as mixing process, and combustion flame [29, 64-66]. The use of rigid endoscope, called borescope, for 2D-PIV measurement in the field of combustion engine is found in Ref.[29]. The 8-mm diameter endoscope, as shown in Figure 8 was a rod lens system. The fiber bundle that used for illumination purposes was removed to allow the use of rod lenses with a 6 mm diameter instead of 4.5 mm. This modification increases the light collection by a factor of 1.7.

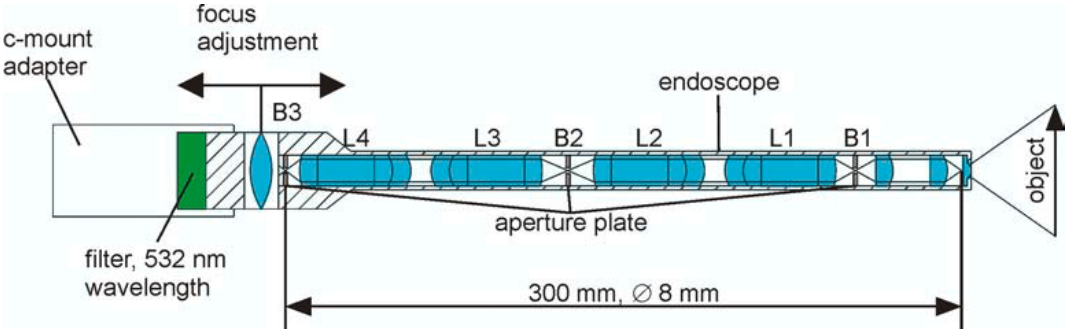

Figure 8: Modified rod lens borescope used for PIV measurement in Ref.[29].

One of the endoscopes that has been widely used in the field of combustion and flow field imaging is the camera endoscope produced by LaVision. The 8-mm diameter camera endoscope is designed for the visible spectral range (VIS) and provides relatively low light-collection efficiency with the equivalent f-number 14.8. Most of researchers utilized this endoscope system to perform Particle Velocimetry Image (PIV) in research engines. [29, 51, 67, 68]

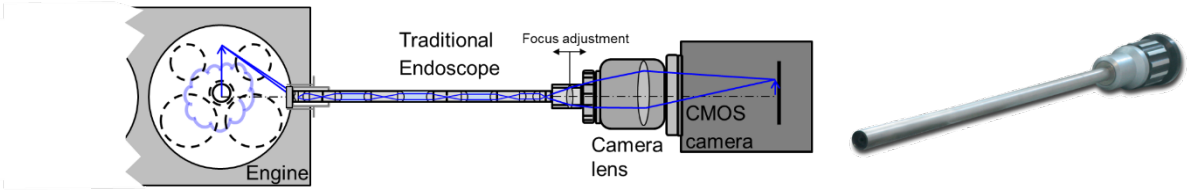

Figure 9: LaVision traditional VIS endoscope. [69]

Another commercial video endoscopes, known as AVL Visioscope are originally designed by Karl Storz, a medical endoscope manufacturer. The Visioscope has two diameters, 7 mm and 4 mm with

the angle of view of 67°, as shown in Figure 10. The Visioscope offers modest light-collection efficiency with F/7 and is more sensitive in visible and near infrared (NIR) spectrum range. Therefore, they are mostly used to visualize the fuel spray formation, and evaluation of two-colour pyrometry flame temperature and soot concentration (KL factor) in Diesel engines [70-72].

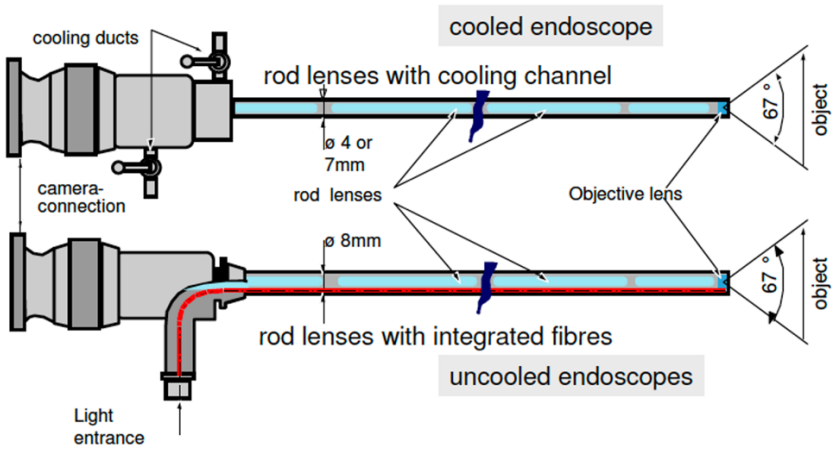

Figure 10: AVL Visioscope (Karl Storz). [73]

However, most endoscopes employed in these experiments were not originally designed for such use but are essentially modified medical instruments. Their light-collection efficiency is modest (large F-number) and most cannot be used in the ultraviolet (UV). Additionally, this typical endoscope was directly mounted to detector which can be exposed to the engine vibration during measurements.

Recent development of large-aperture hybrid endoscope, as shown in Figure 11, has significantly improved light collection efficiency with the equivalent F/4.5 Nikon's UV-Nikkor lens and optical resolution with minimum vignetting and distortion effects [34, 35], especially in UV emission spectrum [33]. The 10-mm diameter hybrid endoscope was developed as a result of collaboration work between two organizations, the Institute for Technical Optics (ITO) of the University of Stuttgart, the Institute for Energy and Materials Processes (EMPI) of the University of Duisburg-Essen (UDE), and later commercialised by LaVision GmbH, Göttingen. The main motivation for the development was due to the limited number of available compact UV endoscopes specifically designed for engine applications [74]. The endoscope system was designed to enable the detection of weak processes, mainly in UV spectrum range such as UV fuel-tracer laser-induced fluorescence (LIF) measurements. The endoscope system utilizes a two-stage concept which allows some relative movement between the access optics and relay optics. A front endoscope is mounted directly in the engine, creating an intermediate image on a field lens. A relay optic, isolated from the vibrations of the engine, projecting this intermediate image onto the camera. For imaging in the UV, the relay optic

can be a hybrid refractive-diffractive optical element (R-DOE), an expensive customized optical component that corrects chromatic aberration and has a narrow-band single wavelength. This system was utilized in the previous studies which covers gas-phase temperature imaging using tracer LIF [75-78], and flame propagation imaging [34] in a near production engine. Another possible relay lens that can be integrated with the access optics is a commercial UV objective lens. The usage of the commercial UV camera lenses improved image resolution and limited the chromatic aberration over larger wavelength range [79]. The system was recently used to visualize the fuel films and soot formation through LIF and natural incandescence in a single-cylinder direct injection spark ignition (DISI) engine [80].

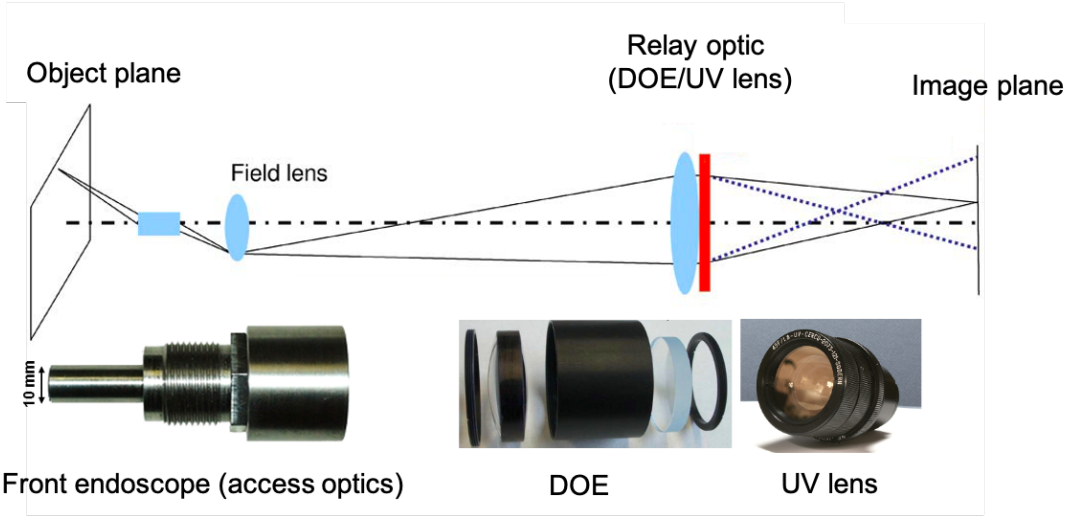

Figure 11: Hybrid UV endoscope. [74]

Table 1: Various endoscope specification.

Features	**Hybrid endoscope (Institute for Energy and Materials Processes, EMPI-University of Duisburg-Essen)**	**Traditional endoscope (Lavision/ AVL-Karl Storz)**
Diameter	10 mm	8 mm / 7 mm
Length	~77 mm	~200 mm / ~110 mm
Angle of view (approx.)	60°	75°/67°
Spectral range	UV-IR	VIS/ VIS-NIR
f-number	F/4.5	F/14.8 / F/7.0

2.2.2 Chemiluminescence

Chemiluminescence (CL) in combustion refers to light emission from electronically excited molecules formed by a chemical reaction [81]. The emission of CL occurs when the excited electron returns to the electronic ground state, emitting photon energy at different wavelength, ranging from ultraviolet (UV) to infrared (IR). The generation of CL involves two steps: formation (E2.15) and the radiative transition (E2.16) of excited-state molecules. However not all excited-state molecules are involved in the process of generating CL due to collision (quenching) or reaction with other species (E2.17).

$$A + B \rightarrow R^* + \text{others} \tag{2.15}$$

For example, according to Gaydon [82], the reaction responsible for OH*, CH*, and C_2* formation are

$$CH + O_2 \rightarrow OH^* + CO$$

$$C_2 + OH \rightarrow CH^* + CO_2$$

$$CH_2 + C \rightarrow C_2^* + H_2$$

Meanwhile, the consumption of OH*, CH*, and C_2* are given by reactions[82, 83]:

$$R^* \rightarrow R + h\nu \tag{2.16}$$

$$OH^* \rightarrow OH + h\nu$$

$$CH^* \rightarrow CH + h\nu$$

In non-radiative collisional quenching, the excess energy of OH* is transferred to the colliding molecule.

$$R^* + M = R + M \tag{2.17}$$

$$OH^* + N_2 \rightarrow OH + N_2$$

where A, B, and R are different ground-state molecules, R* is an excited-state molecule, and M is a third-body species.

The most important excited-state species in hydrocarbon flames are OH*, CH*, and C_2* with the peak wavelengths of 308 nm, 431 nm, and 473 nm, respectively, as shown in Figure 12.

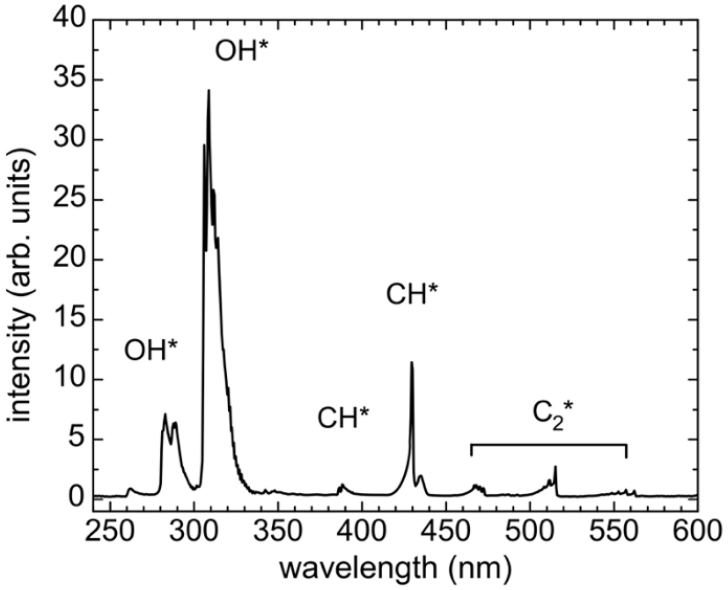

Figure 12: UV-VIS flame emission spectrum of a hydrocarbon flame. [84]

2.2.3 Flame growth imaging

Imaging-based combustion diagnostics is well-established in optical research engines. The investigation of early flame propagation is the key to evaluate the efficiency of combustion process in SI engines, partly because this stage of combustion is closely associated with cycle-to-cycle variability [47, 48]. The initial phase of this combustion is important due to the variation of the combustion cycle and therefore the expansion of pressure begins at this phase. Combustion can be detected by imaging of chemiluminescence (CL) from excited OH and CH radicals [47, 48, 85] or sodium added to the fuel [15], by Schlieren techniques [20], or by OH and formaldehyde LIF [8, 86-88]. Each of these techniques can deliver two-dimensional (2D) images, or time sequences thereof, but since their signal generation is based on different principles, they deliver information on different aspects of the complex three-dimensional (3D) time-dependent phenomena of premixed turbulent flame propagation. In particular, ‘active’ methods such LIF and Mie scatter that are based on thin laser-light sheets show a 2D section through the enflamed volume of gas (flame-front), while “passive” visualization and Schlieren techniques yield a line-of-sight (LOS) integrated 2D projection of the 3D volume. In general, the former class of techniques is more suitable for small-scale quantification of physio-chemical properties like flame speed, local convection, and flame wrinkling. An excellent recent example is the detailed examination of local flame propagation velocity in an engine in Ref.[88]. The latter class of measurements, in particular CL imaging, is much simpler in its implementation but correspondingly yields less detailed results, principally, because of the loss of

information that accompanies the LOS projection. Nevertheless, much useful information about early combustion and even flame-front propagation in optically accessible spark-ignited (SI) engines can and has been obtained with all of these techniques. Even some of the LOS-integrated investigations show a strong correlation between combustion imaging and pressure-derived heat release [47, 48, 54]. Hence, such imaging can be used as an indication of reaction progress.

Aleiferis [54] investigated flame variability in an optical, stratified-charge SI engine at stoichiometric (A/F = 15) and lean (A/F = 22) mixture conditions. The flame propagation images were captured using a ‘double exposure’ technique, in which two identical intensified CCD cameras were utilized to record two consecutive images with 5°CA interval on cyclic basis, as shown in Figure 13a. Projected flame-boundary analysis and heat release calculation showed good correlation between optical flame growth rate and timing of 5% fuel mass burned.

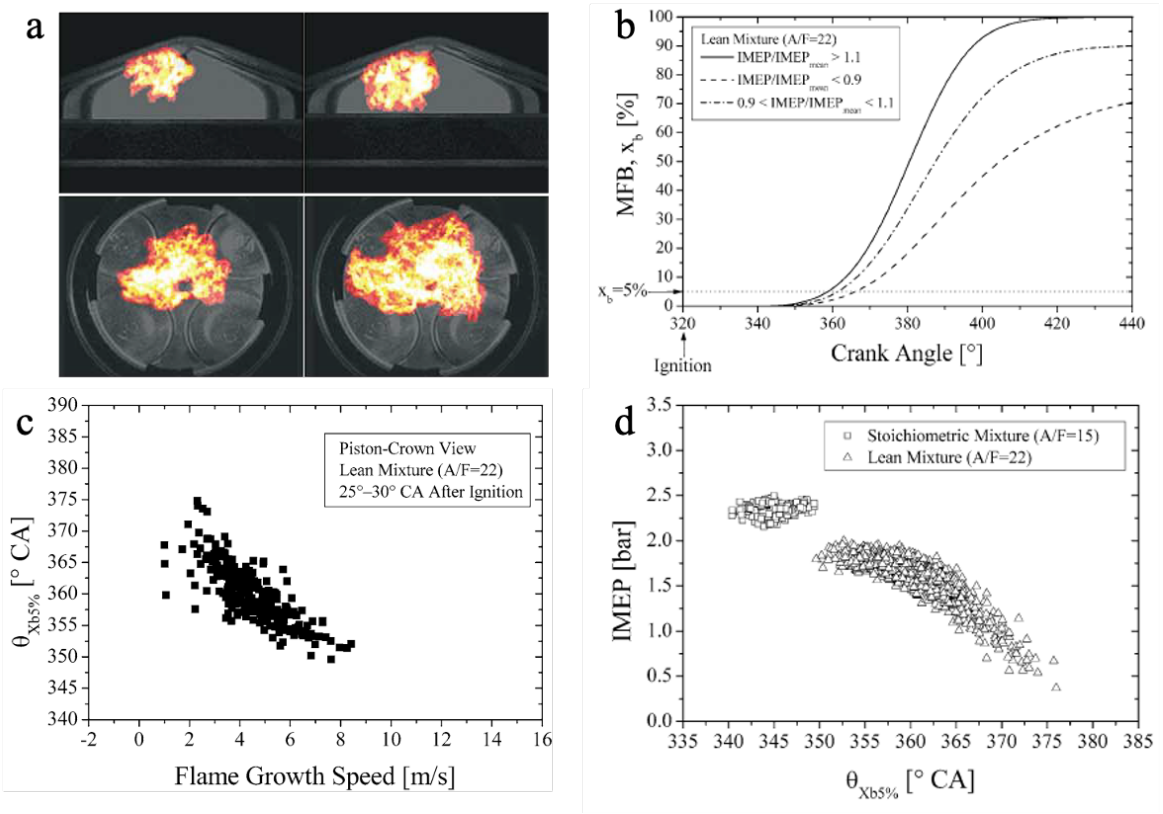

Figure 13: Early flame development in a lean-burn (A/F=22) stratified-charge SI engine. [54] (a) Typical flames as imaged through the pentroof window at 20 and 25°CA AIT (upper) and the piston crown at 35 and 40°CA AIT (bottom); (b) MFB traces and CA of 5% MFB; (c) Correlation between CA5 and flame speed; (d) Relationship between IMEP and CA5 for stoichiometric and lean mixture conditions.

Zeng et al. [15] visualized flame propagation in a single-cylinder optical research via the piston crown. The spatial and temporal flame images were recorded using a high-speed camera at a repetition rate of 12 kHz, equivalent to 0.5°CA per image at 1000 rpm engine speed. Metal alkali dissolved in heavy oil added to the gasoline greatly increased the visible flame luminosity, and consequently increase the signal-to-noise ratio. Flame probability contours for poor and good cycles were generated based on conditional analysis.

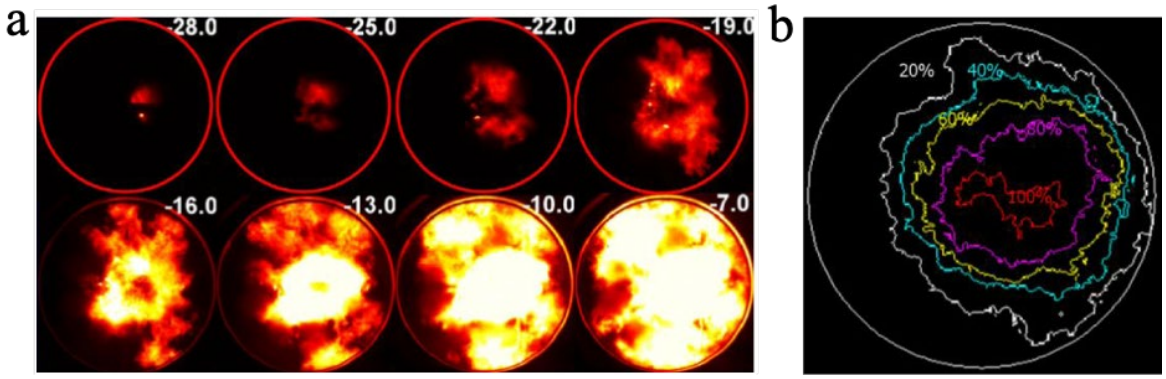

Figure 14: Sodium-added flame image sequence [15]. (a) Typical combustion for fast cycles; (b) Flame probability contours based on conditional analysis.

Another work on flame visualization was done by Dahms et al. [11, 89] using high speed Mie scattering and sodium-enhanced detection in an optical DISI engine. Silicone oil droplets with nominal 1 μm diameter were introduced into the air stream for both Mie scattering and PIV measurements. A copper-vapor laser at 12 kHz (2 mJ energy per pulse) was used to illuminate the droplets for high-speed Mie scattering flame front detection. The evolution of 2D flame front images in a single engine cycle from planar laser Mie scattering can be seen through the burning of silicone oil droplets by the flame. Line-of-sight sodium-enhanced combustion luminosity imaging at 12 kHz was combined with planar 2D Mie scattering to track flame propagation in the engine cycle.

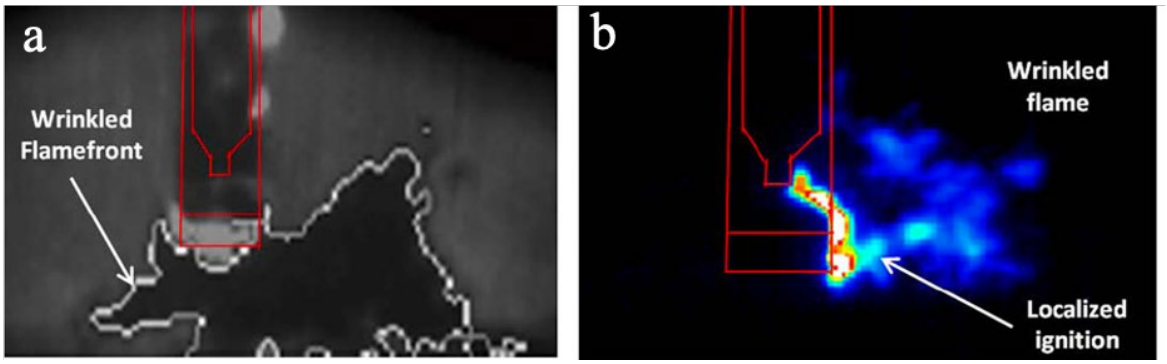

Figure 15: Early wrinkled flame propagation. (a) Mie scattering, (b) sodium-enhanced combustion luminosity. [90]

Recently published works [6, 7] also utilized high-speed 2D Mie scattering imaging to visualize the flame front propagation in optical research engines.

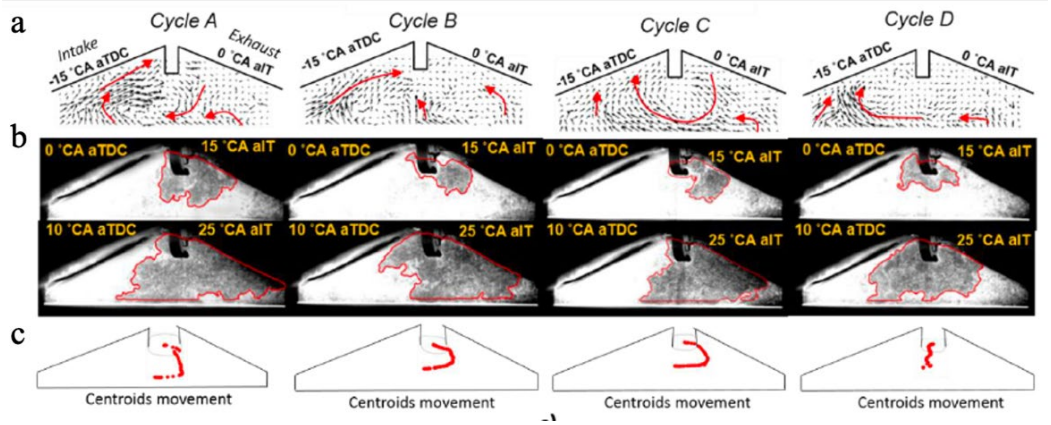

Figure 16: (a) Flow-field vectors of four selected cycles with different combustion performance at the same operating condition, (b) Mie scattering images for detecting the flame front development, (c) flame centroids. [7]

This work investigated the interaction between the in-cylinder flow and flame propagation. It was found that the global vortex location of the tumble motion strongly influences the flame propagation direction, and the flame shape, mainly due to the tumble-induced flow in the vicinity of the spark.

A comprehensive work on 'passive' flame propagation imaging via endoscopic access was carried out by Goschütz et al. [85]. A large-aperture UV endoscope coupled with intensified camera systems was used to capture sequences of OH* chemiluminescence at various engine operating conditions. Three imaging systems ("phase-locked" single-shot, "phase-locked" double-frame, and "high-speed" cinematography) were compared in terms of detecting early flame boundary based on a line-of-sight projection principle. Endoscopic "phase-locked" single-shot imaging technique produced the best image sharpness and resolution, almost match the image quality produced in an optical research engine. The same imaging technique was also applied by Gessenhardt et al. [76, 91] to detect cyclic variations in flame propagation. However, this technique allows only the determination of multi-cycle averages of the flame speed. On the other hand, double-frame imaging enables computing the instantaneous flame speed for a particular combustion cycle. This technique has been previously applied by Aleiferis [47, 54] in an optical research engine. Endoscopic high-speed OH* chemiluminescence imaging, however, produced less image contrast and resolution compared to images obtained from the phase-locked imaging technique. Despite the limited spatial resolution of the images, this technique allows tracking of flame growth in a single cycle, and thus the crank-angle resolved burnt area can be estimated. Gessenhardt et al.[92] applied the same method to visualize irregular combustion events in a near-production engine. In more recently published work, this technique has also been applied [93, 94] in optical research engines.

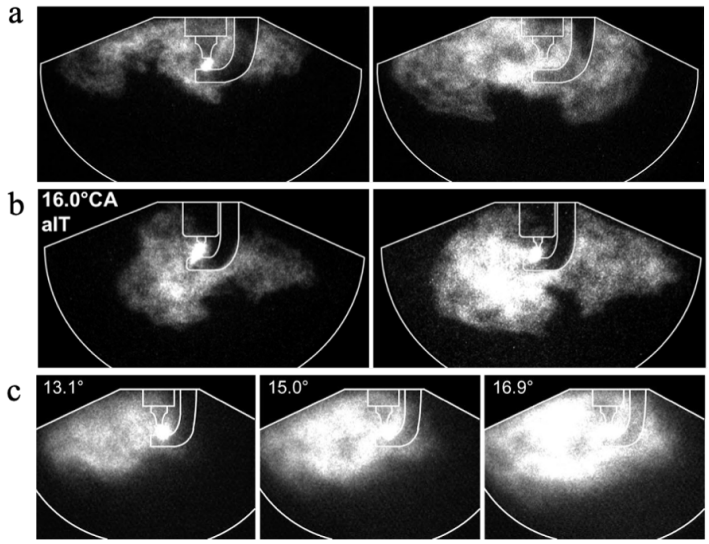

Figure 17: Endoscopic OH* chemiluminescence imaging [85]. (a) “Phase-locked” single shot at a fixed 14 °CA aIT for 2 cycles; (b) “Phase-locked” double frame with 4°CA delay; (c) high-speed imaging at about 7 kHz repetition rate.

Goschütz et al. [95] performed simultaneous single-shot imaging of anisole LIF and OH* chemiluminescence through the same endoscopic system in [85]. ‘Active’ planar imaging of anisole LIF enables visualizing turbulent flame front, meanwhile ‘passive’ OH* CL imaging provides the projected burnt area (PBA), a line-of-sight (LOS) integrated 2D projection of the 3D volume. The calculated PBA was plotted versus the cylinder pressure from both measurements and it was found that the PBA from OH* CL imaging correlated better with in-cylinder pressure. Therefore, it was concluded that the line-of-sight integration of CL imaging yields a better two-dimensional representation of the burnt volume.

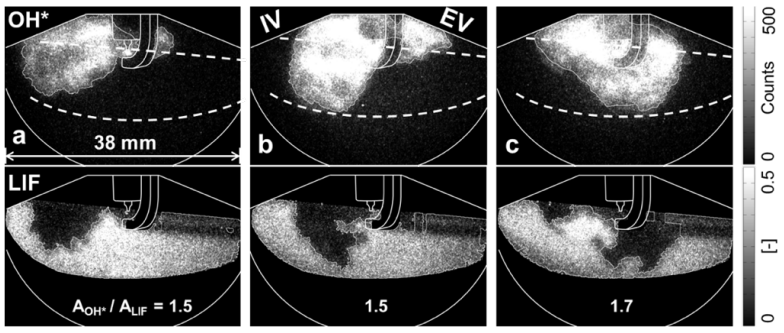

Figure 18: Single shot image pairs from flame-front visualization by simultaneous detection of OH* CL and anisole LIF at 14°CA aIT.

Recent work [96] visualized flame propagation in full optical PFI and SIDI engines. The line-of-sight integrated blue flame luminosity was captured using high speed CMOS camera (Phantom v7.3) with an 85 mm lens f/1.4 at repetition rate of 41 kHz. The calculated apparent flame speed was combined with pressure-derived heat release analysis and the early flame propagation and flow field were correlated based on conditional analysis.

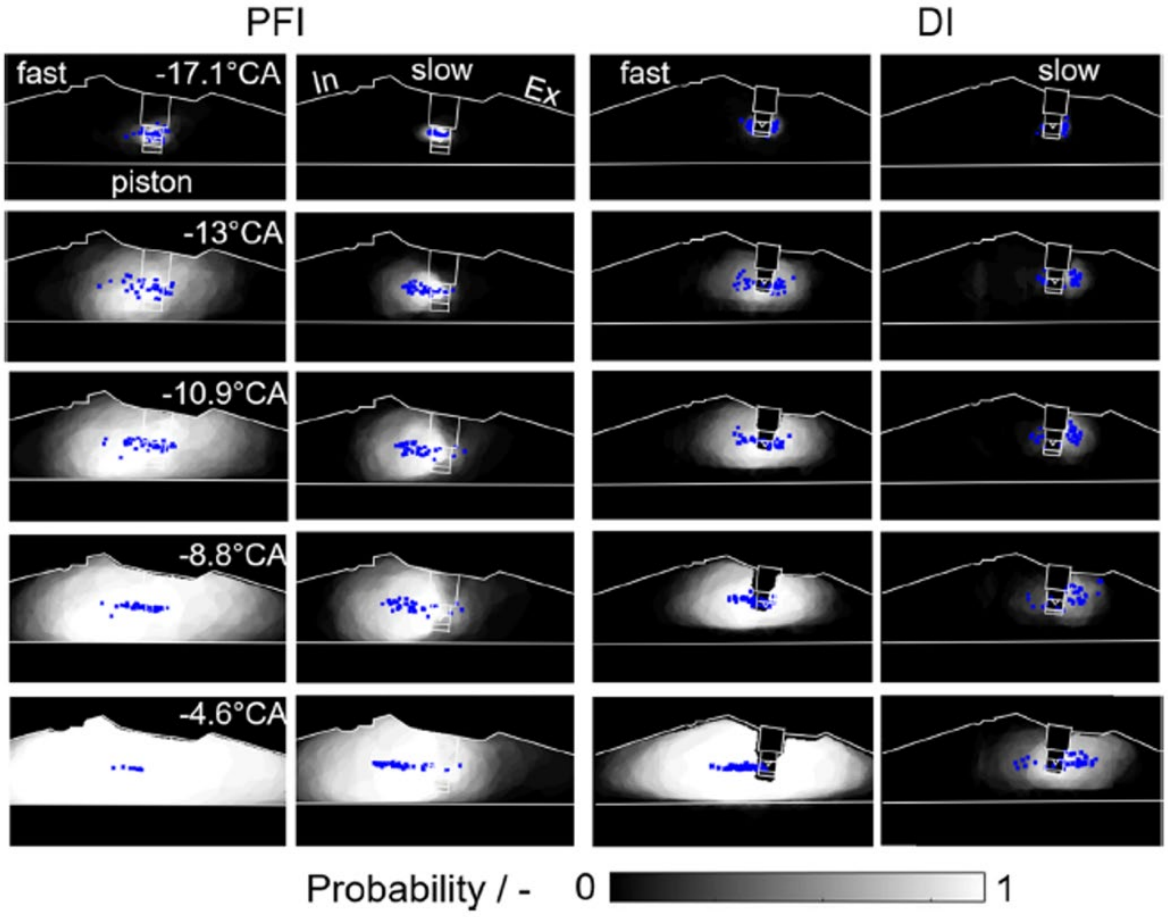

Figure 19: Conditional mean probability flame contours for the fast and slow cycles during early flame propagation. The blue markers indicate the centroid position of each cycle's burnt area. [96]

The recent works on flame imaging measurements in SI engines are summarized in Table 2.

Table 2: Summary of flame imaging measurements in SI engines.

No.	Authors (year)	Imaging technique	Process identified/ Measured quantity
1.	Aleiferis et al. (2004) [47]	Glass liner and piston crown optical engine stratified-charge OH* Chemiluminescence (CL) double frame ICCD	Cyclic variation; turbulent flame shape/location; good correlation between optical flame growth and CA5
2.	Drake et al. (2010) [90]	Optical DISI engine LOS-sodium-enhanced combustion luminosity High speed CMOS	Early flame propagation Projected burnt area (PBA) and apparent flame speed (AFS)
3.	Dahms et al. (2011) [11, 89]	Optical DISI engine 2D Mie scattering/LOS-CN* CL/ broadband CL High-speed CMOS	Wrinkled flame front Projected burnt area (PBA) and speed (AFS)
4.	Zeng et al. (2011) [15]	Optical DISI engine LOS-sodium-enhanced combustion luminosity High-speed CMOS	Cycle-to-cycle variation; Flame propagation driven by local convection; Irregular combustion events Conditional flame probability contours (CA10)
5.	Salazar et al. (2011) [20]	Optical DISI engine Schlieren Density gradients (LOS averaged) High-speed CMOS	Turbulent flame shape/location; correlation between optical flame growth and CA5; relation between flame centroid's location and speed with tumble strength
6.	Goschutz et al. (2014) [85]	Endoscopic production PFI engine OH* Chemiluminescence (CL) Phase-locked single shot/ double frame/ high-speed ICMOS Intensified CCD	Physical flame properties; correlation between optical and thermodynamics data
7.	Peterson et al. (2014) [97]	Optical DISI engine Simultaneously LIF, PIV, and Mie scattering imaging High-speed CMOS	Fuel injection, mixing process, ignition, and early flame development with crank angle time steps at the different spark timings and dilution levels. Conditional burnt gas area probability contours (CA5)
8.	Attar et al. (2015) [98]	Optical DISI engine tracer two-line LIF imaging (Negative LIF) Intensified CCD	Turbulent flame boundary and structure Gas temperature variation

9.	He et al. (2017) [12]	Optical PFI engine Mie scattering imaging High-speed CMOS	2D planar wrinkled flame front Experimental vs. simulation (flame and pressure)
10.	Peterson et al. (2019) [8]	Optical PFI engine Simultaneous dual-plane OH LIF and stereoscopic PIV OH LIF imaging High-speed CMOS	2D planar wrinkled flame front Conditional burnt gas area probability contours (CA5)
11.	Nishiyama et al. (2019) [6, 7]	Optical PFI engine PIV/Mie scattering/CL imaging High-speed CMOS	Wrinkled flame front Flow vectors Relation between flow fields and early flame propagation
12.	Shahbaz et al. (2021) [80]	Endoscopic production DISI engine Chemiluminescence (CL) imaging High-speed RGB color CMOS	Early flame propagation Establish the relation between spray, combustion, and soot formation.
13.	Laichter et al. (2022) [96]	Optical PFI / DISI engine Chemiluminescence (CL) imaging High-speed CMOS	Early flame propagation Cyclic variability in early flame propagation (LOS-CL) for PFI and DISI engines Establish relation between flow fields and early flame propagation Conditional flame probability contours (CA10)

2.2.4 Particle-image velocimetry (PIV)

PIV is a non-intrusive, laser optical technique used to compute two-dimensional instantaneous velocity vector in a cross-section of a flow [99-101]. Generally, a PIV system consists of several components:

1. **Seeding particles**: Small, lightweight particles introduced into the fluid to make the flow visible under laser illumination.
2. **Laser illumination**: Provides coherent light to illuminate the seeding particles in the fluid.
3. **Image detector(s)/synchronization unit/ data acquisition system**: Cameras equipped with appropriate optics to capture the scattered light and record the particle movement in the fluid. These cameras are synchronized with the laser, capturing and storing a series of images that show the movement of the particles over a short time interval.
4. **Image processing software**: Used to process the images and extract the velocity information from the displacement of the particles between consecutive frames. The images can be analysed using cross-correlation algorithms to determine the velocity field.
5. **Velocity field visualization**: The processed data can be visualized as velocity vector fields or contour plots.

In PIV measurements, the moving fluid (either gaseous or liquid) is seeded with highly scattering particles that are relatively small (<50 μm). In air flows, the seeding particles are often silicone oil droplets in the range 1 μm to 5 μm. A double-pulsed laser beam, typically emitted from a Nd: YAG laser at 532 nm is formed into a thin light sheet (<1 mm) to illuminate the seed particles in the flow. The time separation, Δt, between laser pulses is very short, on the order of milliseconds. The light scattered by the tracer particles is captured by one (double-frame) or more high-resolution digital cameras (CCD or CMOS sensor) focused on the illuminated plane. The coordinate space is defined from the targets image. An external timing system is typically used to synchronize the recording camera with the pulses of the laser operated at frequencies ranging from 10 Hz (slow PIV) to kHz (high-speed PIV). Each recorded image pair is divided into discrete regions (interrogation window) and the spatial displacement of particles between two successive images is determined through cross-correlation. This approach identifies individual or group of particles within each interrogation area for each image, and then determines the maximum cross-correlation function (maximum peaks) between the two images for each area.

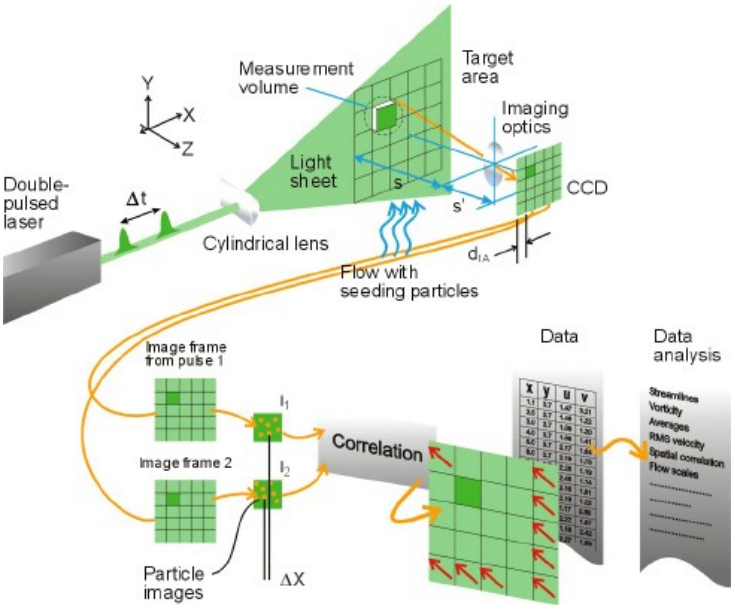

Figure 20: Principle of PIV measurement (Dantec Dynamics). [102]

The velocity vector is computed by combining the spatial displacement, Δx and the time difference, Δt of the images.

$$v = \frac{\Delta x}{\Delta t} \tag{2.18}$$

Applying this numerical technique to the entire field of view (FOV) represents a velocity vector map for the illuminated flow field. The computation of interrogation windows and cross-correlation algorithms between the image pairs can be accomplished either by commercially available software like Davis by Lavision GmbH, DynamicStudio by Dantec Dynamics, or MATLAB-based open-source programs such as PIVlab [103, 104], and OpenPIV [105].

PIV imaging is commonly employed in various fields of research, including engine studies, yielding valuable insight into the motion of fuel/air mixtures within the cylinder during different phases of the engine cycle. The processed PIV images are visualized as velocity vector fields or contour plots, giving researchers insight into the fluid flow patterns and velocities within the combustion chamber. This information helps understand the intake and exhaust flow characteristics, turbulence, swirl, and tumble motions, among other factors affecting combustion efficiency and emissions. Some of the more recent studies that utilized PIV in engines are summarized in Table 3.

Table 3: Summary of the recent PIV and Mie scatter measurements in SI engines.

No.	Authors (year)	Engine type/PIV technique	Observed/measured quantity
1.	Dahms et al. (2011) [89]	Optical DISI engine High-speed 2D Mie scattering	Wrinkled flame front propagation
2.	Peterson et al. (2014) [97]	Optical DISI engine High-speed simultaneous PIV and Mie scattering	Quantify flow velocity within the tumble plane Identify the enflamed region to resolve flame propagation Identify the cause of slower flame development: lean mixture; external dilution; convection velocity in the spark vicinity Conditional burnt gas area probability contours (CA5)
3.	He et al. (2017) [12]	Optical PFI engine High-speed 2D Mie scattering	2D wrinkled flame front propagation
4.	Peterson et al. (2019) [8]	Optical PFI engine High-speed stereoscopic PIV	Time-resolved flow velocity vectors 2D wrinkled flame front Conditional burnt gas area probability contours (CA5)
5.	Nishiyama et al. (2019) [6, 7]	Optical PFI engine PIV/2D Mie scattering/CL imaging High-speed CMOS camera	Wrinkled flame front propagation Time-resolved velocity vectors flow-field Relation between tumble flow and early flame propagation, no correlation between flame shape and propagation path with flame speed
6.	Kim et al. (2021) [51, 67]	Optical DISI/ production engine Endoscope High-speed PIV	Positive correlation between the TDC flow direction and spark stretch, and early flame propagation
7.	Laichter et al. (2022) [96]	Optical PFI / DISI engine High-speed PIV	Cyclic variability in early flame propagation (LOS-CL) for PFI and DISI engines Conditional flame probability contours (CA10) Correlation maps of the velocity magnitude with the equivalent flame radius at a selected CA. Established relationship between flow structure with early flame propagation.

2.3 Image segmentation of flame propagation in SI engines

Image segmentation is a process of dividing a digital image into distinct and meaningful regions to extract useful information for further statistical analysis [106]. It plays a crucial role in various applications, also in engine research [107] in order to characterize combustion in the engine cylinder. Generally, the main steps involved in image segmentation include pre-processing, thresholding, edge detection, and post-processing.

2.3.1 Image pre-processing

The pre-processing step enhances the quality of input images before applying segmentation algorithms. This step involves various processes such as background correction, image denoising and smoothing by filtering (in spatial and frequency domains), and contrast enhancement by histogram equalization. The choice of pre-processing steps depends on the specific characteristics of the images, and the segmentation algorithm being used. Effective pre-processing can significantly impact the accuracy and efficiency of the segmentation process.

Image spatial filtering modifies the visual characteristics of an image by altering the pixel values based on their surrounding pixels' values. It involves applying a filter or kernel to each pixel in the image by convolution, which computes a weighted average of the neighbouring pixels' values. This process is often used for tasks like noise reduction, edge enhancement, and blurring. The size and values of the filter kernel determine the specific effect achieved during spatial filtering.

Frequency filtering is commonly used in tasks like noise reduction, image sharpening, and feature extraction. It can be achieved through techniques such as Fourier transformation and convolution in the frequency domain. Image frequency filtering involves manipulating the different frequency components present in an image. Low-frequency components represent gradual changes like smooth areas, while high-frequency components capture rapid changes like edges and fine details.

2.3.2 Thresholding

Thresholding is a technique used in image processing to separate objects or features from their background in a binary (black and white) image. It involves converting a grayscale or color image into a binary image by assigning pixels above or below a certain threshold value to either one of two classes: foreground (object) or background. Thresholding is a fundamental step in various image analysis tasks, such as object detection, image segmentation, and feature extraction. There are

different thresholding methods such as global, adaptive, and Otsu's thresholding. Global thresholding is a technique in image processing where a single threshold value is applied to the entire image assuming a consistent intensity distribution across the entire image. This technique is particularly effective when the image has a bimodal histogram (Figure 21), where there is a clear and consistent separation between the object of interest and the background in terms of pixel intensities [108].

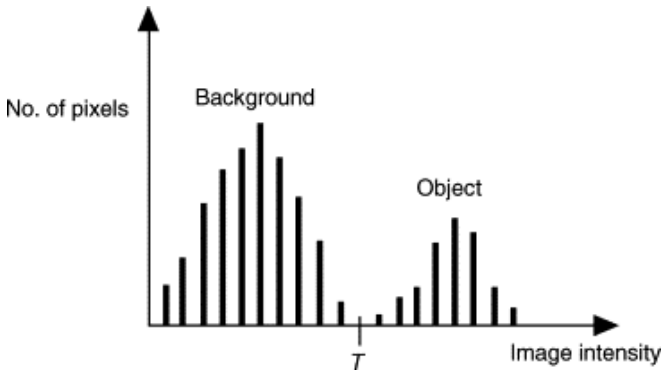

Figure 21: Bi modal histogram.

Adaptive thresholding takes into account local variations in image intensity. The image is divided into smaller non-overlapping regions or blocks. For each region, a threshold value is computed based on the local characteristics of that region. Common methods include calculating the mean or median intensity of the pixels within the region. This makes adaptive thresholding particularly useful for images with uneven lighting conditions or varying contrast [109]. Otsu's thresholding method [110] is an automatic thresholding technique used to determine an optimal threshold value for converting a grayscale image into a binary image. This method aims to find a threshold that maximizes the between-class variance, making it particularly useful for images with bimodal intensity distributions. The main advantage of this method is it helps to automate the process of finding an optimal threshold for different images, especially when manual threshold selection is challenging. Furthermore, this algorithm is readily available in the MATLAB image processing toolbox.

Otsu's thresholding method steps:

1. **Histogram calculation**: Compute the histogram of pixel intensities in the grayscale image. The histogram shows the frequency of occurrence of each intensity level.
2. **Compute probability distribution**: Normalize the histogram to obtain a probability distribution.
3. **Calculate cumulative distribution**: Calculate the cumulative distribution by summing up the probabilities from the lowest intensity to the highest.

4. **Compute mean and variance**: For each intensity level, calculate the cumulative probability, mean intensity, and variance for both foreground (object) and background classes.
5. **Iterate over thresholds**: Iterate through all possible threshold values and calculate the between-class variance. The between-class variance measures the separation between the two classes (foreground and background).
6. **Find optimal threshold**: The threshold that maximizes the between-class variance is chosen as the optimal threshold value. This threshold effectively separates the object and background intensities while minimizing the variance within each class.
7. **Thresholding operation**: Apply the optimal threshold value to the image, classifying pixels with intensities above the threshold as foreground and those below the threshold as background.

2.3.3 Edge detection

Edge-based segmentation involves detecting edges or boundaries in an image using methods like the Canny edge detector [111], Sobel [112], Prewitt [113], and Robert operators [114]. Edges often represent object boundaries, making them useful for segmentation.

Table 4: Summary of edge detection methods.

Edge detector	Detection method	Advantages	Limitations
Canny	Local maxima of image gradient and hysteresis thresholding	• Available function in MATLAB - *edge (I, method)* • Accurate edge localization: Identifies edges with sub-pixel accuracy, i.e., it can pinpoint exact locations of edges even between pixels	• Sensitive to noise (computation of image gradient via convolution process) • Suffering from hysteresis thresholding, need to adjust threshold values for each image • Discontinuous edges: struggle to accurately detect edges that are not continuous or have significant gaps, such as

			dashed lines or edges with interruptions. Thus, requires advanced binary morphological processes
Otsu	Histogram-shape and statistic-based method	• Available function in MATLAB *graythresh (I)* • Fully automated • Free input parameter	• Only effective in bi-modal histogram shape • Uniform background illumination • Histogram shape varies for different image - different dynamic range in image brightness
Gradient-based method (Sobel, Prewitt, and Robert operators)	First and second order derivative	• Provide good prediction of where the location of the edges • Available function in MATLAB - *edge (I, method)*	• Sensitive to noise • Malfunctioning at corners, curves and where the intensity function varies • Discontinuous edges • Lack of robustness: Not robust enough to handle images with varying lighting conditions, non-uniform illumination, or other non-ideal imaging conditions

2.3.4 Image post-processing

After segmentation, further processing like gap filling, and refining boundaries might be necessary to remove artifacts caused by the segmentation process, and thus improve the accuracy of the segmented regions. Some post-processing steps used in image segmentation:

1. **Morphological operations**: Techniques like dilation, erosion, opening, and closing are used to modify the shape and size of segmented regions, filling gaps or eliminating small disconnected regions. Region merging and splitting involves merging adjacent regions that should be part of the same object or splitting regions that were erroneously merged during segmentation. Connected component analysis is used to identify and label connected regions within segments to distinguish between individual objects or structures. Size-based filtering removes or retains segments based on their size to eliminate very small or very large segments that might be artifacts or outliers.
2. **Compute object properties**: Calculates the segmented regions properties (such as area, centroid, orientation).

Most of these operations or functions are readily available in MATLAB image processing toolbox.

2.4 Application of image segmentation in engine research

Image analysis enables the extraction of quantitative information from chemiluminescence images, including flame probability contour, projected burnt area, flame centroid location, and flame propagation speed [96]. These optical parameters can be further used to characterize flame propagation [47, 54, 85, 115], ignition [89], and flame front dynamics [47]. The detailed information contributes to a deeper understanding of combustion physics, turbulence, and the interaction between different components of the combustion process. This information is essential for improving combustion efficiency, reducing cycle-to-cycle variations, addressing flame instability, detecting misfires or abnormal combustion events, and enhancing the overall combustion process [15, 48].

Recent studies have explored the application of machine learning (ML) algorithms to analyse flame images for predicting combustion cycles [116, 117]. These algorithms can learn patterns of normal and abnormal combustion, aiding in real-time flame detection and diagnostics.

The main challenge is that luminosity from the early flame in premixed combustion in spark-ignition engines is quite weak and much of it occurs in the UV, where high-speed CMOS cameras are not

sensitive. Additionally, the bright spark event overlap in time and space. The other challenge is the wide range of image brightness during the relevant part of the cycle, which is also subject to cycle-to-cycle variability. This makes morphological processing of the flame images challenging.

Chapter 3 Engine test bench with endoscopic access

This chapter describes the BMW N46B20 engine test bench at the Institute for Energy and Materials Processes (EMPI) - Reactive Fluids, University of Duisburg-Essen. This includes the main engine modifications to create additional ports for optical endoscopic accesses. The instrumentations for data acquisition such in-cylinder pressure and temperature are also presented. The detailed explanation of the endoscopes used for image detection and laser-sheet forming optics is also presented in this chapter.

3.1 Engine test facility

The automotive engine investigated here, was the BMW 4-cylinder model N46B20. The engine test bench with endoscopic access is illustrated in Figure 22. The engine features a mechanically variable intake-valve train ("Valvetronic"), controlling the load by reducing the valve lift and opening duration in part-load operation. The engine speed was controlled by a dynamometer, while the load was set by an analogue input to the OEM engine control unit (ECU), which then determined all other parameters like fuel injection, ignition timing (IT), as well as valve lift and valve timings. It was not possible to actively change the ECU's parameterization, but all relevant values could be read out. In the current work, the engine was operated at 2000 min^{-1} and 75 Nm, and the maximum torque at that speed is 176 Nm. To achieve this load, 4.4 bar IMEP, at 1000 mbar intake pressure, the ECU set a maximum intake valve lift of 2.2 mm. The engine parameters and operating conditions are summarized in Table 5. Note that the low valve lift may cause an in-cylinder flow substantially different from that with conventional valve operation, which in turn may influence flame propagation.

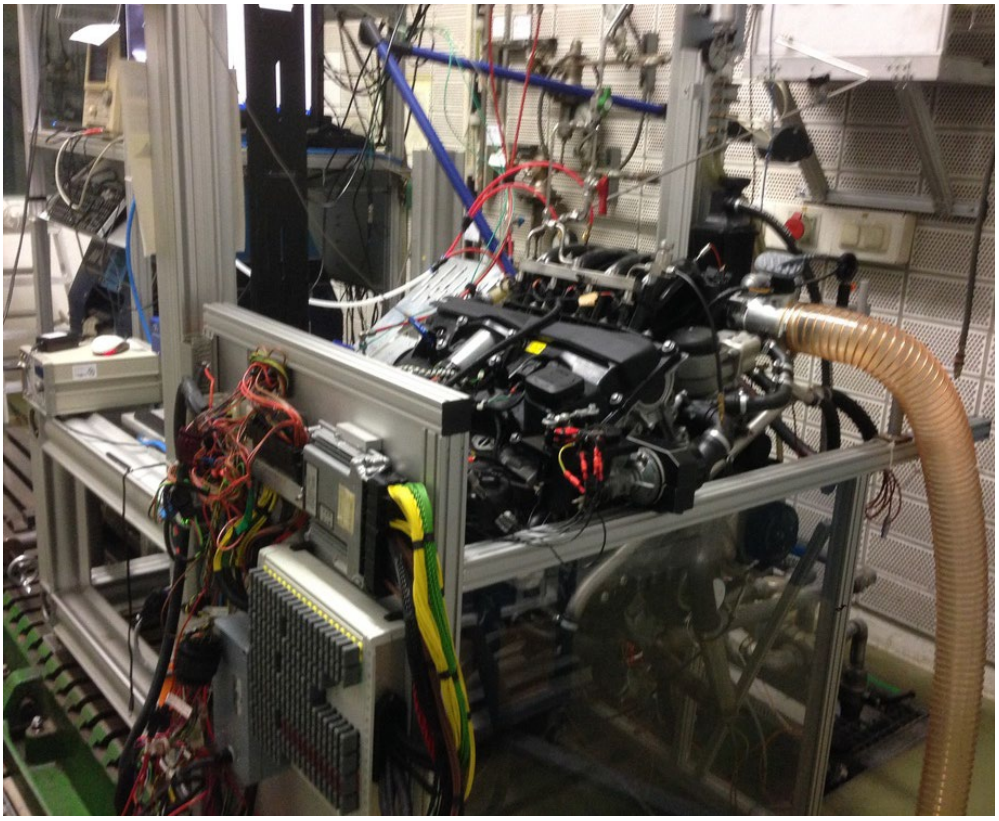

Figure 22: BMW N46B20 engine test bench.

Table 5: Engine parameters and operating conditions.

Engine	**BMW N46B20**
Cylinders	4, inline
Compression ratio	10
Displacement per cylinder [cm³]	499
Bore / stroke [mm]	84 / 90
Speed [min^{-1}] / load [Nm]	2000 / 75
Fuel system	PFI, Gasoline
Relative fuel/air-ratio	1.0
Ignition timing [°CA]	-34.5
IMEP [bar]	4.4
Intake pressure [mbar]	1000

The engine is equipped with pressure transducers in the working cylinder and a crankshaft encoder. The engine test bench is controlled and monitored by a test-bench computer with the established

testing software BMW INPA and COMBI. This software brings all measurement categories and control factors like temperatures and pressures together. Furthermore, the engine temperature is controlled via internal and external water-cooling systems. Coolants and lubricants can be heated up to 120 °C.

3.2 Endoscopic imaging system

The main modifications of the engine were two additional ports in the fourth cylinder (by the gear box), creating optical access via two endoscopes with 10 mm diameter each, one for laser input and another for observation. The engine with endoscopic access is shown in Figure 23. To enable optical diagnostics over the full operating range of the engine, the front section of the endoscope was protected from the combustion chamber pressure and temperature by a 3 mm-thick sapphire window, mounted in a titanium bushing with an outer diameter of 12 mm.

The endoscopic system utilized a two-stage concept, as illustrated in Figure 11. A front endoscope with wide-angle characteristics was mounted directly in the engine, creating an intermediate image on a field lens. The maximum angle of view was about 60°, yielding a field of view (FOV) with a diameter of about 30 to 45 mm (depending on the engine bore) in the center of the combustion chamber. All lenses in the endoscope are made from UV-grade fused silica. The collection efficiency of this endoscope is about equivalent to that of a 105 mm F/4.5 UV-Nikkor lens [33], which is quite poor compared to commercial lenses for typical low-light imaging applications in the visible, but actually very good for an endoscope system. A relay optic, isolated from the vibrations of the engine, projected this intermediate image onto the camera. For imaging in the UV, the relay optic was a hybrid refractive-diffractive optical (R-DO) element, correcting the system's inherent chromatic aberrations [74]. For imaging in the visible, a commercial camera lens was used instead to re-project the intermediate image. The system was designed in a previous project and is now commercially available from LaVision, Germany. With this endoscope system, imaging was carried out in various experiments.

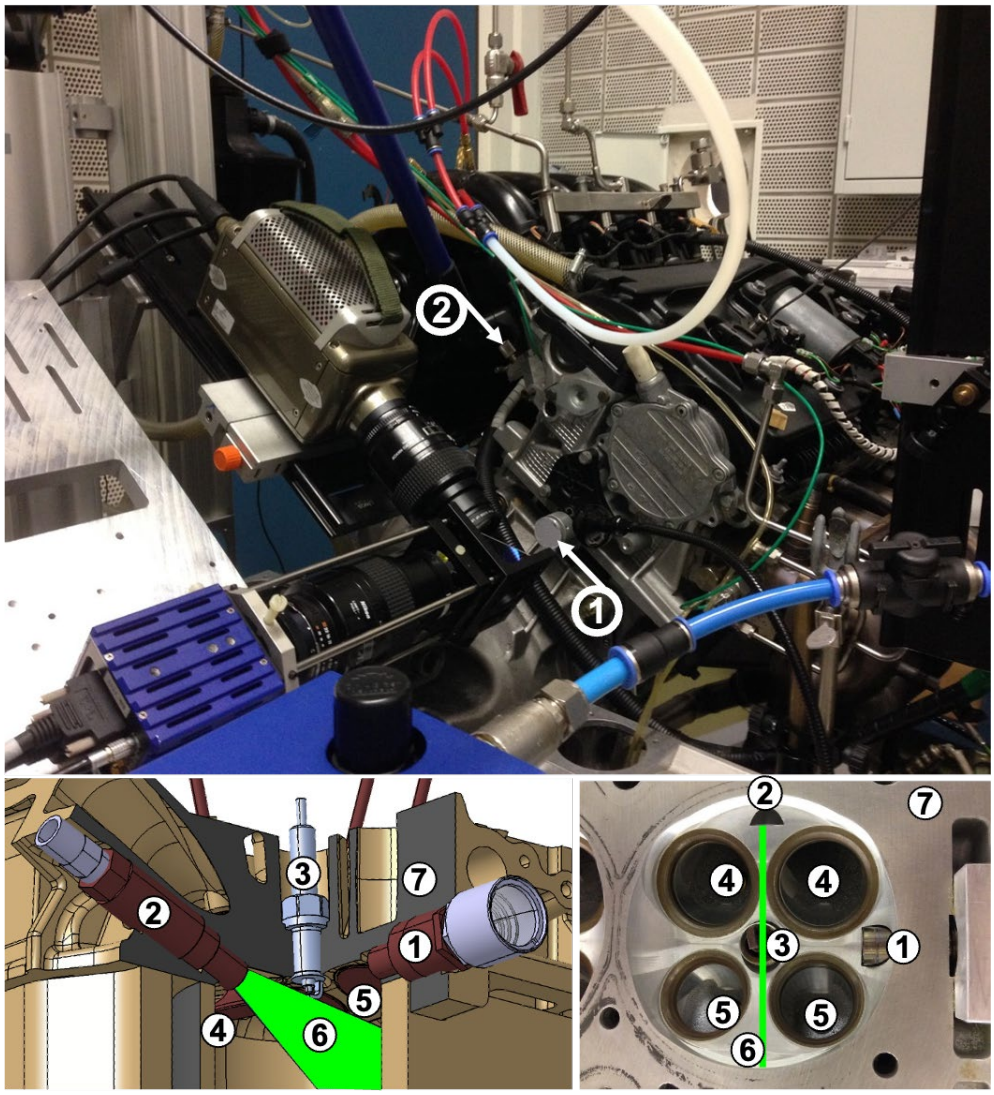

Figure 23: Engine with endoscopic access (detection and laser). [118]

Table 6: Engine components and optics.

Label	Apparatus	Label	Apparatus
1	Front endoscope (detection)	**4**	Intake valve
2	Laser endoscope (light-sheet)	**5**	Exhaust valve
3	Spark plug	**6**	Laser sheet
		7	Cylinder head

3.2.1 Hybrid endoscope

The front endoscope consists of three elements of UV-grade fused silica spherical lens and is transparent in the UV-VIS range. The front endoscope with wide-angle characteristics is mounted directly in the engine, creating an intermediate image on a field lens. The maximum angle of view is about 60°, yielding a field of view (FOV) with a diameter of about 40 mm (depends on magnification) in the centre of the combustion chamber. It was protected from the high combustion chamber pressure and temperature by a 3 mm-thick sapphire window, which is mounted in a titanium bushing with an outer diameter of 12 mm. Details of the optical design can be found in [74]. The endoscope specifications are summarized in Table 7.

Figure 24: Front hybrid endoscope. [74]

Table 7: Specifications of the hybrid endoscope.

Features	Hybrid endoscope
Diameter	10 mm
Length	~77 mm
Angle of view (approx.)	60°
Spectral range	UV-IR
f-number	F/4.5

3.2.2 Laser endoscope

The laser endoscope, as shown in Figure 26, is a cylinder with an outer diameter of 9 mm. It features an inner square cross-section and consists of 3 elements of cylindrical lenses. This lens arrangement yields a thin light sheet with an angle of 44° before entering the combustion chamber. At a working distance of about 46 mm, the light sheet has a thickness of approximately 1 mm at the centre of the combustion chamber and it illuminates almost the entire upper side of the test section.

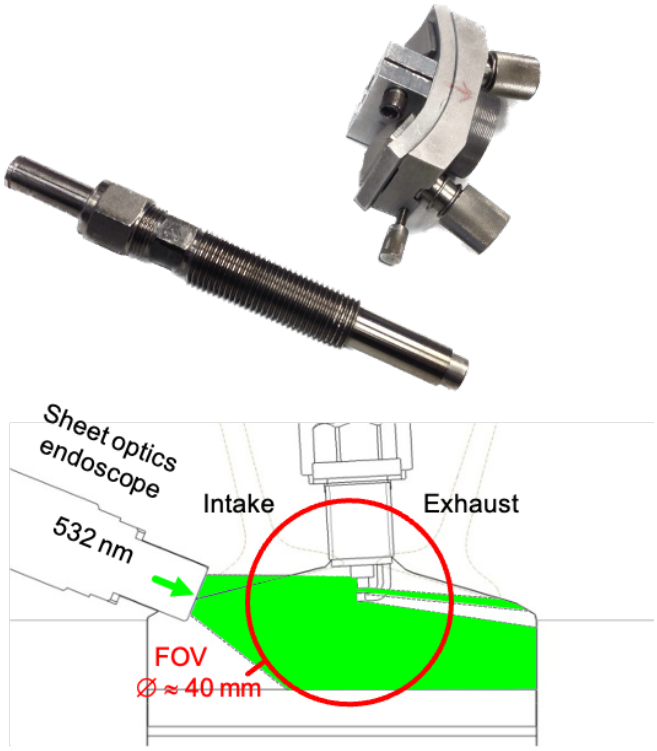

Figure 25: Laser endoscope. [118]

Chapter 4 Automated flame detection: 'Predictor-corrector' scheme

This chapter presents a new mathematical algorithm for automated flame detection in high-speed image sequences. The developed algorithm is simple, unsupervised, and computationally inexpensive to segment a sequence of flame images into three levels which correspond to spark, flame, and background. The main idea is to exploit the images' correlation in time to predict a suitable binarization threshold from the previous image. The algorithm is expected to compute the projected burnt area and flame centroid position which will be used to obtain the flame characteristics in a fast, robust, and reliable way. This information is used to determine early spark and ignition behaviour, cycle-to-cycle combustion variation, and as an input parameter for pressure-derived thermodynamics analysis. Then, the binarization scheme is compared with three literature-documented methods in terms of detecting flame boundary. The robustness of the algorithm was tested on image sequences acquired at different lens apertures.

The findings of this work have been published in [14, 95, 119-122]. The algorithm has been adapted as an optional module in the commercial software *Davis*, LaVision. The **Flame Front Propagation** module is an advanced image analysis tool used to automatically detect and track flame propagation in IC engines. This module can be coupled with **EngineMaster *inspex*** system for in-cylinder spray and combustion imaging via endoscopic access. The 'predictor-corrector scheme' algorithm has been applied and cited by other researchers in their work [96, 123, 124].

4.1 Structure of image data sequence

Each dataset consists of 143 cycles, which contain 55 images each. The structure of the recorded high speed image sequences is illustrated in Figure 27. All images of each cycle were stacked on a three-dimensional axis in MATLAB before further post-processing.

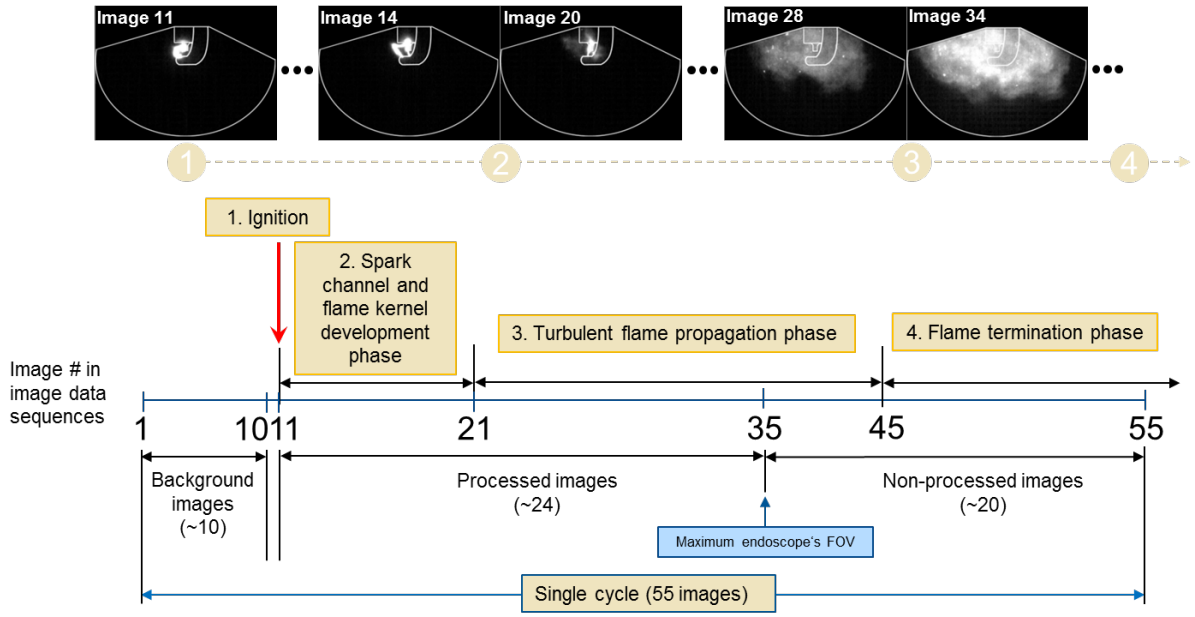

Figure 26: Typical structure of kHz image data sequence.

4.2 General segmentation procedure

In order to derive quantitative spatial information on the flame growth rate, the images are segmented by intensity-based thresholding. The main challenge is the wide range of image brightness during the relevant part of the cycle, which is also subject to cycle-to-cycle variability. To improve the robustness of the binarization with free user input but still good accuracy, a new segmentation algorithm is introduced here. The automatic dynamic thresholding algorithm, termed as Predictor-Corrector scheme (PC) is described as below:

1. **Background subtraction**: The 10 dark images of each cycle taken immediately before the spark event are averaged and this average is subtracted from each subsequent image.
2. **Fourier filtering**: Images from the Phantom v7.3 camera are filtered in the frequency domain suppressing patterned read-out noise. This is described in more detail below in section 4.3.2.

3. **Spatial filtering**: The background-corrected images are filtered using a 3x3 pixel median filter to reduce shot noise and the remaining pattern noise.
4. **Thresholding**: The filtered images are binarized by intensity-based thresholding by the newly developed algorithm called "predictor-corrector" thresholding scheme (PC). This process is described in more detail in section 4.4.
5. **Morphological operation**: The binarized images undergo some morphological processes to remove small spurious regions of foreground.

4.3 Filtering process

The filtering process was applied to the background-corrected images before proceeding with additional post-processing steps. This step aimed to enhance the image quality and extract relevant information. Considering the presence of various types of noise in the raw images, two types of filtering were utilized for enhancing the image quality. Filtering was conducted on the background-corrected images in both spatial and frequency domains.

4.3.1 Spatial filtering

The background-corrected images were filtered using a 3 x 3 pixels median filter to reduce shot noise and preserve useful detail in the image. The available function in MATLAB called *medfilt2* was used to implement this process.

4.3.2 Frequency filtering

The recorded images from the Phantom CMOS camera, in particular at smaller apertures (lower signal) contain periodic pattern noise and its effect on the image can be seen in the single-shot dark image as shown in Figure 29a. The pattern has the same geometrical structure in all images but its intensity varies in both spatial and time domain. The characteristics of this pattern noise influence the binarization process to identify the 'correct' flame boundary. Therefore, FFT filtering was used to remove the periodic pattern from the images, and the procedure of its implementation is shown in Figure 28.

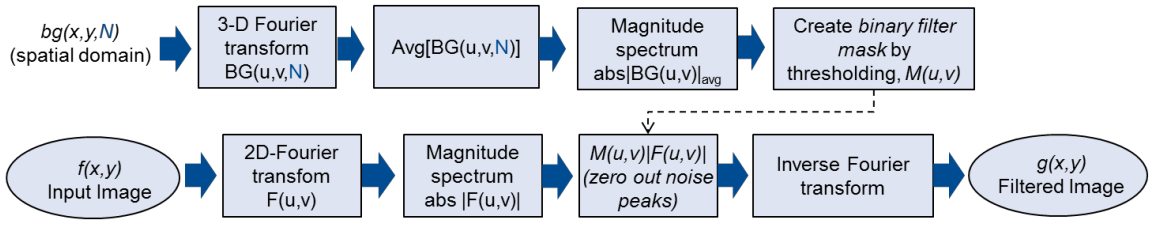

Figure 27: Process flow of frequency domain filtering.

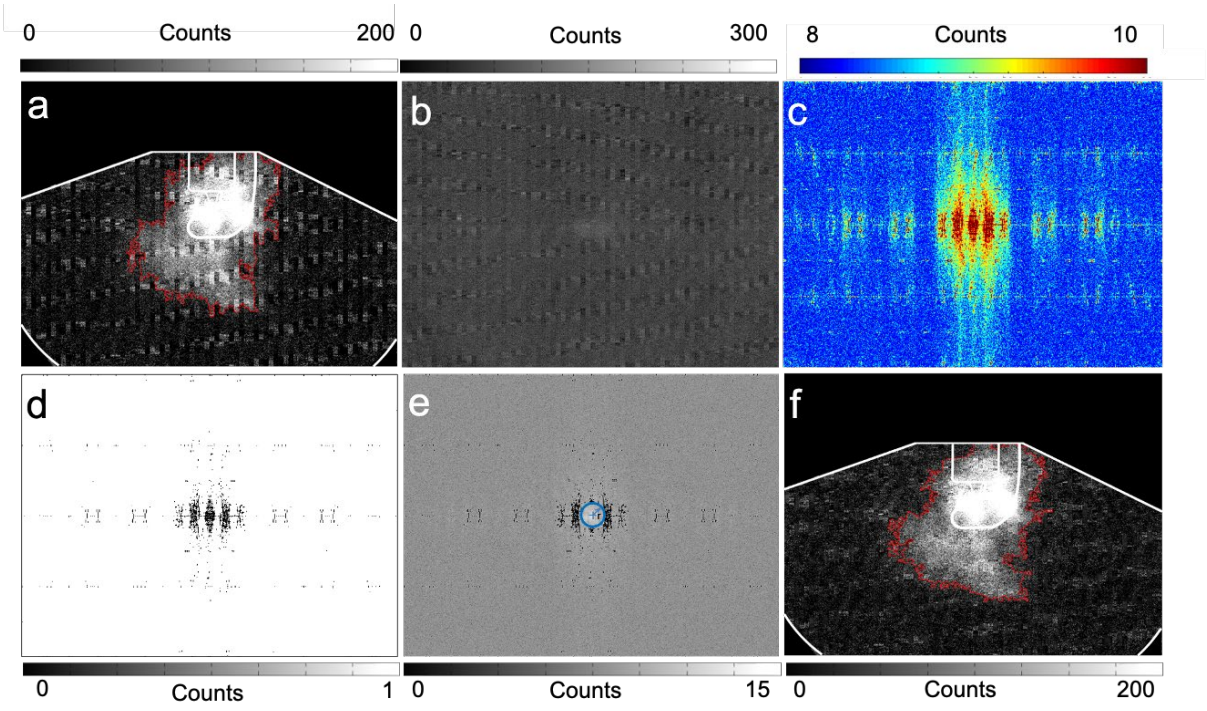

Figure 28: Pattern-noise suppression by Fourier filtering.

a. Background corrected flame image, $f(x,y)$. The red line indicates the detected flame boundary without Fourier filtering
b. Single-shot dark image in spatial domain, $bg(x,y)$
c. Average of *frequency amplitude* of dark images in log-scales, $|BG\ (u,\ v)|_{avg}$
d. Filter mask derived from image c (binary image), $M\ (u,\ v)$
e. *Frequency amplitude* (log-scale) of flame image after applying filter mask with the DC – component excluded, $|F\ (u,\ v)|\ M\ (u,\ v)$
f. FFT filtered flame image, $g(x,y)$. The red line indicates the detected flame boundary with FFT filtering

Figure 29a shows the background-corrected flame image with the red line indicates the detected flame boundary without FFT implementation. It can be clearly seen that this periodic pattern noise affects the binarization process, especially on flame edges, where some of the pattern structures are also detected as part of the flame boundary due to the variation of its intensity in spatial domain.

First, the time series of dark images of each cycle immediately before the spark event were individually transformed into its Fourier domain, *frequency dark image*, $BG(u,v)$ which represents a particular frequency contained in the *spatial domain dark image,* $bg(x,y)$. A sample of individual dark image in the spatial domain is shown in Figure 29b. Then, each *frequency dark image* was shifted in such a way that the DC component of the image, which corresponds to the average intensity is displayed in the center of the image. The corresponding frequency of a *frequency dark image* point is higher when it is further away from the center. The *frequency dark image* consists of two components, *frequency amplitude* (real part) and *phase* (imaginary part) and they were stored as separate images.

Next, the *amplitude* of each *frequency dark image,* $|BG\ (u,\ v)|$ were computed and averaged. Figure 29c shows the average of the *frequency amplitude* of dark images, $|BG\ (u,\ v)|_{avg}$ in log-scale for better visualization. The information gained from the average *frequency amplitude dark image* was used to examine and process certain frequencies of the image, which influence the geometric structure in the spatial domain. This image also gives information about the location of the frequencies that correspond to the periodic pattern noise. In order to identify all 'spikes' that correspond to the frequencies of the periodic pattern noise, a filter mask was created by thresholding the average of the *frequency amplitude dark image* by 60% of its maximum intensity value (DC component). Figure 29d shows the filter mask, $M(u,\ v)$ after thresholding. To cut off all the frequencies that correspond to the periodic pattern noise in the flame image, the filter mask was applied on each *frequency image,* $F(u,\ v)$ of the subsequent flame images. Figure 29e shows the log-scale *frequency amplitude* of the single-shot flame image after applying the filter mask which excluded the DC-component area (blue circle).

Finally, the filtered *frequency flame imag*e, $|F\ (u,\ v)|\ \text{x}\ M\ (u,\ v)$ was inverted to transform back the image into its *spatial domain image,* $g(x,y)$. Figure 29f shows the output of the flame image after the FFT implementation. The red line indicates the detected flame boundary with FFT filtering. However, the geometrical structure was not completely removed from the image flame. This is because the corresponding frequencies of the pattern noise still partially remain in the *frequency flame image*, in particular in the low frequency region near the DC component.

4.4 Predictor-corrector thresholding scheme (PC)

4.4.1 Working principle

After the pre-processing step, the filtered image was binarized by the predictor-corrector thresholding scheme. The working principle of the predictor-corrector thresholding scheme is shown in Figure 30.

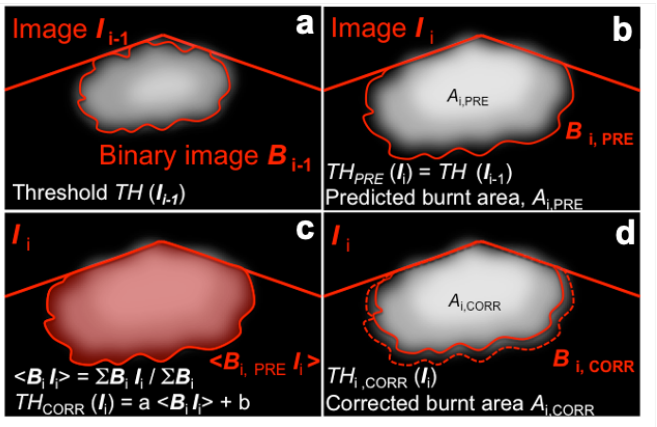

Figure 29: Principle of the predictor-corrector thresholding scheme.

The initial threshold TH_1 for the first flame image $\boldsymbol{I}_1$ is determined by Otsu's method [110], a parameter-free histogram-based method available in MATLAB's image processing toolbox. $\boldsymbol{I}_1$ is binarized by thresholding at TH_1 (Figure 30a). For each subsequent image $\boldsymbol{I}_i$, starting with the second image $\boldsymbol{I}_2$, the following steps are performed:

a. **Predictor**: Binarize $\boldsymbol{I}_i$ at the current threshold value $TH_{i-1} = TH_{i,\,PRE}$ (originating from the previous image, Figure 30a) to yield the binary image $\boldsymbol{B}_i$, Figure 30b

b. Based on the average intensity in this pre-estimated burnt area, Figure 30c, correct the threshold:

   i) Multiply image $\boldsymbol{I}_i$ by $\boldsymbol{B}_i$

   ii) Area-integrate this product image to yield $\Sigma \boldsymbol{B}_i \boldsymbol{I}_i$

   iii) Area-integrate $\boldsymbol{B}_i$ to yield $\Sigma \boldsymbol{B}_i$

   iv) Calculate the average intensity

   $$<\boldsymbol{B}_i \boldsymbol{I}_i> = \Sigma \boldsymbol{B}_i \boldsymbol{I}_i / \Sigma \boldsymbol{B}_i$$

   v) Calculate the new threshold,

   $$TH_{i,\,NEW} = TH_{i,\,CORR} = SC <\boldsymbol{B}_i \boldsymbol{I}_i> + L,$$

where the scaling factor SC is chosen by the user for each data set (typically, between 0.25 and 0.35) and the offset L is chosen by the user for each data set (= experiment).

c. **Corrector**: binarize $\boldsymbol{I}_\mathbf{i}$ by thresholding at $TH_{\mathrm{i,\,NEW}}$, Figure 30d

d. Remove small spurious regions of foreground by morphological operations

e. Set $TH_{\mathrm{i,\,PRE}} = TH_{\mathrm{i,\,NEW}}$ and go to the next image i+1('FW') (step a) or next image i-1('BW') (step a). 'FW' and 'BW' stand for 'Forward' and 'Backward' sequence respectively. The details of these operations are discussed in section 4.6.

The flow chart of the binarization scheme is shown in Figure 31. This flow chart divides the binarization procedure into 5 sections:

1. Input data management, which includes reading, importing, and arranging image data into a MATLAB workspace
2. Pre-processing step (blue box), which includes background subtraction, and filtering in spatial and frequency domains
3. Image thresholding by the Predictor-Corrector scheme (red box)
4. Post-processing, which includes binary morphological processes
5. Extraction of quantitative spatial information on the flame area, growth rate, and centroid location

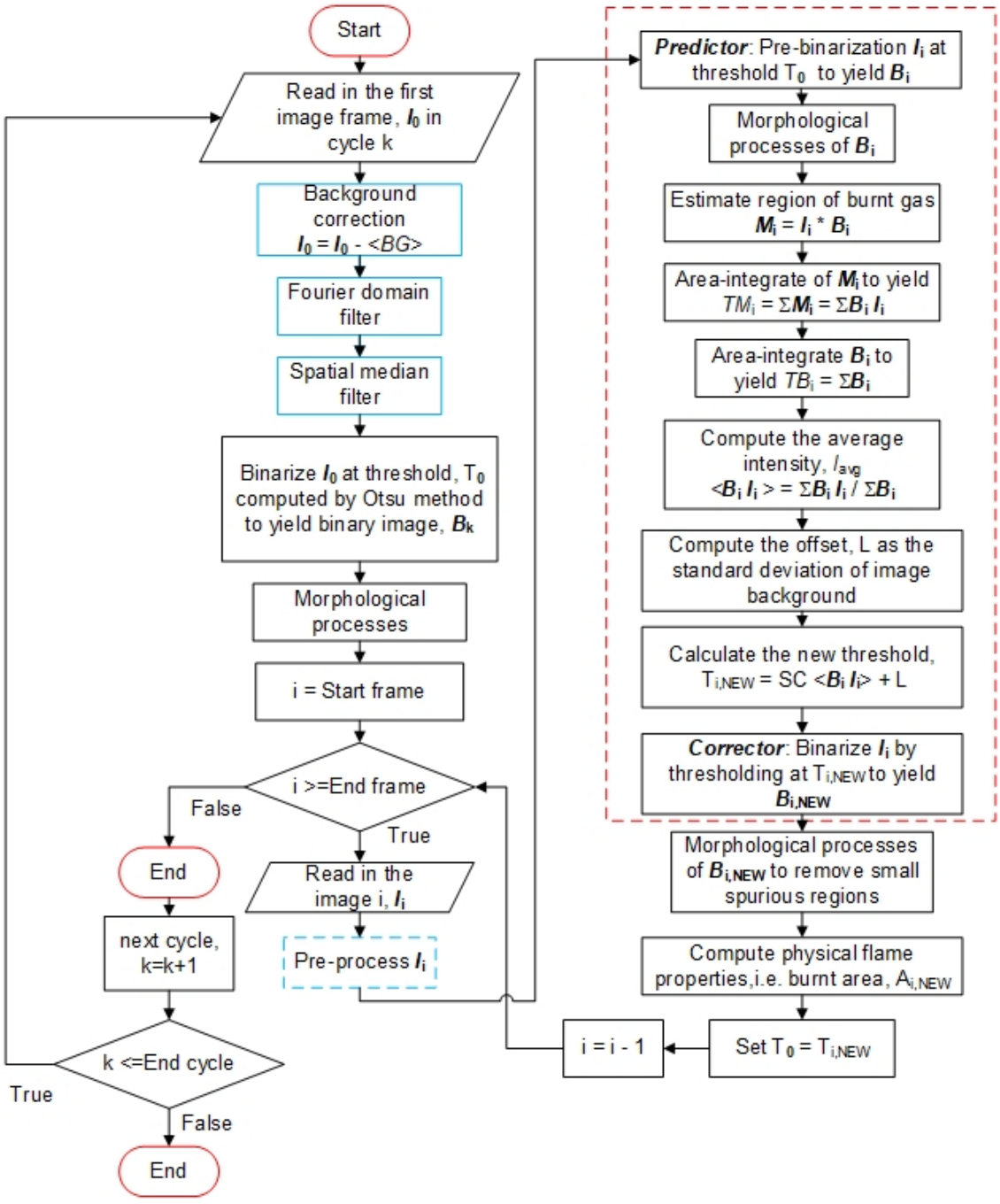

Figure 30: Flow chart of the automated dynamic thresholding algorithm.

4.5 Qualitative and quantitative results

In this section, the segmentation algorithm was tested with flame propagation images from endoscopic high-speed imaging in a production single-cylinder BMW/Rotax engine (F650 motorcycle series). The details of the optical arrangement and experimental work are discussed in chapter 5. This dataset consists of 200 combustion cycles, which contain 55 flame images each. The structure of the recorded high-speed image sequences is illustrated in Figure 27. Here, we also examine the "quality" of the quantitative morphological information that can be derived from the endoscopic high-speed image sequences.

4.5.1 Projected burnt area detection

Figure 32 shows a sample of flame propagation images from two individual cycles obtained by unintensified high-speed endoscopic imaging. The red line in each image indicates the projected flame boundary as detected by the binarization procedure. The corresponding projected burnt area (PBA) is indicated in the upper right-hand corner of each image. The images are shown *before* background subtraction to give the reader an impression of the pattern noise. However, for further processing the correction was done using Fast Fourier Transform (FFT) filtering.

By visual inspection, this algorithm performs significantly better than simply applying Otsu's method (which has the advantage of needing no user input) throughout the data set. We attribute this to the fact that step 4b in the PC procedure makes use of the time-correlated character of the images, whereas any method that operates on each individual image by itself is lacking information available from the previous image. Furthermore, the algorithm performs well even though the pattern noise was very obvious in the background-corrected images. Filtering in the Fourier domain was effective in suppressing this noise component to acceptable levels. The algorithm is capable of detecting early flame kernels despite the substantial variation in image brightness occurring within the relevant part of the cycle. This is particularly noticeable during the initial 10°CA after ignition timing (aIT), where bright spark events overlap in time and space.

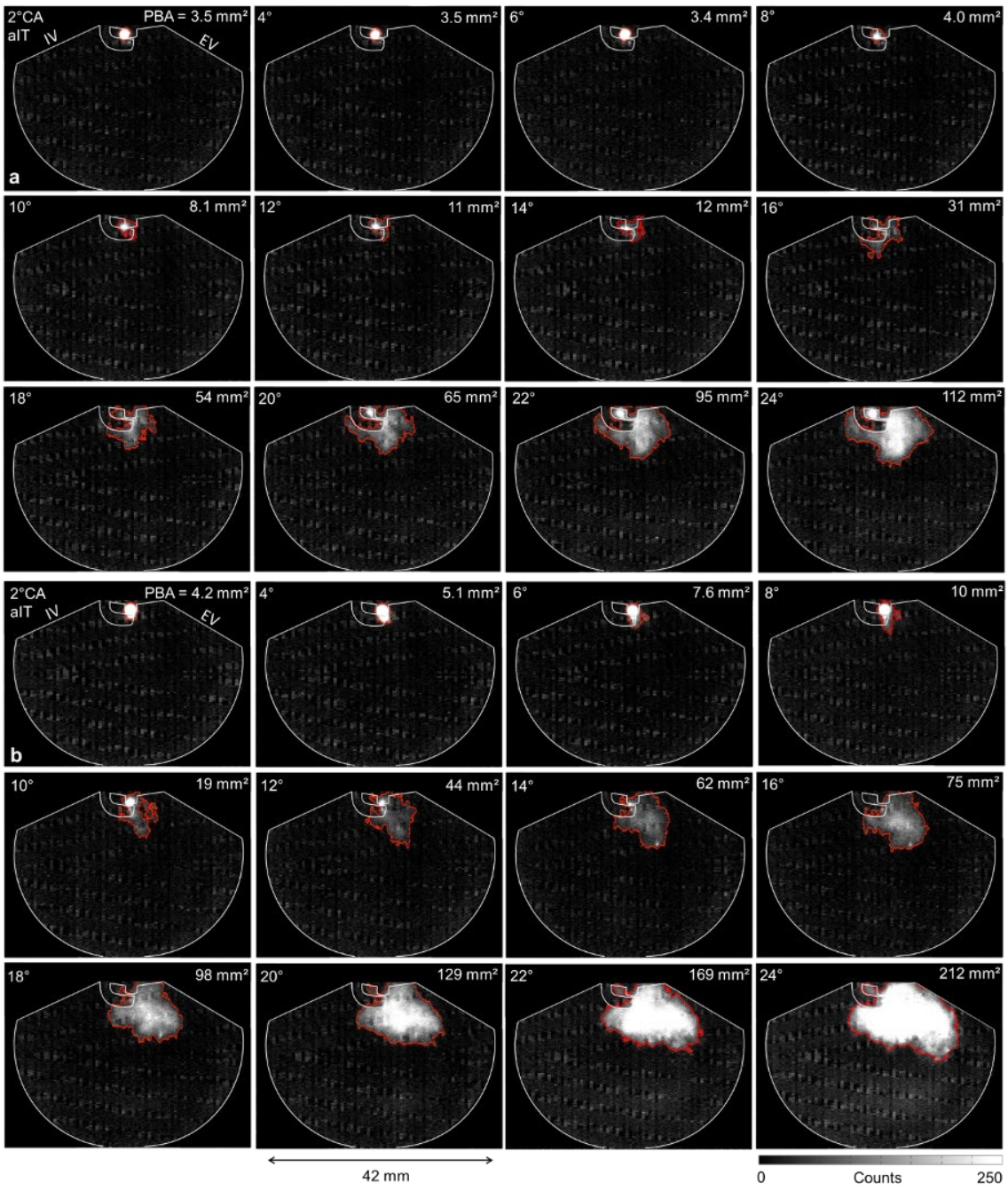

Figure 31: Sample of two individual combustion cycle from endoscopic high-speed imaging. Every second image from each time series is shown. The red line indicates the detected flame boundary using the PC algorithm. The corresponding projected burnt area (PBA) is indicated in the upper right-hand corner of each image.

The binarized images were also post-processed by morphological operations removing small spurious regions of foreground not connected to the main foreground. These regions appear at late crank angles

due to diffuse background reflection of flame luminosity by the cylinder wall. Similarly, small holes in that main foreground were closed. Although more aggressive morphological post-processing could potentially be used to further improve the binarization, here the parameters were chosen such that these operations had merely "cosmetic" character, i.e., they did not have significant influence on the results obtained. Figure 33 shows the result of binarization using an example image from the endoscopic imaging experiment. It is clear that the patterned read-out noise causes some uncertainty on a pixel level.

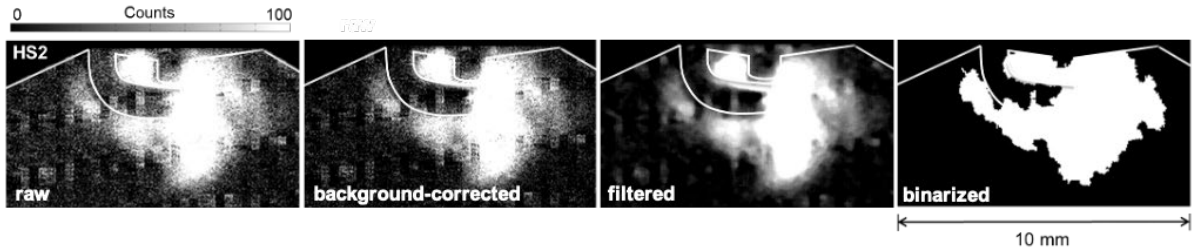

Figure 32: The binarization procedure illustrated with an example image from the single-cylinder motorcycle engine (cycle a at 24°CA aIT). In this case the greyscale limits are chosen to clip in regions of maximum signal such that the flame front and the noise can be seen more clearly.

The flame radius r_F was calculated from the foreground area A in the binarized images as $r_F = (A/\pi)^{0.5}$, i.e., as the radius of a circle with an area equivalent to that of the (irregularly shaped) projected burnt area detected in the images [47, 48]. Figure 34 presents the equivalent flame radius as a function of crank angle for all 200 combustion cycles. The multi-cycle mean is also shown (solid black line). As can be seen in Figure 34, the burned area mostly increases monotonically and the lines representing each cycle's flame-front progress rarely cross. The former is physically reasonable, and the latter has been observed before [20, 47, 87].

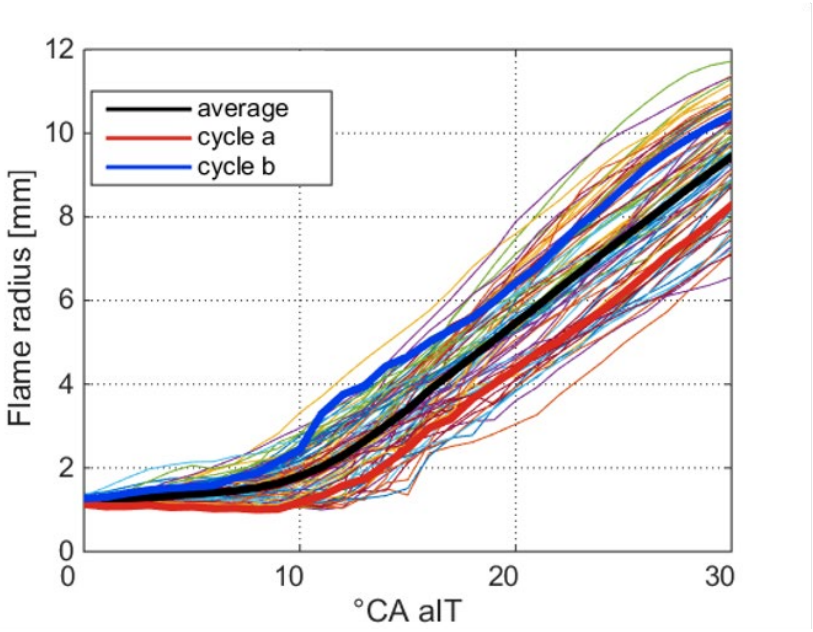

Figure 33: Equivalent flame radius for 200 consecutive cycles (colored lines) and the multi-cycle mean of these cycles (solid black line). Also highlighted are each of the two example cycles from Figure 32.

4.5.2 Sensitivity analysis

Apart from the preceding filtering's kernel size, the threshold calculation contains two free parameters, *SC* and *L*. The values for these were chosen based on visual inspection of the resulting binarization, such as the images in Figure 32 as well as a sensitivity analysis for some of the data sets. As an example of the latter, Figure 35 shows the equivalent flame radius for a single example cycle (b) in Figure 32. Other cycles lead to qualitatively similar results for a variation of SC. The flame radius r_F was calculated from the foreground area A in the binarized images as $r_F = (A/\pi)^{0.5}$, i.e., as the radius of a circle with an area equivalent to that of the (irregularly shaped) projected burnt area detected in the images [47, 48]. For Figure 35, we varied the scaling factor *SC* from 0 to 1.5 in increments of 0.05, while holding the offset *L* at a constant value of 5 counts. The flame boundaries delineated in Figure 32 and all other results from the data set were obtained with $SC = 0.35$, corresponding to the dashed black line. Figure 35 shows that indeed for values of about 0.35 the calculated flame radius is least sensitive to the choice of *SC*, although for crank angles before 10°CA aIT greater values appear to be a better choice. However, visual inspection of a few cycles showed that choosing SC significantly greater than 0.35 would have led to the very early flame kernel being detected too late. Admittedly, some arbitrariness remains, because at this stage of kernel development the intensity of the detected flame luminosity is close to the residual pattern and shot noise.

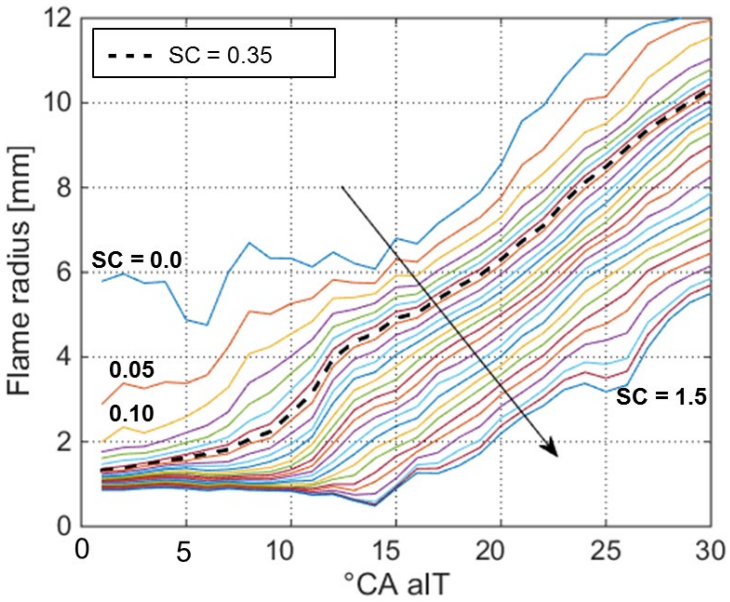

Figure 34: Sensitivity analysis of cycle (b) in Figure 32: Variation of the detected equivalent flame radius as a function of crank angle for a range of values for the scaling factor *SC*. *SC* increases in the direction of the arrow.

The offset L is mainly important at very low image brightness, when it stabilizes the dynamic binarization scheme. If the burnt area in a given cycle i is strongly over-assessed, in the next cycle i+1 in the PC step (a) the preliminary area is also too large and includes much image area with near-zero signal, yielding a very low updated threshold in the PC step (b) and consequently an even larger area in this cycle and the next cycle's PC step (a) – the procedure becomes unstable. In this case, $L = 5$ counts was selected, since this was the minimum offset required to reliably stabilize the algorithm. The combination $SC = 0.35$ and $L = 5$ counts was used for all unintensified imaging, while $SC = 0.5$ and $L = 12$ counts were found appropriate for the intensified endoscopic imaging experiment HS-OH*.

Figure 36 illustrates, why dynamic adjustment of the threshold is necessary: The threshold, which is essentially proportional to the average brightness level within the region labeled as burnt area, varies greatly not only during the imaged portion of the cycle, but also from cycle to cycle. The average threshold at ignition timing is 170 counts, decreasing to a minimum of 28 counts 17°CA later, and increasing back to 95 counts at 30°CA aIT. At that crank angle cycle (b) was thresholded at 145 counts, but cycle (a) at 80 counts. This difference corresponds to the significant difference in detected burnt area. After 30°CA aIT (not shown), both the absolute value of the average threshold as well as the variation between cycles increase another order of magnitude, but at these crank angles the detected burnt area is not necessarily linked to physical flame-front propagation anymore, because in an increasing number of cycles, the flame boundary reaches the edge of the FOV.

Interestingly, the “faster” cycle (b) initially has a lower threshold value (= lower brightness) than the “slower” cycle (a), but this order reverses at about 15°CA aIT. We speculate that the lower brightness is due to the fact that more of the spark’s energy has already been transferred to the surrounding fuel/air mixture. This is supported by Figure 32 showing that at 4 and 6°CA aIT in cycle (b) the bright area near the spark gap is larger than in cycle (a). However, there could also be obscuration by the spark plug, and we are examining two example cycles only here. Nevertheless, this observation illustrates the potential that lies in being able to observe both spark and early flame propagation in the same cycle.

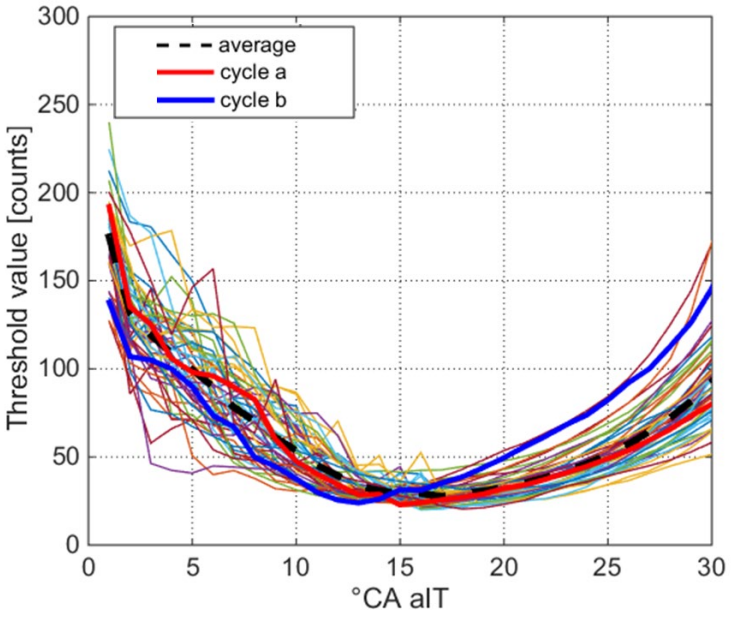

Figure 35: The computed threshold value as a function of crank angle for all 200 cycles.

4.6 Multi-level thresholding via forward and backward analysis

In the above description, the thresholding sequence is running **'forward'** (FW), i.e, in each PC step (e) i is incremented to i+1. But in fact, the reverse is possible as well, starting with the last flame image as $\boldsymbol{I}_1$ and working **'backward'** (BW) simply by using a loop increment of -1 in PC step (e). Because the predictor step (a) transfers information "in time", the FW result is not the same as the BW result. In particular, if two classes of foreground signals with very different intensities are present – such as the bright spark and the weak early flame kernel – the algorithms "locks" onto one of the classes. If the primary goal is to isolate the flame, the BW mode is preferable, because at late crank angles there is only the flame and no spark. Thus, when both FW and BW mode were utilized, the algorithm finds two threshold values for a given image and segments the image into certain brightness regions, which correspond to the bright spark, weak flame kernel, and background. This multi-level thresholding technique will be explored in more detail below.

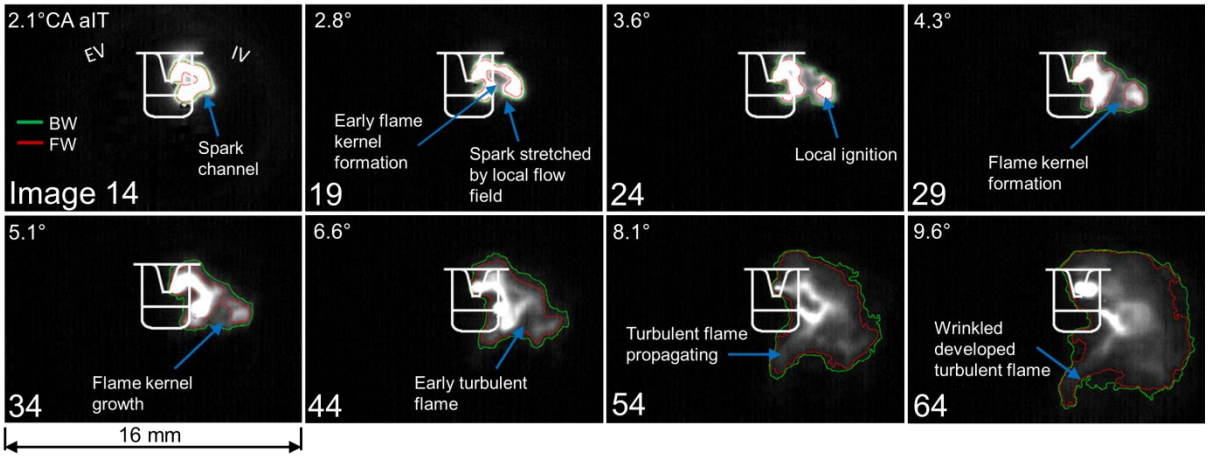

Figure 36: Endoscopic unintensified high-speed spark-ignition sequence. The red and green lines indicate the flame boundary as detected by the 'Forward' and 'Backward' method respectively. Image 0 corresponds to ignition timing.

Figure 37 shows a selected images from a single cycle of imaging with the Photron SA-Z camera at 75 kHz repetition rate. The red and green lines indicate the flame boundary as detected by sequential 'forward' and 'backward' binarization. Image 14 and 19 show the spark channel being stretched and corrugated by the local flow field. Flame kernels are initiated along the spark channel, detaching from the initial arc. The kernels continue to grow and transition into a turbulent flame.

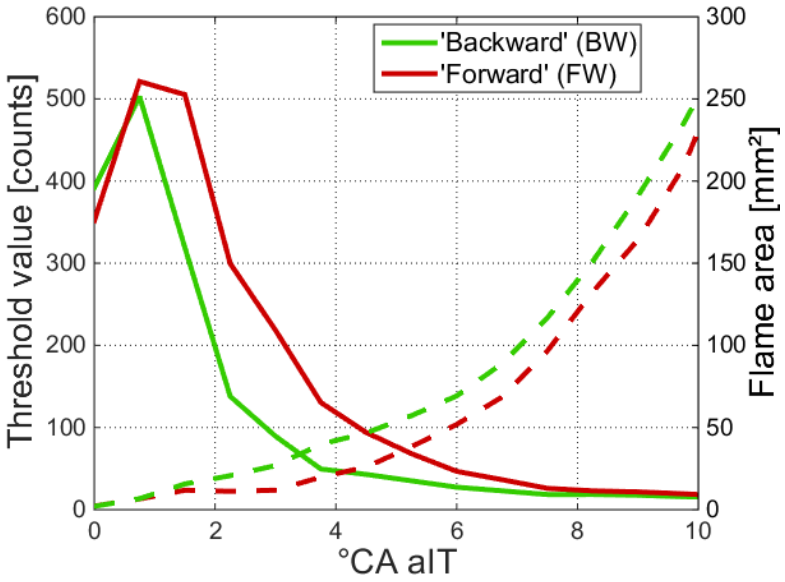

Figure 37: Computed threshold values (continuous line) and burnt area (dashed) vs. CA°aIT using the 'Forward' and 'Backward' binarization scheme

Figure 38 plots the computed threshold values as a function of crank angle for both FW and BW sequences. The FW threshold values are always higher than the BW ones, in particular between 1.5° to 6.5°CA aIT. In the FW mode, the first image input into the algorithm already shows the spark with its high intensity. Thus, in the next image, the predictor step (a) isolates again a region of high intensity, i.e., the spark. The corrector steps averages over this bright region, and arrives at another high estimate for the appropriate threshold. When a second class of lower-intensity foreground, i.e., the early flame kernel, starts appearing, the algorithm does not "find it" until the two intensity levels have become similar.

On the other hand, in BW mode, the first input image is the last image in the cycle, in which only the less bright flame is present. This allows the algorithm to lock onto the lower-intensity foreground class. Running the algorithm forward and backward, the two classes can both be isolated. At which relative brightness level the class separation occurs depends on the scaling factor SC and is somewhat arbitrary, but then again, any distinction between "late spark plasma" and "early flame kernel" might also be arbitrary.

4.7 Algorithm robustness

In this section, the robustness of the binarization algorithm was evaluated by processing different datasets with different levels of image quality (SNR). This evaluation aims to determine how effectively the algorithm performs across a spectrum of image conditions, thereby gauging its ability to maintain consistent and accurate results even when confronted with diverse image qualities.

4.7.1 Variation of camera and lens aperture

Four datasets imaged with two different camera systems were used to evaluate the robustness of the segmentation algorithm. The characteristics of the two cameras are summarized in Table 8.

Table 8: Camera specifications and parameters of the imaging systems. CU = achromatic close-up lens

	Phantom v7.3	**Photron SA-Z**
Pixel size	22.0 µm^2	20.0 µm^2
Read noise	21e$^-$ rms	29e$^-$ rms
Sensor size	17.6 x 13.2 mm^2	20.5 x 20.5 mm^2
Frame rate	6.7 kHz @ 800 x 600 px	20 kHz @ 1024 x 1024 px
Exp. time	20 µs	20
Rep. rate	11 kHz	20
Actual ROI	608 x 456 px	860 x 660 px
Projected pixel size	50 µm/px	35 µm/px
Lens system	50 mm F/1.2 with 250 mm close-up lens	50 mm F/1.2 with 250 mm + 500 mm close-up lens

In order to systematically evaluate the robustness of the image processing algorithm with respect to noise, datasets with different lens apertures, F/1.2, F/2.8, and F/5.6, were acquired using the Phantom v7.3 camera. Decreasing the relative aperture decreases the signal while the physical object of interest – spark and flame – remains the same.

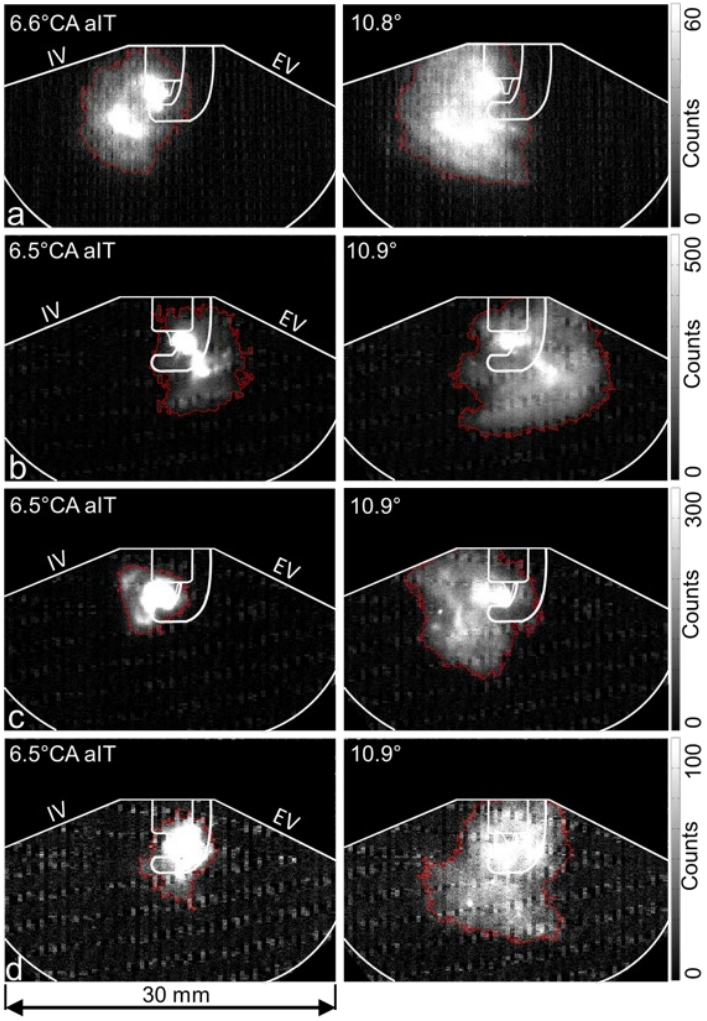

Figure 38: Sample of image series for different imaging system and lens aperture. The red line in each image indicates the flame front as detected by the binarization procedure. (a) Photron SA-Z, (b – c) Phantom v7.3 with the relay lens at (a) F/1.2, (b) F/2.8, and (c) F/5.6.

Figure 39a shows samples from the Photron SA-Z camera at the maximum relay lens aperture F/1.2. Compared to images from the Phantom v7.3 in Figure 39b, the image "quality" appears similar. This is consistent with the specifications listed in Table 8: Read-out noise is higher, but the sensor area is larger, and at low light levels, both read-out and photon noise are relevant. On a per-pixel level, however, the images from the SA-Z had a significantly worse signal-to-noise ratio (SNR) because of the smaller projected pixel size, or equivalently, the higher resolution. For further comparison, the SA-Z images were resized by a factor of 1.5, to 573 x 440 pixels, by interpolation. The projected pixel size is then nearly the same. Of course, the newer Photron SA-Z is much faster than the older Phantom v7.3, which can help analysing fast phenomena such as the spark, as discussed previously.

Figure 39b-d shows image samples from the Phantom v7.3 at different apertures. With reduced aperture, signal is lost, but not as much as the reduction in the entrance pupil would indicate. This is due to the fact that the relay lens is imaging off the field lens, which is not an isotropic light source, but directs the rays towards the relay. This particular CMOS camera shows a periodic and moving pattern in the read-out noise. To lower the pattern noise, we subtracted the mean of the last 10 dark images in each cycle before the spark from each image. The image sequence in Figure 39b show that this works quite well for the late crank angles after ignition, because of high signal intensity at this stage of combustion. However, in the early phase of combustion, the intensity of the flame kernel is close to the read-out noise. The effect of the periodic noise on images becomes more obvious for datasets at higher F-number (F/2.8 and F/5.6) for the same engine operating conditions, as shown in Figure 39c and Figure 39d, respectively. The red line indicates the border of the burnt area, identified by the binarization algorithm. The FFT filtering process increases the robustness of the algorithm for detecting the flame boundary at low light conditions.

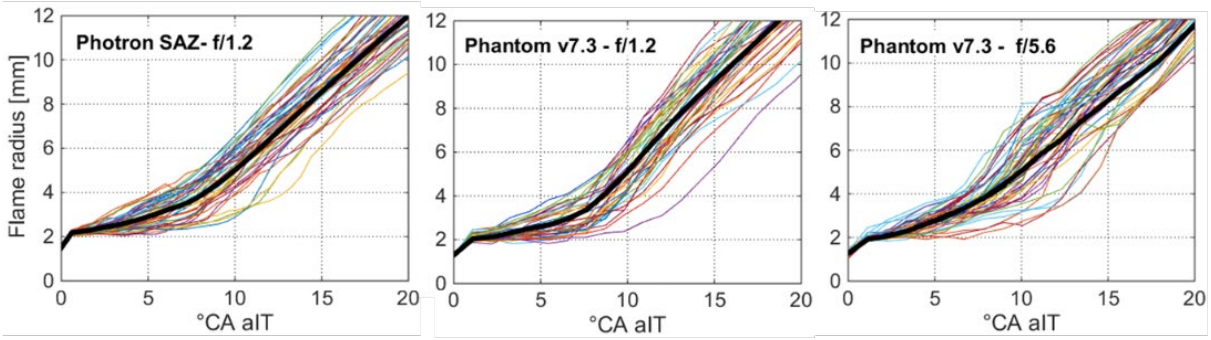

Figure 39: Flame radius for 50 consecutive cycles (colored lines) and the multi-cycle mean of these 50 cycles (solid black line). Camera systems used are indicated in each graph.

Figure 40 shows the equivalent flame radius as function of crank angle for the two cameras and for the Phantom v7.3 for the largest F-number. Consistent with the visual appearance of the images in Figure 39a and b, the two plots are very similar. There is a small systematic deviation, which may be due to slightly different thermal conditions in the engine. In both plots, scatter is low, and lines mostly do not cross, which is physically plausible [48, 125]. For the Phantom v7.3, results from F/2.8 are very similar to those from F/1.2, and (not shown) results without Fourier filtering are also similar. However, at F/5.6, Figure 40c, scatter at early crank angles appears despite Fourier filtering.

4.7.2 Comparison with existing edge detection schemes

In this section, the predictor-corrector thresholding scheme was compared with three popular automatic thresholding algorithms (Otsu's, gradient-based, and multi-thresh Otsu's) in terms of

detecting the boundary of projected burnt area (PBA). For the input images, the same image pre-processing step was applied before thresholding, thereby making their outputs directly comparable. For each algorithm, we consider its correctness based on visual inspection, as well as its stability with respect to different images with a wide range of brightness. All these methods are available in the MATLAB image processing toolbox function; *graythresh (I)*, *edge (I, method)*, *multithresh (I, level)* respectively. The accuracy of each detection scheme is presented in terms of the computed flame radius vs. propagating time.

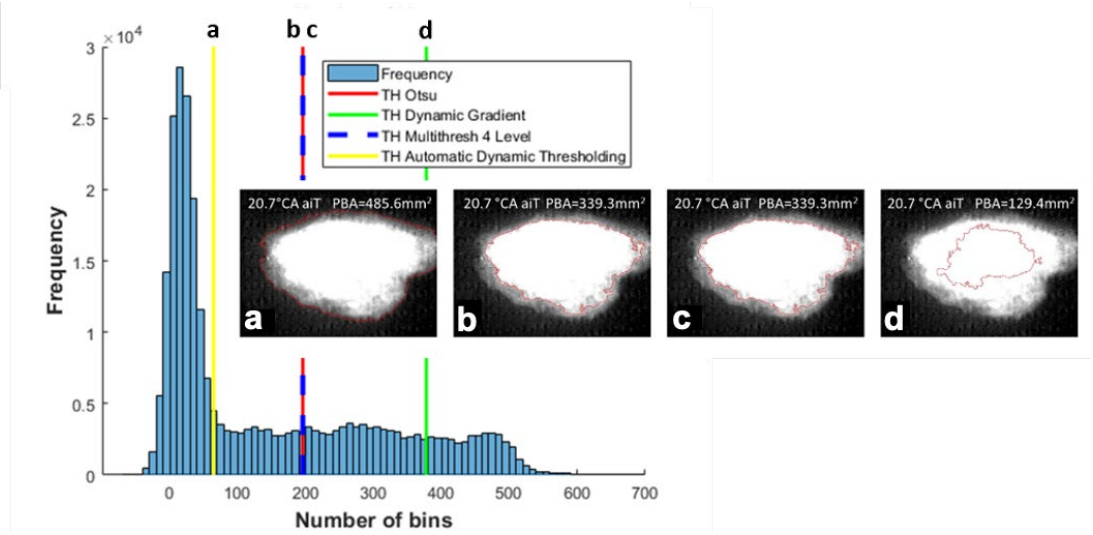

Figure 40: Computed threshold value from each thresholding scheme for flame image at 20.7°CA aIT. The red line in each image indicates the flame's boundary as detected by each binarization scheme. (a) PC, (b) Otsu, (c) multithresh Otsu, (d) dynamic gradient.

Figure 41 shows the intensity histogram of the image and the computed threshold value from each thresholding algorithm. Based on visual inspection and the correctness of the detected burnt area, the PC scheme computed the most precise threshold value among the available options. The global and muti-thresh Otsu's yield the same result, and dynamic gradient underestimated the burnt area. Figure 42 shows sample of an individual cycle of flame propagation images, and the detected burnt area resulting from each binarization scheme. By visual inspection, the PC algorithm consistently outperforms Otsu's method throughout the data set. This advantage can be attributed to the fact that the PC procedure makes use of the time-correlated character of the images, enhancing the algorithm's understanding of the data, and therefore maintains accuracy consistently across frames. In contrast, any method that operates on individual images only is lacking information available from the previous image. Otsu's method also strongly depends on the presence of bi-modal histograms for effective foreground object detection within the image. Nevertheless, Otsu's method works for certain images,

but not consistent throughout the dataset. As expected, the dynamic gradient method gives the worst result in terms of detecting the 'correct' flame boundary. This algorithm adaptively determines edge locations within an image by considering the changing gradient characteristics across varying regions of brightness. Unlike Otsu's method, the dynamic gradient edge detection adjusts the threshold values based on the local contrast and gradient information present in the image. As a result, the algorithm struggled to accurately distinguish edges and gradients across images with significantly different brightness levels.

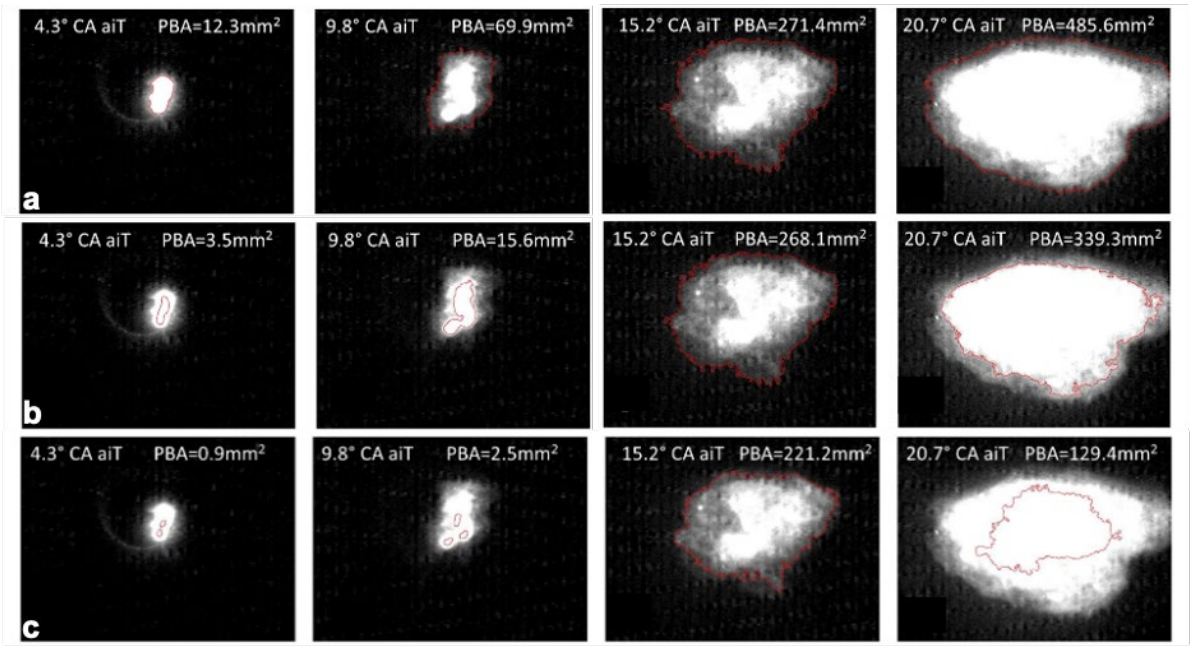

Figure 41: Sample of an individual cycle of a flame propagation image. The red line indicates the burnt area as detected by each binarization scheme. (a) PC algorithm, (b) multithresh Otsu, (c) dynamic gradient.

Chapter 5 High-speed imaging of flame chemiluminescence using selected imaging systems via endoscopic and full optical access

This work investigates the image quality achievable with a large-aperture endoscope system and high-speed cameras in terms of detecting the premixed flame front in spark-ignited engines. The study is an extension of the previous work on endoscopic flame imaging [85], which primarily focused on phase-locked snapshot imaging with intensified CCD cameras. In the present work, two different high-speed camera systems were used together with the endoscope system in two production engines to quantify the time-resolved flame propagation. The systems were cinematography with a CMOS-camera, both with and without an intensifier, the latter variation being used in a four-cylinder automotive engine as well as in a single-cylinder motorcycle engine. The kHz repetition rate of the CMOS camera systems allows following the flame development in each single cycle with sub-crank-angle temporal resolution. Together with the corresponding cycles' pressure traces, a wealth of detailed information on combustion can be acquired in little time. A fundamental problem in evaluating the systems' efficacy is that it is not clear what constitutes "correct" detection of the flame boundary. To help clarify this question, the endoscopic results are compared among each other and to a "best-case scenario", which was based on unintensified high-speed imaging with a large-aperture commercial camera lens in an engine with full optical access.

The endoscopic imaging datasets utilized in this study were acquired by Martin Goschütz, while the imaging dataset from the fully optical research engine was obtained by Martin Schild. The entirety of image post-processing and statistical analysis was performed by the author of the thesis. The findings of this study have been published in Ref.[14].

5.1 Experimental setup

5.1.1 Engines

Endoscopic imaging was performed in two production spark-ignition engines from BMW, an automotive 4-cylinder engine and a single-cylinder motorcycle engine, both port-fuel for premixed stoichiometric combustion. Although the data examined here are from part-load operation, both engines could still be operated over their full speed and load range with the endoscopes in place. At throttled part-load, flame-front imaging is more challenging than at high loads because the chemiluminescence light emission from the flame in the less dense air/fuel mixture is less intense [85]. In addition to endoscopic imaging, we also acquired similar image series in a fully optically accessible single-cylinder research engine (AVL, Graz), utilizing that engine's large optical access for "conventional" lens-on-camera imaging. Parameters and operating conditions for both optical and production engines are summarized in Table 9.

Table 9: Engines parameters and operating conditions.

Engine	**4-cylinder automotive (endoscopic)**	**Single-cylinder motorcycle (endoscopic)**	**Research engine (full optical access)**
Cylinders	4, inline	1	1
Compression ratio	10	10.8	10
Displacement [cm^3]	499	652	499
Bore [mm]	84	100	84
Stroke [mm]	90	83	90
Speed [min^{-1}]	2000	1500	1500
Fuel	Iso-octane	RON 95	Iso-octane
Rel. fuel/air-ratio		1.0	
Ignition timing [°CA]	-34.5	-45	-45
IMEP [bar]	4.4	3.8	2.2

5.1.1.1 4-cylinder automotive engine

The automotive engine, operated at the Institute for Energy and Materials Processes (EMPI) of the University of Duisburg-Essen, was the BMW 4-cylinder model N46B20. The details of the engine test bench are described in Chapter 3.1.

5.1.1.2 Single-cylinder motorcycle engine

Additional endoscopic imaging was carried out in a production single-cylinder engine produced by BMW/Rotax for the F650 motorcycle series. The engine at the Institute for Combustion Engines (IFKM) of KIT had phase shifters for intake and exhaust. The engine speed was controlled by a dynamometer, while load, cam phasing, injection and ignition parameters were controlled with the prototype engine control system ADWin Pro II. The valve lifts for intake and exhaust were 10 mm and the engine was throttled to intake pressures of 700 mbar at 1500 min^{-1}. Despite the modest throttling, the engine's indicated mean effective pressure (IMEP) was only just under 4 bar, presumable due to valve timings optimized for high-rpm performance.

5.1.1.3 "Optical" research engine

At the EMPI, similar experiments were then also performed in a fully optically accessible single-cylinder gasoline engine (AVL Graz) with a pent-roof four-valve head and a flat piston top. The engine was operated on premixed air/fuel charge, throttled to an intake pressure of 700 mbar. Additional throttling by reduced lift of the intake valves (3.0 mm) and the exhaust (3.5 mm) valves resulted in a part-load condition with even less IMEP than that in the endoscopic experiments.

5.1.2 Imaging system

5.1.2.1 Endoscopic system

In this study, the hybrid endoscopic system was used together with a high-speed camera with and without intensifier. The details of the endoscopic system are described in Chapter 3.3. A schematic drawing of the endoscopic imaging systems is shown in Figure 43a. The single-cylinder motorcycle engine was modified to receive the same endoscope, which protruded through the timing belt's casing.

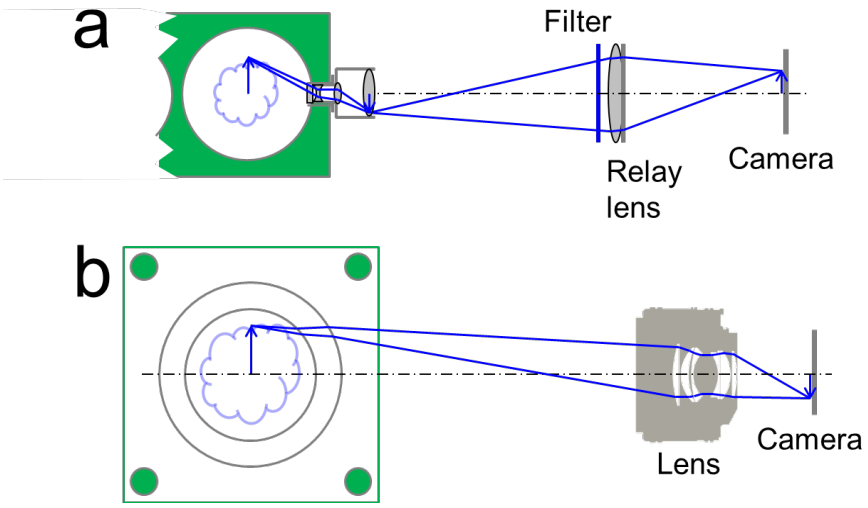

Figure 42: Schematic diagram of imaging with (a) endoscopic access and (b) large optical access.

With this endoscope system, imaging was carried out in three different experiments, whose detection-train characteristics are summarized in Table 10. Additionally, imaging with a high-speed CMOS camera and a commercial large-aperture lens was performed in the optical research engine, as detailed in a section below.

Table 10: Main parameters of the imaging systems.

Imaging system	**Endoscopic, intensified (HS-OH*)**	**Endoscopic, unintensified (HS1)**	**Endoscopic, unintensified (HS2)**	**Full optical access, unintensified**
Camera type	ICMOS	CMOS	CMOS	CMOS
Repetition rate (Hz)	6688	11019	9009	18018
Exposure time (µs)	20	20	29	15
Spectral window (nm)	300 – 335	400 – 800		400 – 800
(Relay) lens system	Hybrid R-DO	50 mm F/1.2 + 250 mm close-up lens		50 mm F/1.2
ROI (pixels)	800 x 600	608 x 456		512 x 312

5.1.2.2 Intensified OH* chemiluminescence via endoscopic imaging

Since chemiluminescence of OH* is usually considered to be a good marker of the high-temperature zone in premixed combustion, our initial experiments were aimed at using this species' UV chemiluminescence for flame-front visualization [85]. In the "intensified high-speed" configuration, OH* visualization was performed with an active-pixel sensor CMOS camera (Phantom v7.3), lens-coupled to an image intensifier with a UV-sensitive S-20 photocathode (LaVision). A bandpass filter transmitting from 300 – 335 nm preferentially transmitting OH* chemiluminescence from the strong bands at about 310 nm. The detector's full array of 800 x 600 pixels was read out at a repetition rate of 6688 Hz, approximately corresponding to one image per 1.8°CA at 2000 rpm. Based on the pixel number, among the ones considered here, this detection scheme would be expected to yield the best spatial resolution, but in fact the high-speed image intensifier degrades the resolution significantly, as will be seen in the results. The intensifier was gated to yield an exposure time of 20 µs. This experiment in the 4-cylinder engine will be designated "HS-OH*".

5.1.2.3 Unintensified high-speed cinematography (HS1 & HS2)

These measurements were performed with the same CMOS camera, but without the intensifier and the band pass filter. The CMOS detector itself is most sensitive in a spectral range between 400 and 800 nm. Such broadband sensing in the visible mainly detects the luminescent species CH*, CO*, CO_2*, and H_2O, not all of which are directly associated with the flame front. A Nikon 50 mm, F/1.2 lens combined with an achromatic close-up lens (Canon 250D) relay-imaged the endoscopic field-of-view onto 608 x 456 pixels. Reducing the readout area (ROI) of the detector allowed increasing the repetition rate. For experiment "HS1" in the 4-cylinder automotive engine, it was set to 11019 Hz (1.089°CA per image) at 2000 rpm, while for "HS2" in the single-cylinder motorcycle engine 9009 Hz correspond to 0.999°CA per image at 1500 rpm. Note that the seemingly odd numbers are due to the fact that the camera could only operate with stable read-out characteristics at certain fixed combinations of repetition rate and ROI. We increased the exposure time from 20 µs for HS1 to 29 µs for HS2, since results from HS1 had indicated that detecting the flame front in the unintensified images was more limited by the low signal-to-noise ratio than by motion blur.

5.1.2.4 Imaging with large optical access (HS)

In the optical engine (experiment “HS”), the entire upper part of the cylinder was from fused silica, which enabled viewing the pent-roof combustion chamber and the complete width of the bore to about 29 mm down from the fire deck. Again, the CMOS camera was used without intensifier and filter, like in HS1 and HS2. However, the same commercial f/1.2-lens now directly projected the FOV onto 512 x 312 pixels, as shown in Figure 43b. The exposure time was set to 15 µs. At 1500 rpm, the repetition rate of 18 kHz corresponds to one image per 0.5°CA.

5.1.3 Pressure trace analysis

The crank-angle resolved pressure in intake, exhaust, and cylinder was recorded in all experiments. For the current work, the results of pressure-trace analysis only will be presented for HS2 in the single-cylinder motorcycle engine. The analysis at the IFKM was based on a zero-dimensional model. The in-cylinder mass was determined in a gas exchange calculation, in which the residual gas mass was computed with the thermodynamic conditions of intake port, exhaust port, and cylinder and the separately determined flow coefficients of intake and exhaust valves. From the pressure trace, the burn rate and the burned fuel mass fraction were calculated using a two-zone model. The wall heat transfer was modelled with the theory of Hohenberg because it gave the best fit in compression phase. Blow-by was assumed to be 0.4% of the cylinder charge.

5.2 Results and discussion

In this section, we will first show and qualitatively discuss example image series from intensified and unintensified high-speed cinematography in the 4-cylinder automotive engine HS1, then compare these endoscopic images to those obtained from the less challenging case of full optical access. The case HS2 is discussed last. We then present an algorithm to binarize the images to obtain the instantaneous location of the flame front. Identification of the flame front allows calculating the apparent flame speed, which we compare between all four experiments, and other derived statistics, a few of which are presented for the case HS2. For this experiment, we also check if the optical measurements correlate with the pressure-trace analysis as expected.

5.2.1 Example images series

5.2.1.1 Intensified high-speed cinematography (HS-OH*)

Images from and qualitative discussion of this experiment were already included in Ref.[85], but are partially reproduced here for completeness. Figure 44 shows two series of OH* CL images from intensified high-speed endoscopic imaging. To reach kHz repetition rates, compromises have to be made in the design of image intensifiers, and similarly CMOS cameras optimized for extremely fast read-out are noisier than “slow” CCD or CMOS detectors. In particular, the strong emission from the spark impacts parts of the image that are several millimetres away. The spark’s luminosity is not due to OH* [48, 89], but other species that either emit within the transmission band of the filter or have emission strong enough to “leak” through the filter in its spectrally blocked range. This suggests that the seemingly large spatial extent of the spark signal is solely due smearing by the high-speed image intensifier.

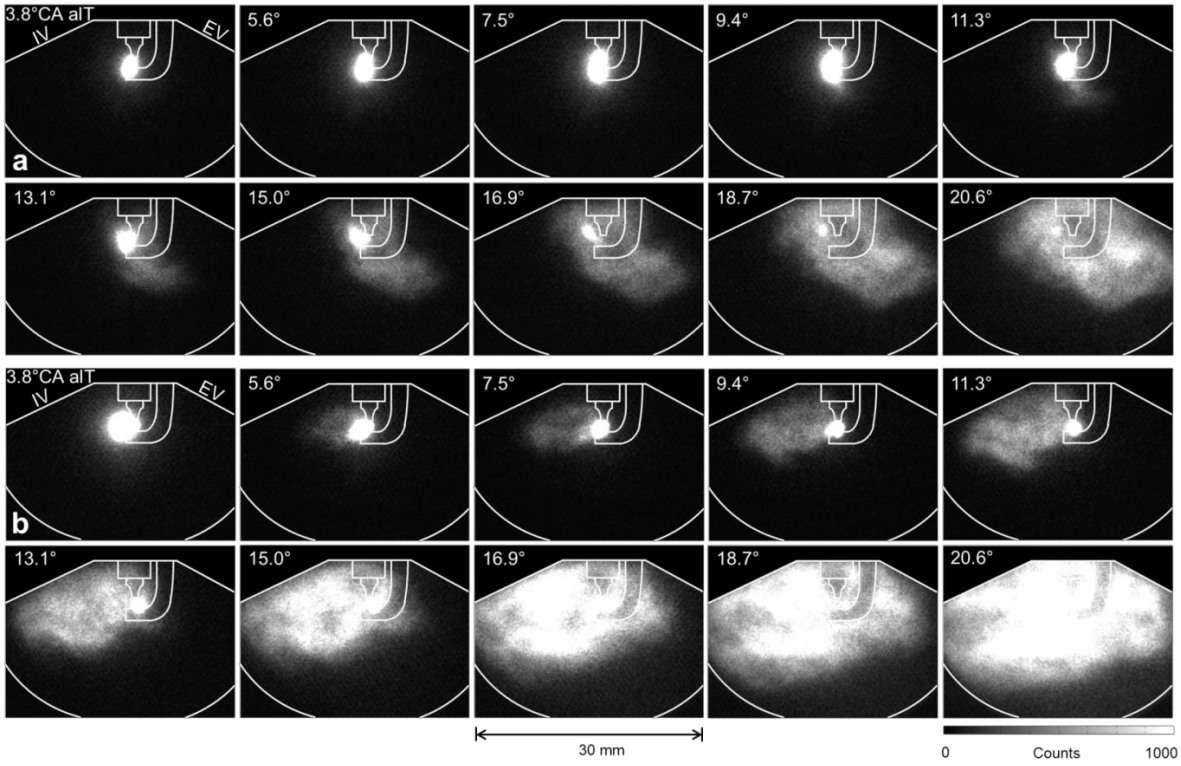

Figure 43: OH* chemiluminescence in endoscopic intensified high-speed cinematography (HS-OH*): (a) slower cycle, (b) faster cycle. Every second image from each time series is shown.

Despite the limited spatial resolution of the images, a few qualitative observations can be made. The delay between spark initialization and the onset of discernible flame propagation differs between the two sample sequences. In the first series during about the first 10°CA aIT, only the spark can be seen, while in the second one an irregularly-shaped flame emerges from the saturated part of the image at 5.6°CA aIT. Correspondingly, by the end of the second sequence the burnt area fills a much greater portion of the FOV. Overall, the early flame front develops faster in cycle (b) than in cycle (a). Both series confirm a key finding of previous research, [47, 89] that flames keep their shape while growing. The main direction of convective displacement in these sequences is evident as well and is different between the two sequences, a clear indication of significant cycle-to-cycle variability in the flow field near TDC.

5.2.1.2 Unintensified high-speed cinematography (HS1)

Figure 45 shows two sequences of flame propagation from endoscopic unintensified high-speed cinematography in the 4-cylinder automotive engine, HS1. As opposed to the images in Figure 44 details of the spark are discernible here. Although the ignition event itself was not our primary interest here, much can be learned from imaging the spark channel [48, 89], therefore this could be a significant advantage over intensified imaging. The lack of an intensifier-induced “halo” means that the flame kernel can be distinguished from the spark earlier. However, without the analog amplification of the intensifier upstream of the CMOS-detector the signal is much closer to the read-out noise of the detector. The CL in the visible part of the spectrum detected here may also not be as strong as the UV emission of OH* detected by the bandpass-filtered intensifier (Figure 44).

This particular camera shows a pattern in the read-out noise that is spatially shifting with time. To obtain the lowest noise floor in those images that capture the weakly luminescent nascent flame kernel, we subtracted the mean of the last 10 images in each cycle before the spark from each subsequent image. Both sequences in Figure 45 show that this works quite well for the first few crank angles after ignition, but later, the pattern has shifted too much and cannot be fully compensated. As a result, the edge of the burned area is “ragged”. For later crank angles, the increase in signal partially compensates the concurrent increase in residual background noise. As for Figure 44, also for Figure 45, we have chosen a faster and a slower cycle, which again differ both in crank-angle of first flame emergence and the apparent burnt area at the end of the sequence.

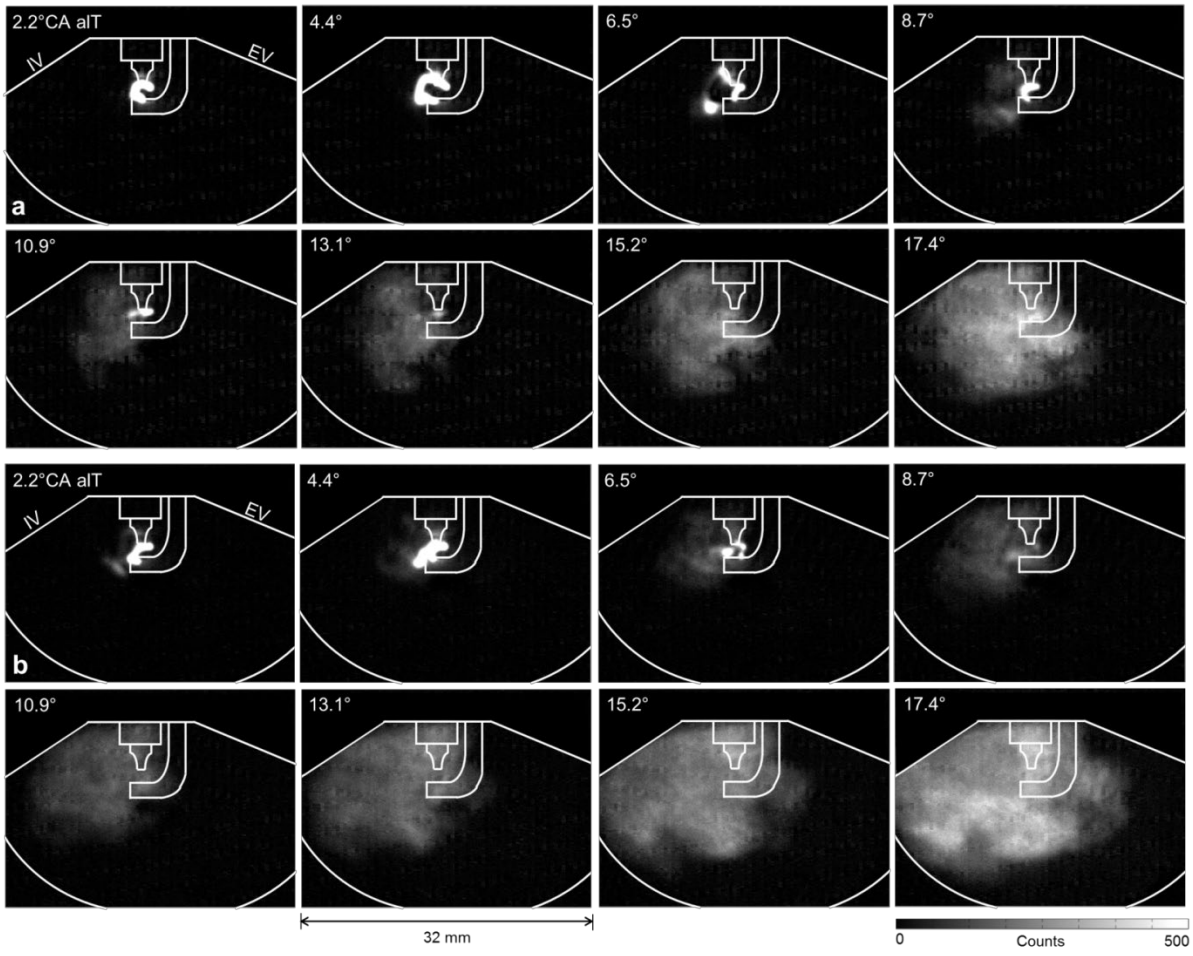

Figure 44: Endoscopic broadband cinematography HS1: (a) slower cycle, (b) faster cycle. Every second image from each time series is shown.

5.2.1.3 High-speed cinematography in the "optical" engine (HS)

The image sequences in Figure 46 show the image quality that can be achieved when the optical access is nearly unrestricted. Despite even higher frame rate and thus reduced detector area, as well as lower IMEP, the detected signal is about twice as high as in HS1. Indeed, if we assume that the CL signal per unit time is proportional to IMEP and engine speed, multiply by each imaging systems' collection efficiency (calculated from the values in Table 10 and the corresponding text), as well as the exposure time, we estimate that HS should yield 2.3 times the signal of HS1. The images also appear sharper than those in Figure 44 and Figure 45, but this is not necessarily due to better spatial resolution of the non-endoscopic imaging system, but rather because the read-out pattern noise is less important compared to the higher signal. Also, at the given reproduction size in this figure, the wider FOV gives the impression of a sharper image. The spatial features are similar to those seen in the

endoscopic production engine, but the three-prong spark plug in the optical engine seems to obscure the spark to a large extent.

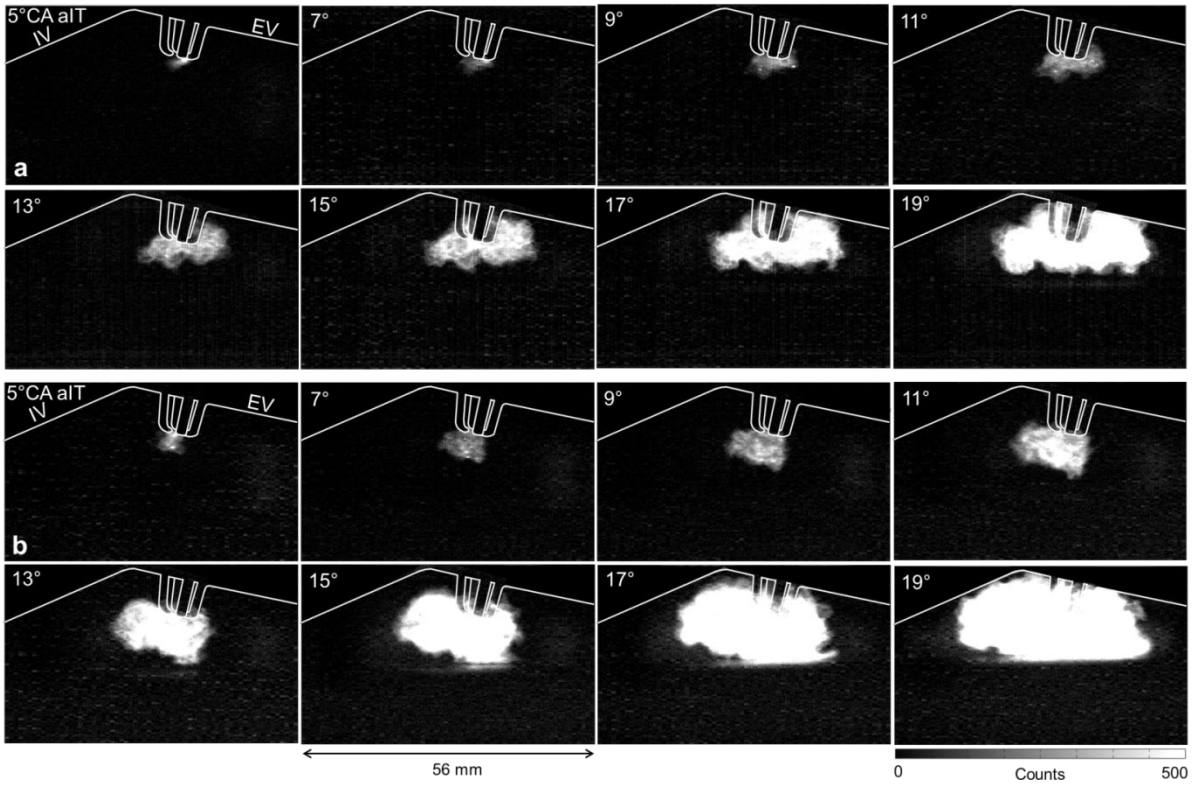

Figure 45: Unintensified broadband cinematography in the EMPI research engine: (a) slower cycle, (b) faster cycle. Every fourth image from each time series is shown.

In series (b) of Figure 46, we can clearly see the flame boundary reaching the piston top between 13° and 15° aIT. From then on, the luminous area is sharply limited by a horizontal border. (The image at 15° reveals that the lowest part of the luminous area is actually a reflection from the piston top's flat fused silica window that allows optical access through the slotted Bowditch-type piston. In the later images it is still possible to distinguish the flame from its reflection when the image is displayed at a more suitable brightness.) Images from the endoscopic experiments never show such a clear lower boundary, even when the flame can be expected to have impinged on the piston. The difference is due to the much wider viewing angle of the endoscope, about 60° compared to less than 15° for the case of imaging in the optical engine. The wide viewing angle (or equivalently, the short distance of the endoscope to the object) also introduces a systematic error in the burnt area estimated from the images. In our previous work, we estimated that in endoscopic imaging, the burnt area appears up to 15% larger than it does in the optical engine. However, for the crank angles aIT examined here, 5% perspective error are more typical [85].

5.2.1.4 Unintensified high-speed cinematography (HS2)

Figure 47 shows a slower and a faster cycle from endoscopic unintensified high-speed cinematography, HS2. The red line in each image indicates the projected flame boundary as detected by the binarization procedure, which is detailed in dedicated section below. As opposed to Figure 45 (HS1), the images in Figure 47 are shown *before* background subtraction to give the reader an impression of the pattern noise. (For further processing the correction was then applied as before.)

As in Figure 45 (HS1), also in these unintensified image series HS2 the spark is discernible with more detail than in the intensified images in Figure 44, but not quite as well as in the former case. In this engine, the endoscope is positioned lower in the cylinder head than in the 4-cylinder automotive engine. Correspondingly, while in HS1 the spark appears near the center of the image, it is out of the center here in HS2, where the resolution of the endoscope is not as good as in the center [33] and flare from the very bright spark is more pronounced. Away from the image center vignetting also reduces the image brightness, which is most critical during the early flame-kernel development with its weak luminosity.

Once the flame is established, the images from HS2 are quite similar to those from HS1. The flame boundary seems slightly sharper in the HS2, but as in Figure 46 this may be due to the lower magnification, which in turn is due to the larger bore of the motorcycle engine. Qualitatively, even accounting for the larger FOV, the projected burnt area increases slower than in HS1. The procedure to quantify this flame growth rate is presented in the next section.

In the last two images of each series in Figure 47, particularly at 24°CA aIT in cycle (b), an area of elevated brightness can be seen in the lower right part of the images. This is probably a reflection of the flame on the piston top. For later crank angles, which were of less interest here, this reflection can complicate the downstream image analysis. It is also of practical interest to note that it was quite difficult to attribute this bright area to a particular spatial feature and optical effect, a problem that we have experienced in other endoscopic experiments as well and is partly attributable to the wide viewing angle.

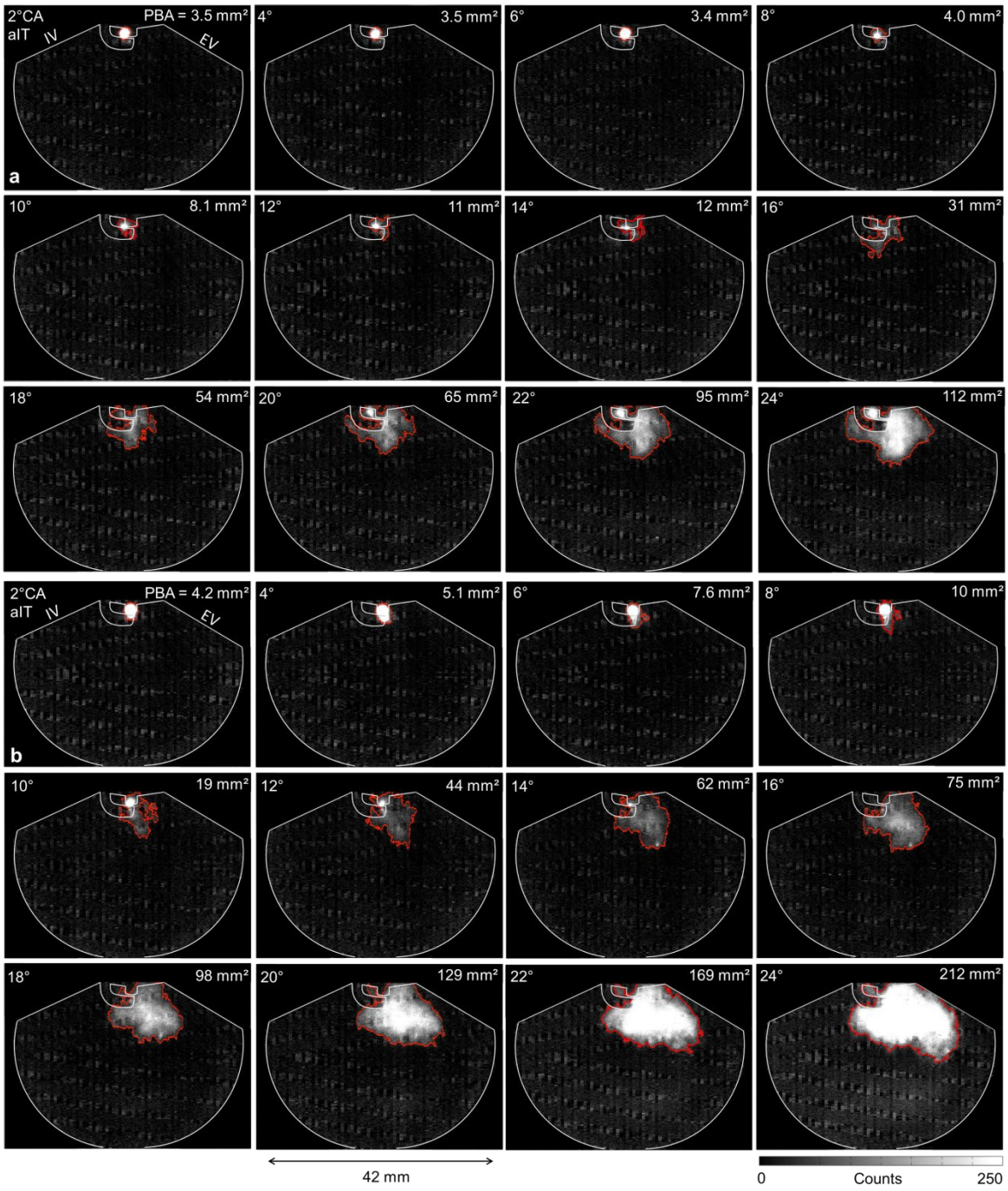

Figure 46: Endoscopic unintensified cinematography HS2: (a) slower cycle, (b) faster cycle. Every second image from each time series is shown. The red line indicates the projected flame boundary, the corresponding projected burnt area (PBA) is indicated in the upper right-hand corner of each image.

5.3 Quantitative results

In the remainder of this section, we will examine the "quality" of the quantitative morphological information that can be derived from the endoscopic high-speed image sequences. All datasets were post-processed using the PC binarization procedure (Chapter 4). Since in general it is not known what would be the "correct" location of the flame boundary, we first compare the flame radius measured by the three endoscopic experiments among each other and with the reference case of the fully optically accessible engine. We then examine, in how far projected burnt area and flame growth rate are consistent with the pressure-trace analysis and physical expectation. For brevity, this latter part of the analysis has been restricted to the case HS2, and only to a few simple statistics.

In this section, we will compare the endoscopic images to those obtained from the less challenging case of full optical access, in terms of detecting the flame boundary. We then present an algorithm to binarize the images to obtain the instantaneous location of the projected flame boundary and thus the projected burnt area. Identification of this boundary allows calculating the projected flame growth rate in terms of the equivalent flame radius, which we compare between all four experiments, and other derived statistics, a few of which are presented for the case HS2. For this experiment we also check if the optical measurements correlate with the pressure-trace analysis as expected.

5.3.1 Inter-experiment comparison

Figure 48 presents the equivalent flame radius as function of crank angle for all four combinations of engine and imaging system. Their multi-cycle mean is also shown (dashed line). All four plots in Figure 48 are similar in that mostly the burnt area monotonically increases and the lines representing each cycle's flame-boundary progress do not cross. The former is physically reasonable and the latter has been observed before [20, 47, 87]. Imaging in the optical engine, Figure 48c, shows these finding most clearly. We therefore consider this the "most correct" result, which was expected and is consistent with the good visual impression of the images from this experiment.

Compared to this baseline, the intensified endoscopic measurement HS-OH* shown in Figure 48a has the most scatter at early crank angles. Many traces, also those of the two highlighted cycles, cross. Also, in the mean, the projected burnt area does not expand between 4 and 8°CA aIT, with many cycles showing a period of a seemingly receding boundary. Inspection of the raw images indicates that for this part of the cycle, the burnt area is overestimated as consequence of the detector smearing out the saturated area caused by the spark luminosity. After 8°CA aIT, scatter is reduced. Our previous work showed that, as expected, for this later part of the cycle the multi-cycle mean of HS-

OH* nearly matches the phase-locked mean from a single-shot imaging method discussed in Ref. [85].

In contrast, scatter from the unintensified endoscopic data HS1 and HS2 in Figure 48b and d, respectively, is more consistent over the measurement duration. Thus, compared to the intensified version, the variance during early flame development is lower. This is because the spark causes only very local saturation of the detector. Again, the multi-cycle average roughly matches the phase-locked single-shot mean. The greater scatter at late crank angles (and compared to HS, Figure 48c, at all crank angles) shows the influence of the read-out noise pattern on edge detection. Compared to HS-OH*, HS1 also seems to indicate that the flame growth accelerates after 15° aIT. This is probably due to the effect of increasing flare as the flame boundary fills the FOV. The internal surfaces of this version of the front endoscope are stainless steel, which is more reflective in the visible than in the UV. We have since blackened them, but the same is true of the cylinder liner, whose surface we cannot influence.

Compared to the other two sub-figures, Figure 48c, representing data from the optical engine, shows markedly different traces for crank-angles before 8°CA aIT: the projected burnt area smoothly increases from zero in the latter case, while the former two indicate non-zero values immediately after IT. The difference is due to the spark-plug geometry: The spark is mostly hidden by the three prongs of the optical engine's spark plug. This may be beneficial or detrimental, depending on the desired information. In the endoscopic methods, it would also be possible to mask out the spark by placing a spatial filter (a black dot, in essence) onto the front endoscope's field lens, where a real intermediate image is formed.

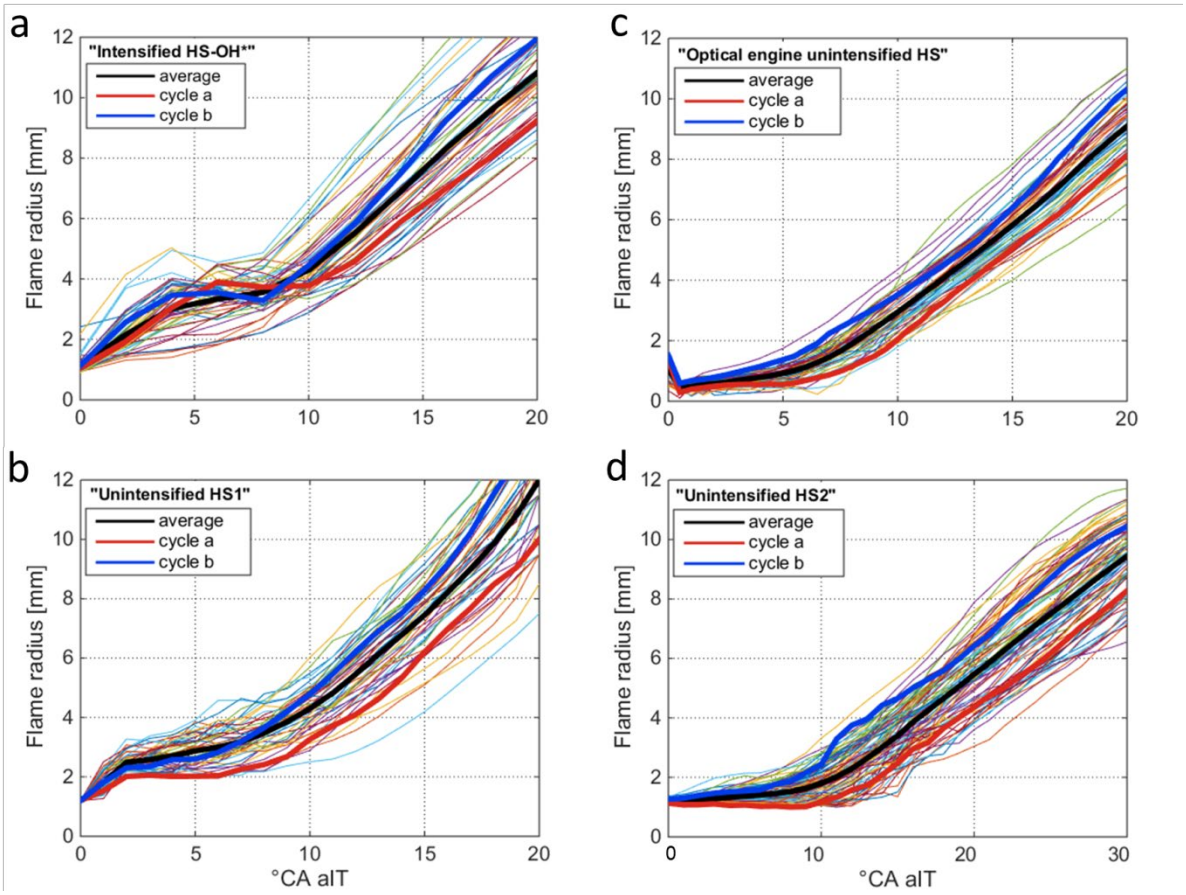

Figure 47: Equivalent flame radius for many consecutive cycles (colored lines) and the multi-cycle mean of these cycles (solid black line). Also highlighted are each of the two example cycles from Figure 44 to Figure 47.

a. Endoscopic intensified cinematography HS-OH* (50 cycles)
b. Endoscopic unintensified cinematography HS1 (50 cycles)
c. Unintensified cinematography in the research engine (100 cycles)
d. Endoscopic unintensified cinematography HS2 (200 cycles)

The two most similar cases in terms of their optical arrangement are HS1 and HS2 in Figure 48b and d, respectively. We can therefore expect that differences in the two plots correspond to physical differences between the two engines. Three main points can be noted: (1) In HS1 and HS2, the flame radius is similar only for the very first image or two. Immediately after the start of ignition, the detected flame radius increases quickly in HS1, then the growth becomes more gradual but remains significant, while in HS2 the flame radius always increases more gradually and in fact with near-zero slope for the first few crank angles aIT. The two example cycles in Figure 45 and Figure 47 suggest that the initial inflation of the flame radius may be due to the spark being carried out of the spark gap more, and the spark is detected as “flame” in all experiments due to its high brightness, but also due to earlier development of an initial flame kernel. (2) On a per-crank-angle basis, the growth of the flame radius (i.e., the integral flame growth rate) is significantly greater in HS1 than in HS2, and (3) in the

former, it even increases towards later crank angles. Since flame speed scales somewhat less than linear with engine speed, part of this difference may be due to the faster speed of the operating point used in HS1 (2000 min^{-1}) vs. HS2 (1500 min^{-1}). However, we would expect the resulting difference to be minor, and conclude that the difference in flame growth rate and the flame acceleration is attributable to differences in the turbulent in-cylinder flow field that drives flame propagation.

5.3.2 Projected burnt area, equivalent flame speed, and correlation with pressure-trace analysis for HS2

This section discusses the connection and correlation between the optical measurements of flame propagation and the pressure trace analysis. Figure 49 shows a scatter plot of the cylinder pressure vs. flame area. Colors designate the data from a particular crank angle. To make the plot easier to read, only every second crank angle (= image) is shown. The corresponding plot for the case of endoscopic *phase-locked* single-shot intensified imaging of OH* chemiluminescence (in the 4-cylinder automotive engine) was shown in [85] (Figure 6). This single-shot method may be a more accurate method of flame-boundary imaging, because the associated detectors are more mature than "high-speed" detectors, but does not allow following a single cycle.

Nevertheless, despite the more challenging conditions, Figure 49 shows the same features as that previously published plot, and with similar clarity: At very early crank angles –in the present case of HS2 until about 18°CA aIT– there are no significant differences in pressure between different cycles, while the endoscopic measurement already shows variations in the burnt area spanning an order of magnitude. Thus, for these early times, the optical measurement is a much better indicator of cyclic variability. For intermediate crank angles (here, 20 to 32°CA aIT) we find the expected positive correlation between pressure and burnt area. For later crank angles this correlation is progressively lost as the flame reaches the edge of the endoscope's FOV, which limits the maximum detectable burnt area to 450 mm^2 in the case of HS2. However, at this phase of the flame propagation, information from the cylinder pressure sensor has become reliable and can be used to assess each cycle's combustion progress – albeit with no spatial information. We thus conclude that also in the case of unintensified broadband high-speed imaging with its single-cycle time resolution, the endoscopic measurement complements the traditional pressure-trace analysis very well.

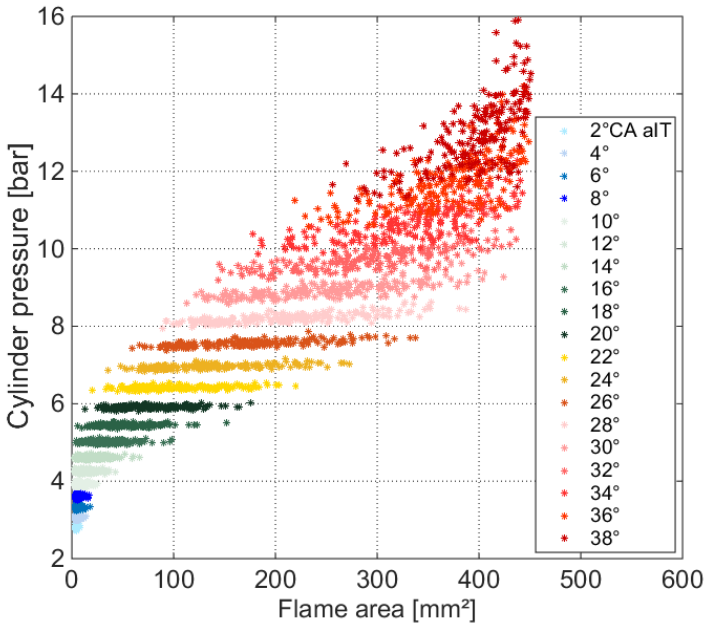

Figure 48: Correlation between cylinder pressures and apparent burnt area in HS2.

From the data shown in Figure 48d, the circumference-averaged projected flame growth rate s_F can be calculated by discrete differentiation in time: $s_F = \Delta r_F/\Delta t$. Taking the derivative acts as a high-pass filter, thus the resulting single-cycle growth rates show large, not necessarily physical variations in time. The results become more meaningful when averaged over many cycles or some number of crank angles. Figure 50 shows the growth rate averaged over all cycles from HS2 as a function of crank angle. The plot is consistent with textbook results (e.g., [126], p.229) clearly showing the first three phases of spark-ignited premixed combustion in engines:

1. Ignition, with near-zero propagation speed
2. Development of the flame kernel, characterised by an acceleration of the flame front due to increasing wrinkling
3. (Turbulent) flame propagation, with a speed that is nearly constant if turbulence is similar throughout the combustion chamber

Except for parts of the pent-roof, the last phase of combustion, wall termination, is not accessible by the present endoscopic imaging. Instead, the seeming decrease in the optically measured average flame speed (to the right of the dashed line in Figure 50 occurs because in more and more cycles the flame has reached the edge of the FOV.

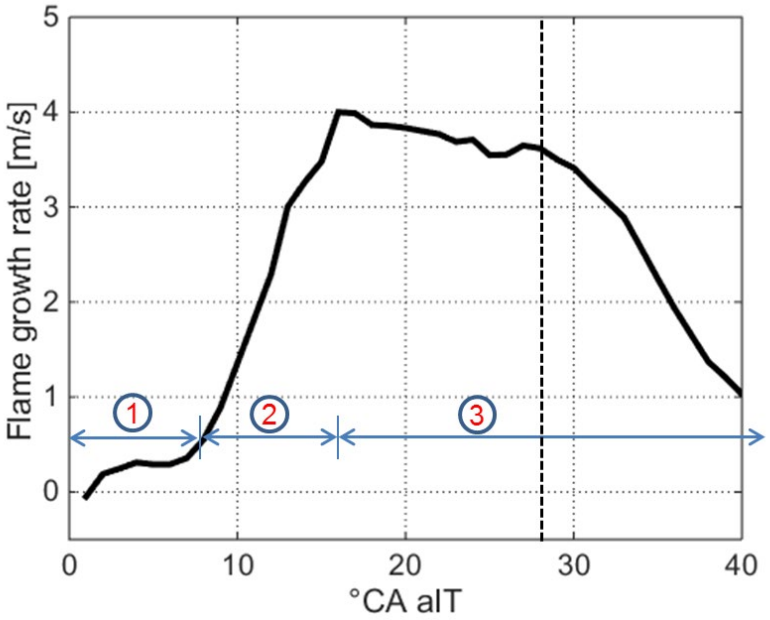

Figure 49: Average flame growth rate of all cycles in HS2 with the first three phases of "classic" SI engine combustion numbered for reference in the text.

In HS2, the multi-cycle average flame growth rate during turbulent flame propagation is between 3.5 and 4 m/s. Comparing this result to the previously documented rate of about 10 m/s in the 4-cylinder automotive engine at the same operating point as in HS1, [85] (Figure 16), quantifies the observation made above, that flame propagation in HS1 appears to be significantly faster than in HS2.

In extensive experiments in a fully optically accessible engine, Aleiferis et al. [47, 48] showed that the flame growth rate optically measured and then averaged on a single-cycle basis over a time interval corresponding to early flame propagation correlates with CA5, the crank angle at which 5% of the fuel mass are burned. This crank angle is typically one of the earliest for which the mass fraction burned (MFB) by the flame can be determined reliably from single-cycle pressure-trace analysis. We therefore examine if this well-established correlation can be recovered from endoscopic high-speed imaging.

Figure 51 shows the pressure-derived MFB in HS2 for the two example cycles (a) and (b) as well as the average over all recorded cycles. As is typical for SI engines, CA5 varies significantly, occurring at -16.5°CA (16.5° before TDC) in cycle (b) and at -8.0°CA in cycle (a). The early flame's growth rate, on the other hand, was calculated by averaging the rate s_F for each single cycle of HS2 from 1 to 28°CA aIT.

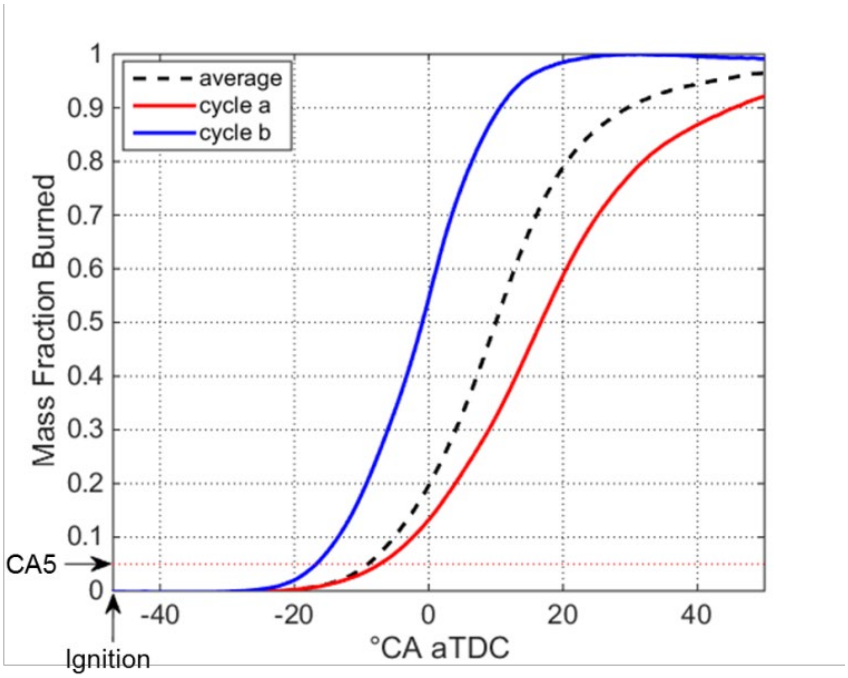

Figure 50: Pressure-derived mass fraction burned (MFB) for the two example cycles in HS2.

Figure 52 is a scatter plot of the pressure-derived CA5 vs. the optically determined flame growth rate s_F. The plot agrees well with the results of Aleiferis [47, 48] and Salazar [20], with "optically slower" cycles indeed systematically reaching CA5 later than faster ones. Least-squares fitting of a linear function to data yields a coefficient of determination $R^2 = 0.62$. Note that in most cases CA5 is reached *after* the "useful" duration of endoscopic imaging, when the flame has reached the FOV, consistent with Figure 49. The analyses of Aleiferis et al. are much more detailed than the present one, and they also show that the correlation obtained by imaging through the piston window of their optical engine results in an even better correlation than the one obtained from side viewing like in the present experiments. Nevertheless, the present endoscopic high-speed imaging is seen to deliver the result expected from the literature quite well.

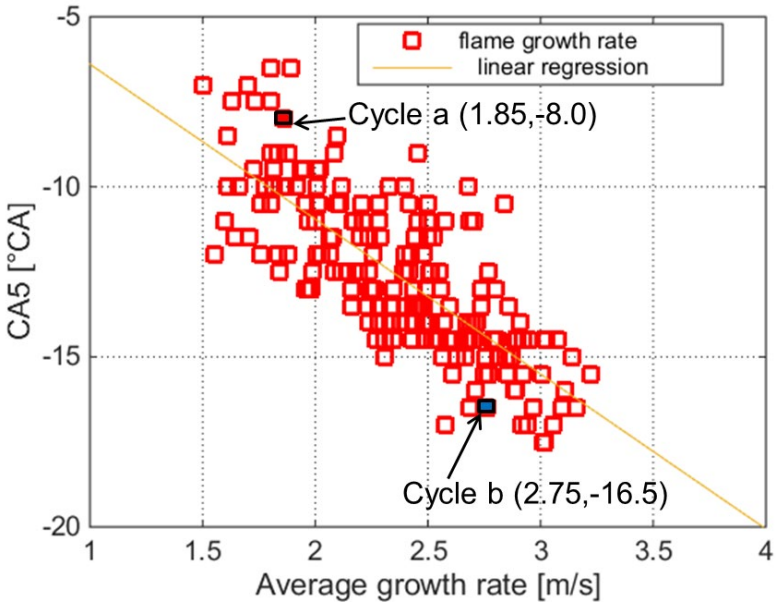

Figure 51: Correlation between CA5 and flame speed for all cycles in HS2.

Chapter 6 Combined endoscopic phase-locked PIV and HS flame propagation imaging

In this chapter, a combined high-speed flame chemiluminescence and phase-locked 2D PIV imaging was conducted to study the relationship between flow field and turbulent flame propagation. The use of a PIV system as the basis for this measurement allowed two successive images to be acquired within a short interval. Mie scattering imaging was used to obtain details of the flame front on the vertical tumble plane that could not be identified by chemiluminescence imaging due to the projected line-of-sight nature of the latter technique. By combining pressure-derived heat release analysis and optical flame speed measurements, the relation between flow field and early flame propagation was observed and correlated. This study was performed by the author and is unpublished at the time of writing.

6.1 Experimental setup

The combined flow-flame measurements were performed in the BMW N46B20 production engine using the same hybrid endoscopic system described before. Phase-locked particle image velocimetry (PIV) was coupled with high-speed unintensified flame chemiluminescence imaging to evaluate the relationship between flow structure and turbulent flame propagation. The schematic diagram of the experimental setup is illustrated in Figure 53. The measurements were carried out at an engine speed of 2000 rpm and a torque of 75 Nm and operated with stoichiometric fuel/air ratio. The trigger signal was generated for every engine cycle at a rate of 16.67 Hz to synchronize the engine, camera, and laser. For PIV seeding, oil droplets (DEHS, LaVision) were generated using a seeding generator (LaVision) and the particles were introduced into the air through the intake manifold, which was supplied to one of the engine cylinders. As shown in Figure 53, the double-pulse 532 nm beam of a Nd:YAG laser with time separation of 10 μs at a repetition rate of 8.333 Hz was sent into the light-sheet endoscope through an articulated arm (LaVision). The laser energy was 25mJ/pulse as measured before the endoscope that generates a 1-mm-thick diverging laser light sheet through a set of

cylindrical optics. The laser sheet then illuminated the region at the mid-plane between two intake valves. A dichroic beam splitter was mounted in between the front endoscope and the relay lens. The transmitted light above 513 nm was directed onto sCMOS camera sensor for Mie scattering detection, while the reflected light below 502 nm was collected by the high-speed CMOS sensor for flame chemiluminescence detection. A band pass filter (532/3) was placed onto the 105 mm f/2.8 micro lens to further constrain the spectral range of Mie scattering to block light from surface reflection.

For 2D flow-field and Mie flame-front imaging, a double-frame sCMOS camera with 6.5 µm pixel size was utilized to record 143 cycles of particle image pairs at two different crank positions, 50°CA and 26°CA bTDC. The image pairs were recorded at a resolution of 2560 x 2160 pixels with a repetition rate of 8.333 Hz (every second engine cycle). This generates images with a projected pixel size of 15.5 µm/pixel. Simultaneously, time-resolved flame propagation images were recorded for every second combustion cycle using a high-speed CMOS camera (VisionResearch Phantom v7.3) with an exposure time of 50 µs. The chemiluminescence imaging started at 50°CA bTDC (= 15.5°CA before ignition) and continued to 6°CA bTDC (= 28.5°CA after ignition). Images that are taken before the spark event are used for background correction. The images were recorded at 608 x 456 pixel resolution at 11 kHz frame rate, resulting in 1.1°CA per frame at 2000 rpm engine speed. The image magnification leads a projected pixel size of 60 µm/pixel.

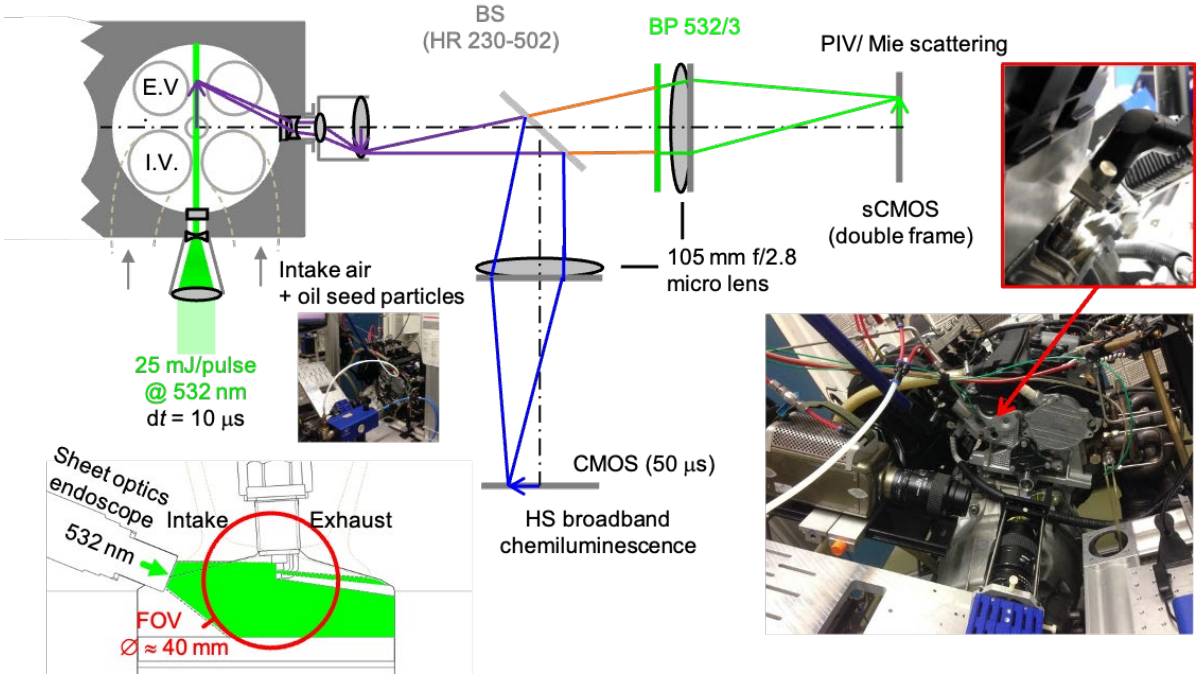

Figure 52: Schematic diagram of combined PIV/Mie scattering and high-speed flame chemiluminescence imaging

Table 11: Engine operating conditions and measurements set up of the all-metal production engine

Phase-locked PIV setup	
Laser	Double-pulse Nd:YAG @532 nm
Pulse time separation	10 µs
Detector	Imager sCMOS double-frame
Imaging lens	105 mm f/2.8 micro lens
Region of interest (ROI)	Full frame at 2560 x 2160 pixels
Imaging frequency	8.333 Hz
Beam splitter	HR 230-502 nm
Bandpass filter (PIV camera)	BP 532 nm (±3 nm)
Tracer seed	DEHS
Scale (after calibration)	64.2 pixel / mm
High-speed chemiluminescence setup	
High-speed camera	VisionResearch Phantom v7.3
Imaging lens	105 mm f/2.8 micro lens
ROI/Frame rate	608 x 456 pixels @11 kHz
Exposure time	50 µs
Projected Pixel Size (PPS)	60.0 µm /pixel
Engine operating conditions	
Speed/torque	2000 rpm/ 75 Nm
Ignition timing	34.5° bTDC
Equivalence ratio	1.0

6.2 Cyclic variations and correlation with pressure-derived heat release

6.2.1 Mie-scattering for flame-front detection vs. high-speed chemiluminescence imaging

In this section, the quality of 2D planar flame-front images from Mie scatter imaging was examined with a large-aperture endoscope system. In the present work, the detected planar flame-front from the phase-locked Mie scattering imaging was compared with chemiluminescence from high-speed imaging at the same crank angle position in the same combustion cycle.

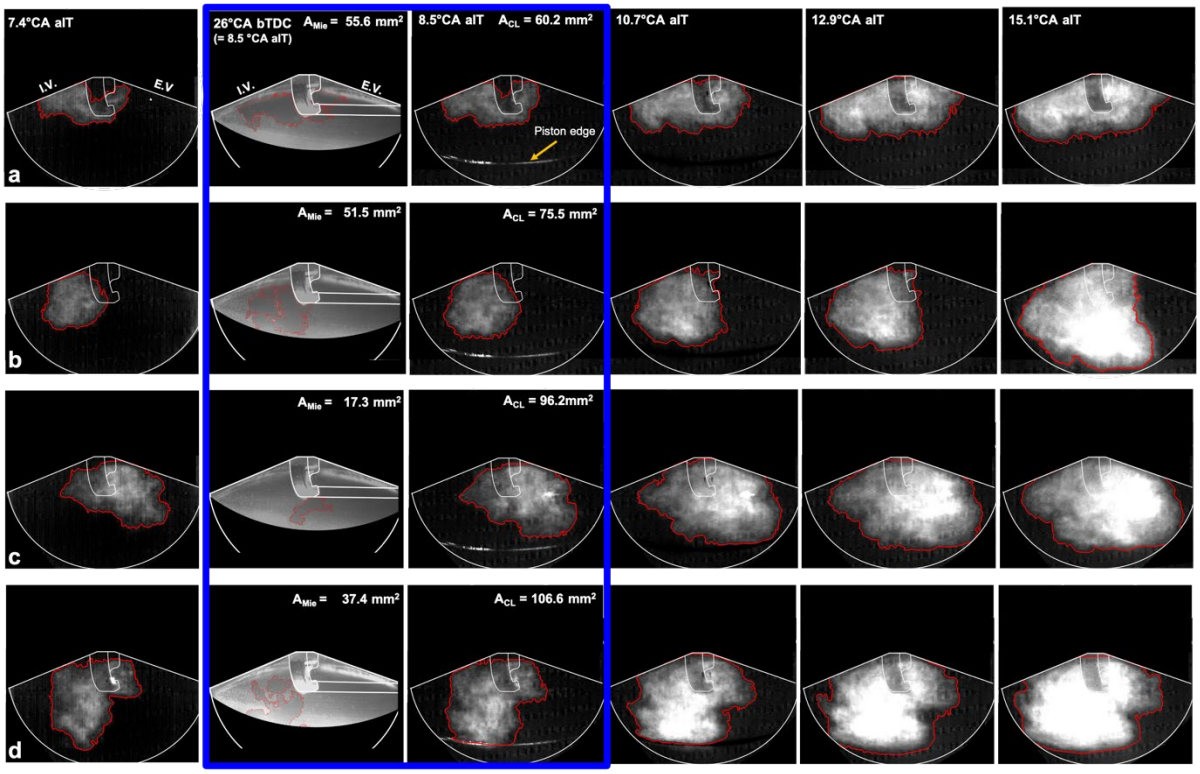

Figure 53: Flame front from Mie scattering for 4 different cycles (a-d) and the corresponding high-speed flame chemiluminescence detection from the same cycles. The two images in the blue box in each row represents an image pair of Mie-CL burnt area at the same crank angle. The red line indicates the detected flame boundary, the corresponding burnt area is placed in the upper right-hand corner of some selected images

The Mie scattering images were captured at 26°CA bTDC (equivalent to 8.5°CA aIT) using double-frame imaging at 8.333 Hz (every second combustion cycle), while time-resolved chemiluminescence images were recorded using the high-speed camera at 11 kHz, equivalent to 1.1°CA per image. Figure

54 shows a sample of flame front measurements from Mie scattering and the corresponding high-speed chemiluminescence from the same combustion cycle for some selected cycles. Images obtained using Mie scattering are noisier than corresponding chemiluminescence images, as they consist of discontinuities associated with the mean spacing between droplets. The instantaneous flame front was identified as droplets evaporate through the flame front, changing the particle number density between burnt and unburnt region. The local wrinkled flame structure due to the presence of turbulence in the unburnt gas region is clearly seen from the Mie scattering images. Based on the CL images, the flame propagates while preserving its shape throughout the engine cylinder. However, the shape, location, and size of the burnt area vary from cycle to cycle. The boundaries of the flame are well-defined by this broadband high-speed endoscopic imaging.

In order to obtain quantitative results, both Mie and chemiluminescence images were post-processed in MATLAB. First, the region of interest ROI was defined to mask out the region with strong reflected light. The average background of all input images was calculated and subtracted from each raw Mie scattering image. This background subtraction process has effectively suppressed uneven illumination in the raw images. The background corrected images were then smoothed in both spatial (median filter with 3 x 3 pixels size) and frequency (Wiener filter with 7 x 7 pixels kernel) domains to reduce the noise in the images. These pre-processing steps were executed directly in PIVlab. Finally, the boundaries of the flame front were extracted in MATLAB using Otsu's thresholding method and binary morphological processes. The detected edges were enhanced using a series of erosion-dilation steps dependent on each image. As for the chemiluminescence images, flame boundaries and quantitative results such as the projected burnt area (PBA), and flame growth rate were extracted from 143 combustion cycles using the Predictor Corrector (PC) algorithm described in Chapter 4. Based on the quantitative results extracted from chemiluminescence images, the connection and correlation between thermodynamics (cylinder pressure) and the optical measurements of flame propagation (projected burnt area) was established. Figure 55a shows a scatter plot of the cylinder pressure vs. the projected flame area at different °CA aIT for 71 different combustion cycles. The corresponding plot for the same endoscopic imaging technique in the single-cylinder motorcycle engine was shown in [14] (Figure 49). Both plots show the same characteristics: At a very early combustion stage, between 2 to 6°CA aIT, there are no significant cyclic variations in terms of cylinder pressure. However, the optical measurement shows variations in burnt area, and thus can be a much better indicator of cyclic variability. For intermediate crank angles (8-16°CA aIT), both cylinder pressure and burnt area have positive, and linear correlation, as can be seen in Figure 55b. For late crank angles, this correlation starts to degrade significantly as the flame reaches the endoscope's FOV. At this combustion stage,

the thermodynamics analysis from the pressure sensor becomes more reliable to assess single cycle combustion progress.

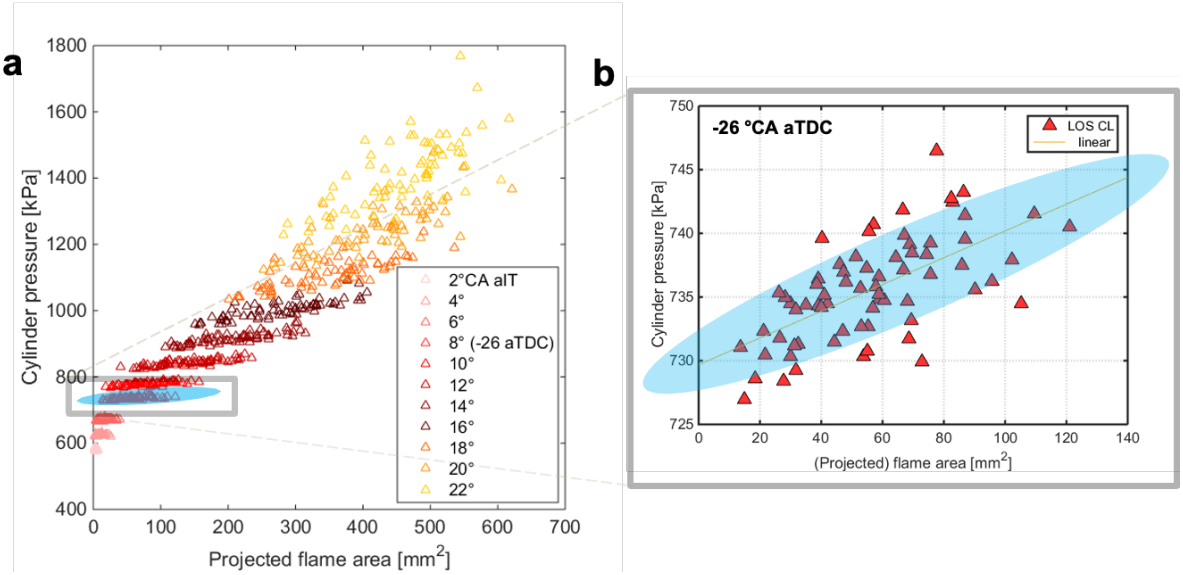

Figure 54: (a) Scatter plot of in-cylinder pressure vs. projected burned area at different °CA aIT; (b) Correlation between cylinder pressure and projected burnt area at -26 °CA aTDC (= 8°CA aIT)

The two images in the blue box, each row in Figure 54 represents an image pair of Mie-CL burnt area at 26°CA bTDC (= 8.5°CA aIT) from 4 different combustion cycles. Some cycles show a good correlation between Mie and CL images in terms of flame shape and position of the burnt area, as can be seen in Figure 54a-b. However, some cycles show the opposite results, in which the Mie burnt area is much smaller compared to CL projected burnt area, as shown in Figure 54c-d. The CL images yield larger burnt areas than the corresponding Mie images because they represent a line-of-sight projection of the outermost burned region.

Since the laser sheet illuminates the same region of interest for both imaging techniques, a direct comparison can be made in terms of detected burnt area from these two imaging techniques. Figure 56a shows a scatter plot of projected burnt area as measured by broadband CL (A_{CL}) vs. burnt area measured by Mie scattering (A_{Mie}). As expected, all image pairs have the area ratio, A_{CL}/ A_{Mie} greater than 1 (all the points lie above the line $A_{CL}/ A_{Mie} = 1$).

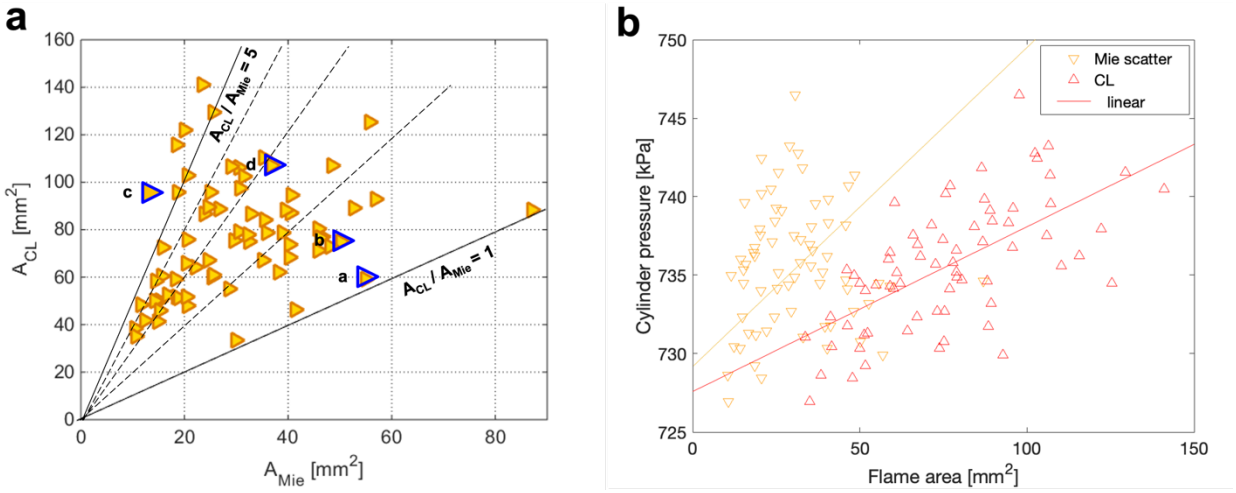

Figure 55: (a) Scatter plot of A_{CL} vs. A_{Mie}. Letters (a-d) correspond to the image pairs in the blue box in Figure 54; (b) Pressure vs. flame area, the latter determined by two different metrics

The image pairs in the blue box shown in Figure 54 are labelled with corresponding letters (a-d) in Figure 56a. Cycle (a) and (b) have a low area ratio, which means the shape of the burnt areas are similar in the CL and Mie images. However, cycle (c) and (d) have a high area ratio, in which the Mie burnt area is much smaller than the CL projected burnt area. This may be due to the variation of the flame position in the optical axis. Cyclic variation in flow structure, specifically the presence of large-scale vortexes within the engine cylinder, can have an impact on the spatial movement of the flame in all directions. Consequently, this variation in flame position, especially along the optical axis, can affect the image size captured by a front endoscope with wide viewing angle. The previous endoscopic work conducted by Goschütz et al. [95] concluded that image pairs of anisole LIF and OH* CL with high area ratio indicate that the flame preferentially burned towards the endoscope. Figure 56b plots the cylinder pressure at the time of image acquisition vs. flame area determined from CL and Mie images. The plot clearly shows that the burnt areas from CL images have better correlation with in-cylinder pressure compared to the burnt area derived from Mie images. These findings are consistent with the results obtained by Shahbaz et al. [78], which also reported that the burnt area derived from OH* CL images (full FOV) correlate better with in-cylinder pressure compared to the burnt area obtained from LIF images. This is consistent with the character of line-of-sight integration, which allows for the construction of two-dimensional representations of the observed volume. On the other hand, 2D planar Mie images as shown in Figure 54, provide the details of the flame front wrinkles, even in this challenging endoscopic application.

6.2.2 Correlation between flame propagation speed and pressure-derived mass burn function

Based on the correlation plot of pressure and flame area in Figure 56b, we conclude that line-of-sight imaging provided a better two-dimensional representation of gas-burnt volume. In our previous work [14], we found a strong correlation between pressure-derived CA5 and optically measured average flame speed through endoscopic high-speed chemiluminescence imaging in a single-cylinder direct injection (DI) motorcycle engine. In the present work, we re-examine the correlation between optical data of flame propagation speed with the corresponding pressure-trace analysis in an all-metal 4-cylinder PFI engine. The engine was operated at 2030 rpm and 75 Nm of torque with stoichiometric conditions. At this operating condition, the ignition timing was set at 34.5°CA bTDC.

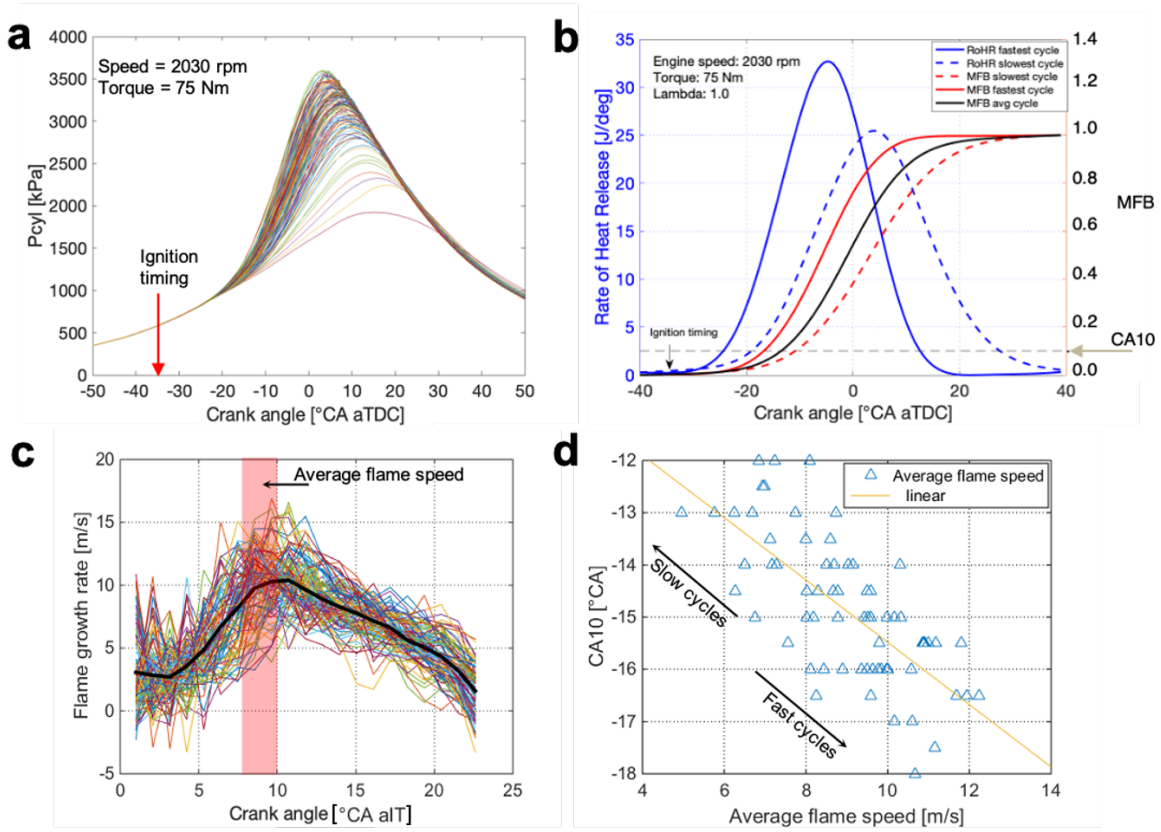

Figure 56: (a) In-cylinder pressure vs. °CA aTDC; (b) Pressure-derived heat release and MFB; (c) Optical flame speed over °CA aIT (every second combustion cycles); (d) Correlation between CA10 and average flame speed

Figure 57a shows the recorded in-cylinder pressure as a function of crank angle for 143 consecutive combustion cycles. There is no significant variation in pressure between individual cycles within the first 10°CA after ignition timing. However, the variations in cylinder pressure become significant for the later crank angle, occurring from 20°CA bTDC to 30°CA aTDC. Cylinder pressure traces clearly show the variations in peak pressure, rate of pressure rise, and the shape of the pressure curve, which are indicative of cyclic variability. The heat release analysis was computed based on a single-zone zero-dimensional model [127]. The corresponding pressure-derived HRR and MFB for the two selected cycles, as well as the average over all recorded cycles are shown in Figure 57b. The two selected cycles are the fastest and the slowest cycle recorded in this dataset. The crank angle at 10% of mass fraction burned, CA10 varies significantly from cycle-to-cycle, occurring at 18°CA bTDC in the fastest cycle and at 12°CA bTDC in the slowest cycle.

The average flame speed was computed by averaging the flame's growth rate, s_F for each individual cycle from 8 to 10°CA after ignition timing (aIT). Figure 57c shows the optically measured flame speed of all cycles as a function of crank angle. The multi-cycle average flame speed during turbulent flame propagation is about 10 m/s, consistent with the result obtained in Ref.[85] for the same engine operating condition. A scatterplot of the average flame speed versus CA10 is shown in Figure 57d. Linear least squares fit to data yields a correlation coefficient of 0.68, indicating a strong correlation between optical flame speed and CA10. This means that 'faster' cycles reach CA10 earlier than the 'slower' ones. Therefore, the cycles can be classified as 'slow' or 'fast' based on their CA10. In order to investigate the relation between turbulent flame propagation and flow field, the cycles were divided into 35 fastest ('fast') and 35 slowest ('slow') cycles. The flow field of the corresponding cycles were analysed, and the influence of flow field on turbulent flame propagation was investigated and correlated.

6.3 Relationship between in-cylinder flow field and turbulent flame propagation

6.3.1 Flow-field vector calculation in PIVlab

The PIV vectors were computed with PIVlab v2.61, a Matlab-based open-source software developed by Thielicke [103, 104]. The raw PIV images first undergone the optical distortion correction in DaVis (LaVision, Göttingen, Germany). The pre- and post-processing procedures in PIVlab are shown in Figure 58.

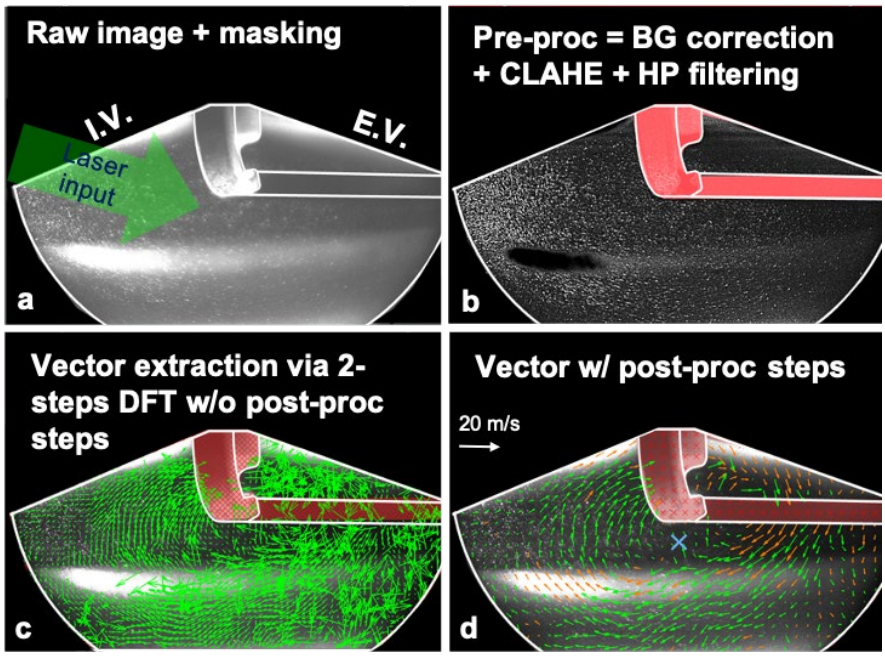

Figure 57: Vector extraction procedure in PIVlab: (a) Applying mask for ROI, (b) Pre-processing, (c) Raw vector computation via a 2-step discrete Fourier Transform (DFT), (d) Interpolated vectors (orange) in post-processing. The blue x marker indicates the visually determined center of the tumble vortex. Every second vector is shown in (d)

The region of interest (ROI) is defined to mask out the regions with no signal and to exclude the undesired light reflection on the spark plug and pent-roof surfaces (Figure 58a). In pre-processing, low-frequency background information due to inhomogeneous illumination was suppressed by applying a high-pass filter. However, the regions with constant intensity in the raw image are zero as a result of derivative in the spatial domain, as can be seen in Figure 58b. Consequently, useful vector fields could not be computed in these regions. Also, the background correction was performed by subtracting the average intensity of 100 images from each raw image. Then, the built-in function in

PIVlab, contrast limited adaptive histogram equalisation (CLAHE) was applied to enhance the local pixel intensity (30 x 30 pixels), effectively increased the contrast of the particle images for better correlation. This function spread out the most frequent intensities of the image intensity histogram throughout the full data range, optimizing the regions with low and high exposure independently. A sample of a pre-processed image is shown in Figure 58b. For vector calculation, a multi-pass discrete Fourier transform (DFT) window-deformation cross-correlation with interrogation areas decreasing from 64 x 64 to 32 x 32 pixels with 50% overlap was applied. This computes the correlation of the particle displacement at every pixel within the defined interrogation window, thus resulting in a vector spacing of 640 µm. A 3-point Gaussian sub-pixel peak finding algorithm was used to obtain the most probable droplet displacement within the selected interrogation window size. A sample of a computed raw vector field is shown in Figure 58c. In the final step, the raw vectors were post-processed to identify and remove spurious vectors. This was done by evaluating velocity thresholds semi-automatically based on mean and standard deviation of velocity. Each velocity component was compared with a lower threshold and an upper threshold, and the velocities that are not in between these thresholds were removed. The missing vectors were then replaced with the interpolated vectors (orange), as shown in Figure 58d.

6.3.2 Cycle-to-cycle variations of the in-cylinder flow-field

The flow measurements were performed within the center of tumble plane (at the mid-plane between two intake valves) during the compression stroke at 50°CA bTDC. Figure 59 shows the instantaneous flow field of some selected individual cycles and the ensemble-averaged over 35 cycles for ‘fast’ and ‘slow’ cycles. The instantaneous velocity fields of all 8 individual cycles reveals significant cyclic variation in flow structure. Nevertheless, at this crank position, all cycles have flow motion towards the exhaust side with different location of the tumble vortex center. These variations are due to the complex interaction between the bulk tumble motion and the piston-induced upward flow, which creates shear and breaks up large-scale tumble into micro-scale turbulent eddies, particularly during the late stages of the compression stroke [56, 67, 96, 128]. Based on the mean velocity fields, the fast cycle has a higher mean flow velocity in the vicinity of the spark plug as compared to the slow cycle. This finding is consistent with the results obtained through high-speed PIV measurements in optically accessible research engines [7, 56, 96], which reported that the flow direction and the velocity components near the spark region influence the overall flame propagation speed. Another remarkable notice is that the fast-burning cycles have a single large-scale tumbling vortex, which effectively carries the kinetic energy to maintain higher mean flow velocity in the vicinity of spark plug before

the time of spark discharge. On the other hand, slow cycles have a small-scale tumble structure with two or more counter-flow vortices, as seen in cycle #56 and cycle #77. This is due to the large-scale tumble flow breaking up earlier into small vortices during the compression stroke, as a result of vortex-wall interactions [128], consequently leading to weakened tumble motion that cannot maintain a strong flow motion near the spark plug. In fast cycles, the tumble motion moves around within the center and lower part of the spark plug location, which is in agreement with the findings in Ref.[96] through high-speed PIV measurements. On the other hand, in slow cycles, the center of the tumble flow moves towards the intake valve side.

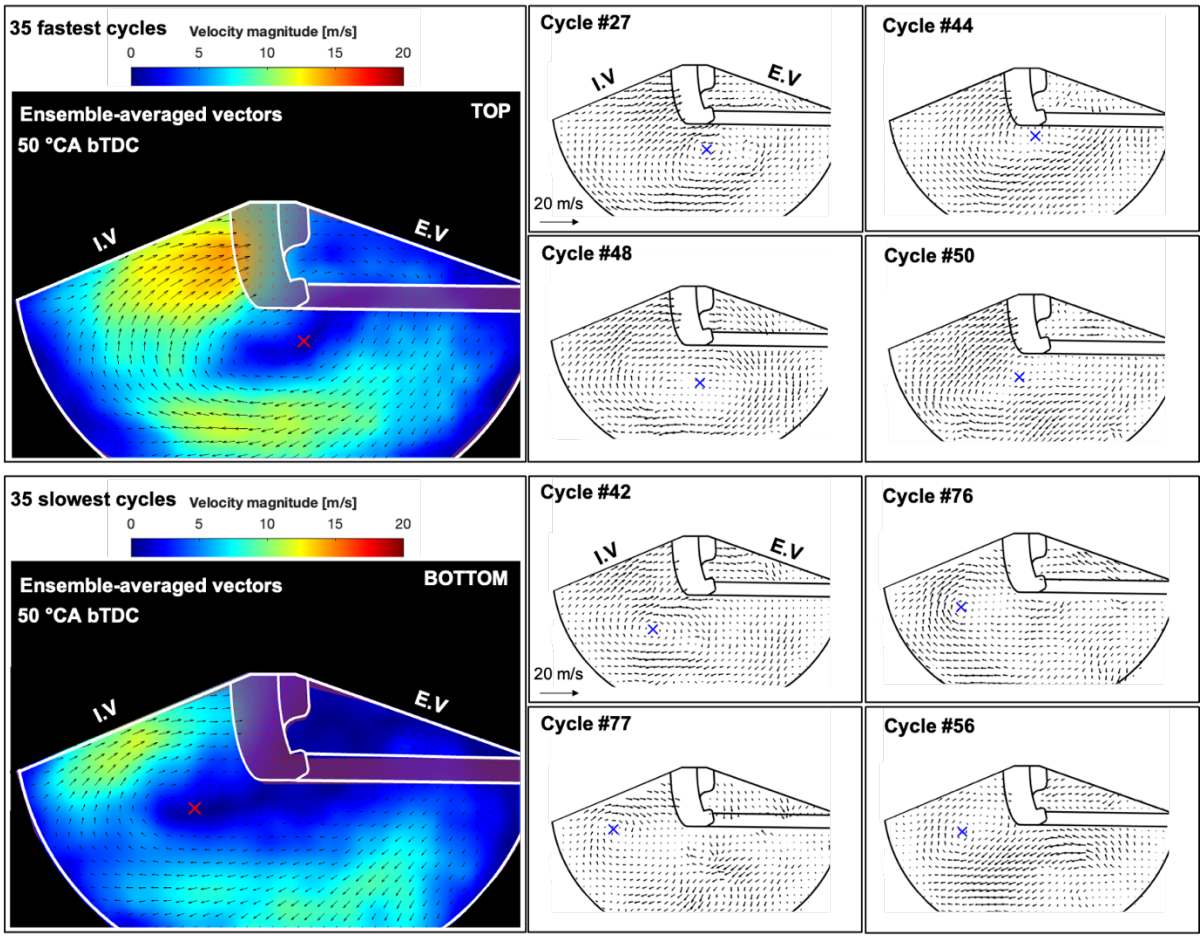

Figure 58: Instantaneous flow field of 4 different individual cycles (right) and the ensemble-averaged flow field of the 35 fastest (top) and slowest (bottom) cycles (based on CA10). The red and blue x marker indicate the visually determined center of the tumble vortex

6.3.3 Impact of flow structure on spark arc and turbulent flame propagation

The in-cylinder flow measurements are combined with high-speed flame chemiluminescence imaging to investigate the influence of flow structure on the spark plasma and the turbulent flame speed.

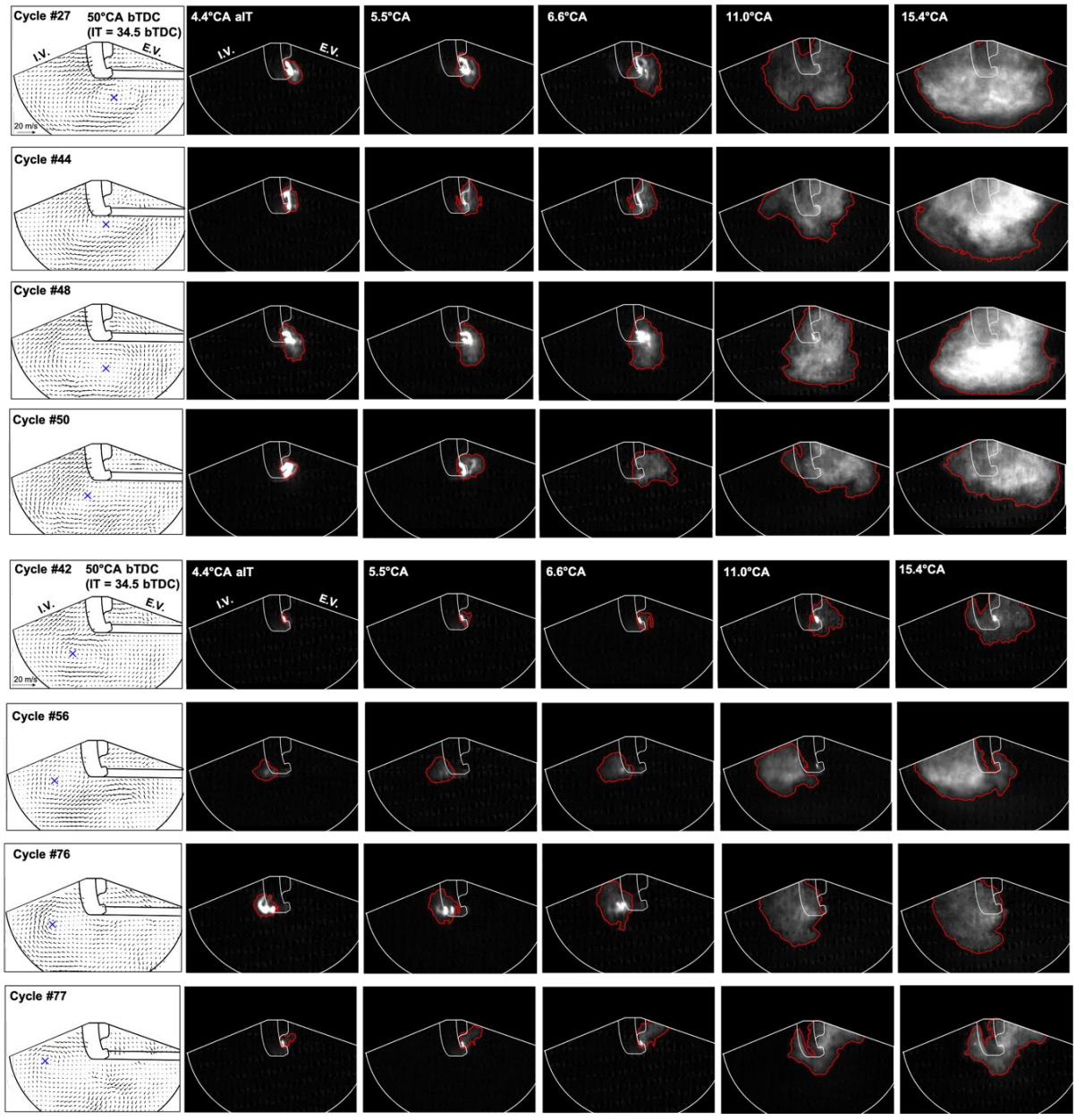

Figure 59: Flow velocity vectors and the corresponding time-resolved flame propagation of some selected individual cycles. Top: 35 fastest cycles; Bottom: 35 slowest cycles

Figure 60 shows the corresponding flame propagation images from the same cycle of flow measurements. The flow-flame images unveil the influence of the flow direction and velocity components near the spark region on the direction and stretch of the spark plasma. These factors in turn determine the overall speed of turbulent flame propagation. The fast-burning cycles, characterized by higher mean flow velocity in the spark vicinity, predominantly exhibit a spark arc movement towards the exhaust side. This observation aligns with the findings of [56], which reported that only 4-8% of cycles showed a spark arc stretching towards the intake side in the high-tumble case.

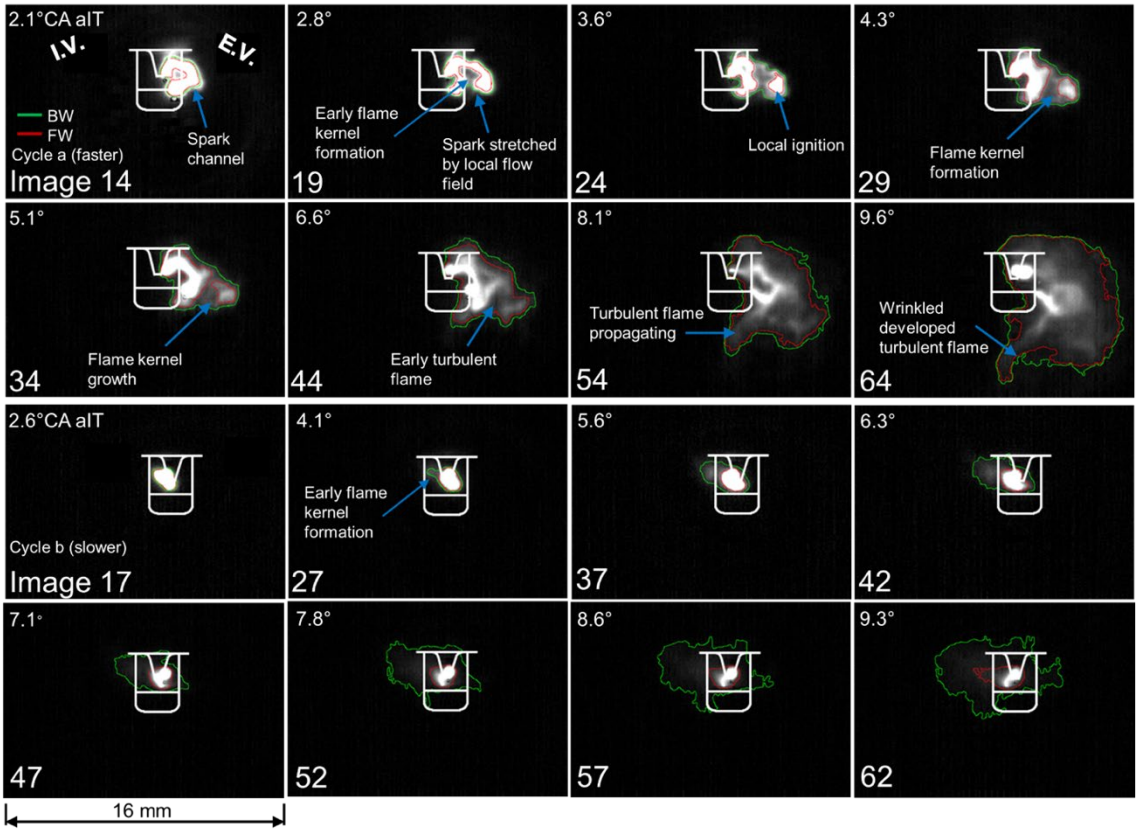

Figure 60: Spark arc imaging at 75 kHz: (a) faster cycle, (b) slower cycle. Image 0 corresponds to ignition timing. The red and green lines indicate the flame boundary as detected by in-house 'Predictor-Corrector' scheme via backward (BW) and forward (FW) sequences [14]

This finding is further supported by the visualization of the spark plasma and the initial kernel formation at 75 kHz, conducted under the same engine operating conditions in our previous work (Figure 61). The spark arc stretches due to the influence of the local flow field, effectively transferring the local ignition to the adjacent unburned mixture during the first 5°CA aIT. This process leads to the acceleration of the early flame kernel, which eventually transitions into a turbulent flame with a higher growth rate. In comparison to the slower cycles, low mean flow velocity in the spark vicinity

causes the spark plasma to remain grounded during the first few °CA after ignition timing (cycle #42 and cycle #77), resulting in the loss of heat to the spark ground instead of convecting that thermal energy to the adjacent unburned mixture. Consequently, a longer time is required for the flame to spread throughout the combustion chamber. Another remarkable observation is that the slow-burning cycles exhibit a spark arc convecting towards the intake side. One possible explanation is the adverse pressure gradient induced by the vortex motion (vortex-wall interaction), resulting in flow separation, which can be observed in cycles 56 and 76. This phenomenon leads to a shift in flow direction near the spark, pointing towards the intake side counter to the small-scale tumble motion.

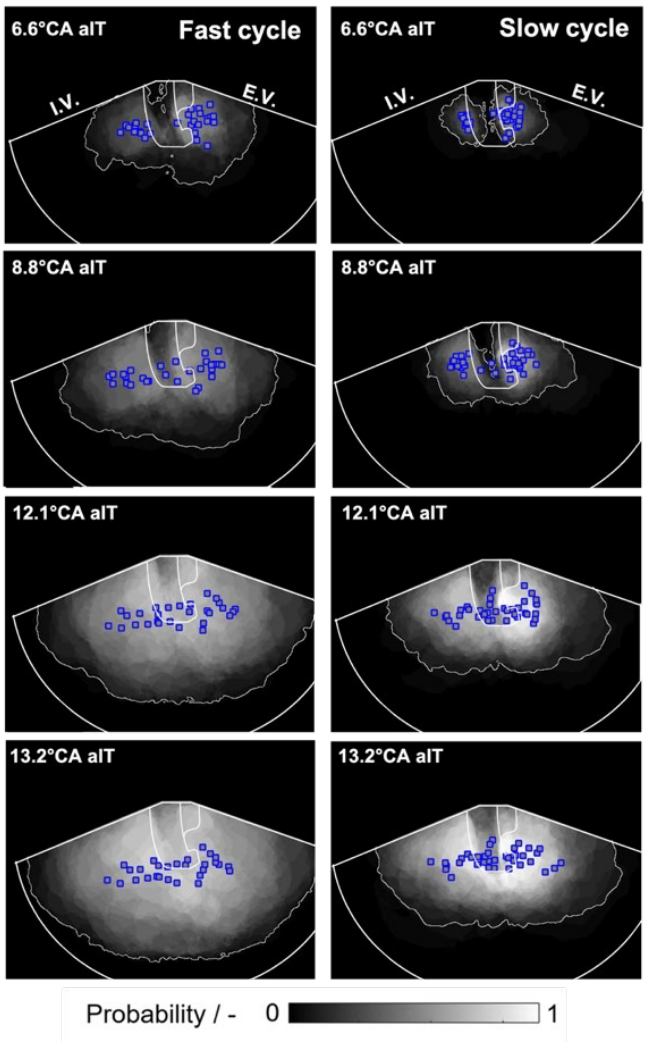

Figure 61: Burnt area probability contours at different °CA aIT for the 35 fastest ‘fast’ and 35 slowest ‘slow’ cycles. The blue marks indicate the centroid location of each cycle’s burnt area. The white line represents that at least one cycle has a burnt area within the outline

Figure 62 provides a more comprehensive analysis on spatial and temporal characteristics of the flame propagation. The flame probability contours at different °CA aIT is shown as mean over the 35 fastest and 35 slowest cycles. The figure also shows the centroid location of the flame in each cycle at the specified crank angle position. The white line represents that at least one cycle has a burnt area within the outline. Clearly, the fast-burning cycles consistently exhibit faster early flame kernel growth and subsequent turbulent flame propagation compared to the slower cycles. In fast cycles, the flame centroid spreads randomly, scattering more around the spark plug, especially during the initial 9°CA aIT. Conversely, in slow cycles, the distribution of the flame centroid is more concentrated around the spark vicinity. Nevertheless, as the combustion progresses to the later crank angles, the flame shape and the centroid location become almost identical for both cases, despite the flame probability contour being larger for the fast cycles than for the slow cycles. This suggests that in fast burning cycles, the flame mostly tends to preferentially burn towards the endoscope, as evidenced between 12.1° to 13.2°CA aIT in Figure 62. At this crank angle, the entire spark plug's ground electrode appears behind the CL signal, presumably within the burnt gas region. Therefore, in fast burning cycles, the flame might also travel in the direction of the optical axis, influenced by three-dimensional flame-flow interactions.

To identify correlation regions between the average flame speed s_F (from 8°- 10° CA aIT) and velocity magnitude $|v|$ in the two-dimensional flow-field, we generated a correlation map following the suggestion of Stiehl et al. [129]. The correlation coefficient, $P_{x,y}$ is defined as:

$$P_{x,y} = \frac{\sigma_{xy}}{\sigma_x \sigma_y} = \frac{\sum_{i=1}^{n}(x_i - \overline{x})\,(y_i - \overline{y})}{\sqrt{\sum_{i=1}^{n}(x_i - \overline{x})^2 \sum_{i=1}^{n}(y_i - \overline{y})^2}} \tag{6.1}$$

σ_{xy} : Covariance of variable x (average flame speed s_F) and variable y (velocity magnitude $|v|$)

σ_x , σ_y : Standard deviation of x and y

The correlation coefficients are used to measure the strength of the correlation between the two variables, either a positive ($1 > P_{x,y} > 0$) or a negative relationship ($-1 < P_{x,y} < 0$).

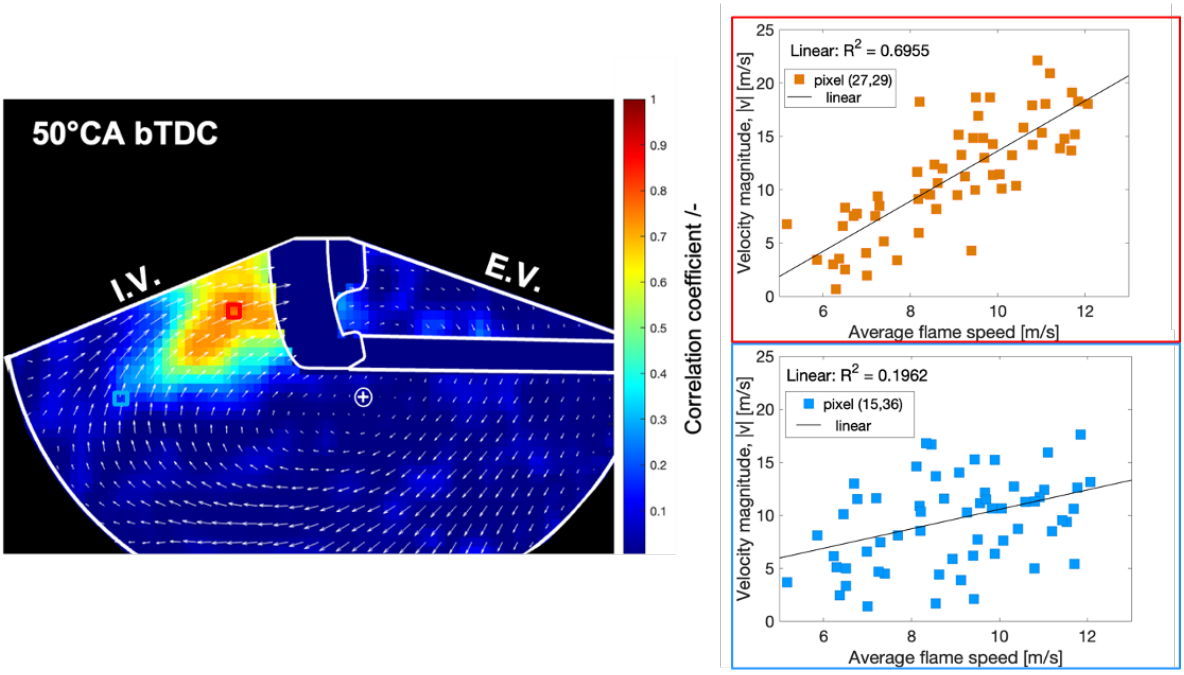

Figure 62: Correlation map of the velocity magnitude $|v|$ with the average flame speed (8°- 10° CA aIT)

The correlation map as shown in Figure 63 links the flow structure at 50°CA bTDC with the subsequent early flame growth. The figure also shows the correlation plot of the velocity magnitude $|v|$ with the average flame propagation speed s_F at two different pixel coordinates. A positive and strong correlation region near the spark plug can be seen in the map, indicating that the flow direction and velocity components have a strong influence on the overall turbulent flame speed. This means that the cycle with a higher mean flow velocity in the spark vicinity experiences faster flame growth. This high-correlation region is where the largest differences in flow velocity magnitude between slow

and fast cycles are found in Figure 59. This finding is consistent with the result obtained in an optical engine [96].

Chapter 7 Conclusions and outlook

7.1 Conclusions

A predictor-corrector image segmentation scheme (PC) was developed and applied to endoscopic high-speed sequences of flame propagation. The algorithm with automatic dynamic thresholding was capable of detecting the line-of-sight projected flame boundary despite artifacts caused by the spark and the large dynamic range in image brightness across each time series. The algorithm performed significantly better than Otsu's method throughout the data set. This advantage was attributed to the fact that the PC procedure makes use of the time-correlated character of the images, enhancing the algorithm's understanding of the data, and therefore maintain accuracy consistently across frames. Furthermore, the algorithm performed quite well even though pattern noise generated by the high-speed camera was very obvious in the background-corrected images. Filtering in the Fourier domain was effective in suppressing this noise component to acceptable levels. Thus, a FFT filtering process increases the robustness of the algorithm for detecting the flame boundary, especially at low-light conditions. This algorithm was also capable of processing images in two ways, forward (FW) and backward (BW) sequences. In the FW mode, the algorithm isolates a region of high intensity, i.e., the spark. On the other hand, in BW mode, the algorithm 'locks' onto the lower-intensity foreground class, i.e., the early flame kernel. Thus, when both FW and BW mode were utilized, the algorithm finds two threshold values for a given image and segments the image into certain brightness regions, which correspond to the bright spark, weak flame kernel, and background. The robustness of the algorithm was systematically evaluated by processing data sets from different engine operating conditions as well as at different levels of lens collection efficiency (F-number) for the same engine operating condition. By implementing this image analysis tool, the quantitative spatial information of flame propagation, such as flame area, speed, and centroid was extracted from high-speed endoscopic image sequences in a fast, robust, and reliable way.

Early flame-front propagation was investigated with a large-aperture UV endoscope in two nearly unmodified production SI engines. Also, in one of the engines two different imaging configurations were tested. The endoscopic results were compared with unintensified high-speed cinematography

with a large-aperture camera lens in an engine with full optical access. The projected burnt area and some associated simple metrics were derived by morphological post- processing. Experiments with unintensified broadband endoscopic imaging in a production single-cylinder motorcycle engine, were analysed further with a pressure-derived heat release analysis and discussed with reference to the literature and previous results from other imaging experiments in one of the engines. Overall, the results show that at the part-load stoichiometric operating points considered here, endoscopic detection of the premixed flame's projected boundary during early combustion is reliably possible, though still significantly more challenging than the same task in a research engine with full optical access. In endoscopic imaging with its limited aperture (equivalent to F/4.5), intensified imaging of OH* has advantages and disadvantages compared to broadband detection in the visible with the unintensified CMOS sensor. In the former case, spatial "smearing" of the intensifier is a problem during the extremely bright spark event that blinds the detector in the vicinity of the spark. This degradation of the spatial resolution also appears later in the cycle, when the flame is imaged. However, the overall shape of the burnt area was still discernible, and the amplified signal level avoids issues with the patterned read-out noise incurred in the case of unintensified imaging. This variant utilizes less specialized hardware and, because of the much larger dynamic range without the intensifier can visualize both spark and ensuing flame, thus providing complementary information on flame-kernel initialization. Unfortunately, current high-speed CMOS cameras are not sensitive in the UV, where OH* chemiluminescence provides a strong and spatially well-defined signal. However, even with that limitation, the large-aperture endoscope made the use of high-speed imaging feasible for the current task. The read-out noise pattern limits low-light performance. This may be overcome with hardware improvement (progress is rapid in the area of CMOS image sensors, and the Phantom v7.3 used here is 14 years old at the time of writing) and with more sophisticated post-processing, for example filtering in the Fourier-transformed time and space domains.

Combined endoscopic phase-locked PIV and high-speed flame chemiluminescence imaging was applied in the production engine to study the relationship between flow structure and turbulent flame propagation. The cyclic variability in flow and combustion were also investigated through Mie-scattering imaging, flame chemiluminescence imaging, and in-cylinder pressure trace analysis. The flame front was detected at 26°CA bTDC using the Mie scattering images of DEHS droplets. The 2D flame-front was compared with the line-of-sight projected burnt area derived from chemiluminescence imaging. Qualitatively, the details of the spark are discernible and the edge of turbulent flame propagation was clearly detected by endoscopic high-speed broadband chemiluminescence imaging. The flame propagates while preserving its shape throughout the engine cylinder. However, the shape, location, and size of burnt area vary from cycle-to-cycle. On the other

hand, Mie scattering imaging resolves the details of flame front wrinkles much better in 2D planar. Quantitatively, the CL images yield larger burnt areas than corresponding Mie images because they represent a line-of-sight projection of the outermost burnt region. The burnt area derived from CL images correlated better with in-cylinder pressure. The ratio between CL and Mie burnt areas indicates variations in the flame position along the optical axis due to cyclic variations in large-scale flow structures that affect the flame's spatial movement in all directions. Based on strong correlation between optically measured flame speed and pressure-derived CA10, the cycles were divided into 35 fastest (‘fast’) and 35 slowest (‘slow’) cycles based on their CA10.

Flow measurements were conducted at the center of the tumble plane at 50°CA bTDC (before top dead center). Ensemble-averaging data from 35 cycles for both 'fast' and 'slow' cycles revealed a consistent flow pattern. In 'fast' cycles, the tumble motion predominantly remained in the central and lower regions near the spark plug location, while in 'slow' cycles, the central tumble flow shifted towards the intake valve side. Notably, 'fast' cycles exhibited higher mean flow velocities near the spark plug compared to 'slow' cycles. Analysis of instantaneous velocity fields from individual cycles unveiled substantial cyclic variations in flow structure. 'Fast-burning' cycles featured a single large-scale tumbling vortex that effectively carried kinetic energy, resulting in higher mean flow velocities near the spark plug before ignition timing. Conversely, 'slow' cycles displayed small-scale tumble structures with two or more counter-flow vortices, induced by vortex-wall interactions, consequently leading to weakened tumbling motion within the cylinder. In all cycles, flow motion was directed towards the exhaust side, albeit with varying positions of the tumble vortex center.

The impact of the flow field structure on spark and turbulent flame propagation was investigated using combined high-speed flame chemiluminescence and phase-locked PIV imaging. Combined flow-flame images revealed that the flow direction and velocity components near the spark region influenced the direction and extension of the spark plasma. In 'fast-burning' cycle, characterized by higher mean flow velocities near the spark, the spark arc stretched away from the ground electrode towards the exhaust side. This mechanism increased the ignition volume and effectively transferred local ignition to adjacent unburnt mixtures, enhancing early flame kernel formation and turbulent growth rates. In 'slow-burning' cycles, the spark plasma remained grounded during the initial few degrees CA (crank angle) after ignition timing, leading to more heat loss through conduction to the spark ground, rather than convective transfer to adjacent unburned mixtures. The spatial and temporal characteristics of flame propagation were analysed by finding the mean probability distribution of the flame contour during the early combustion stage. As anticipated, in 'fast' cycles, the flame centroid exhibited a more scattered and random distribution, with a tendency to disperse further from the spark

plug. Conversely, in 'slow' cycles, the flame centroids were more evenly distributed and concentrated in the vicinity of the spark.

The correlation between the two-dimensional flow velocity magnitude and the average flame speed (within the range of 8° to 10° CA aIT) was analysed. The analysis revealed a strong and positive correlation between the velocity magnitude and the average flame speed, particularly in the vicinity of the spark plug. This finding suggests that flow direction and velocity components significantly impact the overall turbulent flame speed. Notably, the regions with high correlations correspond to areas where the largest differences in flow magnitude between 'slow' and 'fast' cycles are observed.

7.2 Outlook

The accuracy of PIV measurement can be further enhanced by utilizing seed particles with high thermal resistance to prevent the evaporation of seeding particles at high temperatures, thus maintaining a suitable particle density for both flow field measurements and the flame front detection.

For future research, a more challenging endoscopic measurement can be carried out by integrating various optical diagnostic techniques, such as high-speed PIV, laser-induced fluorescence (LIF), and chemiluminescence imaging to provide deeper insight into cyclic variability in flow fields, mixture formation, and combustion processes in a production engine.

References

[1] Average CO_2 emissions from new passenger cars and future targets, European Environment Agency. https://www.eea.europa.eu/data-and-maps/daviz/average-co2-emissions-from-new#tab-chart_1

[2] R. D. Reitz, H. Ogawa, R. Payri, T. Fansler, S. Kokjohn, Y. Moriyoshi, A. Agarwal, D. Arcoumanis, D. Assanis, C. Bae, K. Boulouchos, M. Canakci, S. Curran, I. Denbratt, M. Gavaises, M. Guenthner, C. Hasse, Z. Huang, T. Ishiyama, B. Johansson, T. Johnson, G. Kalghatgi, M. Koike, S. Kong, A. Leipertz, P. Miles, R. Novella, A. Onorati, M. Richter, S. Shuai, D. Siebers, W. Su, M. Trujillo, N. Uchida, B. M. Vaglieco, R. Wagner, H. Zhao, "IJER editorial: The Future of the Internal Combustion Engine," *International Journal of Engine Research,* 21 (2020), 3-10

[3] F. Un-Noor, S. Padmanaban, L. Mihet-Popa, M. N. Mollah, E. Hossain, "A Comprehensive Study of Key Electric Vehicle (EV) Components, Technologies, Challenges, Impacts, and Future Direction of Development," *Energies,* 10 (2017), 1217

[4] M. Mofijur, M. M. Hasan, T. M. I. Mahlia, S. M. A. Rahman, A. S. Silitonga, H. C. Ong, "Performance and Emission Parameters of Homogeneous Charge Compression Ignition (HCCI) Engine: A Review," *Energies,* 12 (2019), 3557

[5] T. Kuboyama, Y. Moriyoshi, T. Yamada, J. Takanashi, Y. Urata, K. Hatamura, "A Study of Newly Developed HCCI Engine With Wide Operating Range Equipped With Blowdown Supercharging System," *SAE International Journal of Engines,* 5 (2011), 51-66

[6] A. Nishiyama, M. K. Le, T. Furui, Y. Ikeda, "The Relationship between In-Cylinder Flow-Field near Spark Plug Areas, the Spark Behavior, and the Combustion Performance inside an Optical S.I. Engine," *Applied Sciences,* 9 (2019), 1545

[7] A. Nishiyama, M. K. Le, T. Furui, Y. Ikeda, "Simultaneous In-Cylinder Flow Measurement and Flame Imaging in a Realistic Operating Engine Environment Using High-Speed PIV," *Applied Sciences,* 9 (2019), 2678

[8] B. Peterson, E. Baum, A. Dreizler, B. Böhm, "An Experimental Study of the Detailed Flame Transport in a SI Engine Using Simultaneous Dual-plane OH-LIF and Stereoscopic PIV," *Combustion and Flame,* 202 (2019), 16-32

[9] S. Sayama, M. Kinoshita, Y. Mandokoro, T. Fuyuto, "Spark Ignition and Early Flame Development of Lean Mixtures under High-velocity Flow Conditions: An Experimental Study," *International Journal of Engine Research,* 20 (2018), 236-246

[10] R. N. Dahms, M. C. Drake, T. D. Fansler, T. W. Kuo, N. Peters, "Understanding Ignition Processes in Spray-guided Gasoline Engines Using High-speed Imaging and the Extended Spark-ignition Model SparkCIMM. Part A: Spark Channel Processes and the Turbulent Flame Front Propagation," *Combustion and Flame,* 158 (2011), 2229-2244

[11] R. N. Dahms, M. C. Drake, T. D. Fansler, T. W. Kuo, N. Peters, "Understanding Ignition Processes in Spray-guided Gasoline Engines using High-speed Imaging and the Extended Spark-ignition Model SparkCIMM: Part B: Importance of Molecular Fuel Properties in Early Flame Front Propagation," *Combustion and Flame,* 158 (2011), 2245-2260

[12] C. He, G. Kuenne, E. Yildar, J. van Oijen, F. di Mare, A. Sadiki, C.-P. Ding, E. Baum, B. Peterson, B. Böhm, J. Janicka, "Evaluation of the Flame Propagation within an SI Engine using Flame Imaging and LES," *Combustion Theory and Modelling,* 21 (2017), 1080-1113

[13] M. Günther, M. Sens, "Knocking in Gasoline Engines," *5th International Conference,* Berlin, Germany. Springer (2017)

[14] S. Shawal, M. Goschutz, M. Schild, S. Kaiser, M. Neurohr, J. Pfeil, T. Koch, "High-Speed Imaging of Early Flame Growth in Spark-Ignited Engines Using Different Imaging Systems via Endoscopic and Full Optical Access," *SAE International Journal of Engines,* 9 (2016), 704-718

[15] W. Zeng, C. A. Idicheria, T. D. Fansler, M. C. Drake, "Conditional Analysis of Enhanced Combustion Luminosity Imaging in a Spray-Guided Gasoline Engine with High Residual Fraction," SAE Technical Paper 2011-01-1281 (2011)

[16] R. Zhang, L. Chen, H. Wei, J. Pan, J. Li, P. Yang, R. Chen, "Optical study on the effects of the hydrogen injection timing on lean combustion characteristics using a natural gas/hydrogen dual-fuel injected spark-ignition engine," *International Journal of Hydrogen Energy,* 46 (2021), 20777-20789

[17] J. V. Pastor, A. García, C. Micó, F. Lewiski, "An optical investigation of Fischer-Tropsch diesel and Oxymethylene dimethyl ether impact on combustion process for CI engines," *Applied Energy,* 260 (2020), 114238

[18] B. Afkhami, Y. Wang, S. A. Miers, J. D. Naber, "Development of a turbulent burning velocity model based on flame stretch concept for SI engines," *Journal of the Energy Institute,* 93 (2020), 2444-2455

[19] S. J. Kazmouz, D. C. Haworth, P. Lillo, V. Sick, "Large-eddy simulations of a stratified-charge direct-injection spark-ignition engine: Comparison with experiment and analysis of cycle-to-cycle variations," *Proceedings of the Combustion Institute,* 38 (2021), 5849-5857

[20] V. Salazar, S. Kaiser, "Influence of the Flow Field on Flame Propagation in a Hydrogen-Fueled Internal Combustion Engine," *SAE Int. J. Engines,* 4 (2011), 2376-2394

[21] P. Sementa, B. M. Vaglieco, F. Catapano, "Thermodynamic and optical characterizations of a high performance GDI engine operating in homogeneous and stratified charge mixture conditions fueled with gasoline and bio-ethanol," (in English), *Fuel,* 96 (2012), 204-219

[22] K. Schänzlin, T. Koch, K. Boulouchos, "Characterization of the Combustion in a Direct Injection Spark Ignition Engine," SAE Technical Paper 2002-01-0834 (2002)

[23] S. A. Miers, H. Ng, S. A. Ciatti, K. Stork, "Emissions, Performance, and In-Cylinder Combustion Analysis in a Light-Duty Diesel Engine Operating on a Fischer-Tropsch, Biomass-to-Liquid Fuel," SAE Technical Paper 2005-01-3670 (2005)

[24] S.-C. Kong, L. M. Ricart, R. D. Reitz, "In-Cylinder Diesel Flame lmaging Compared with Numerical Computations," SAE Technical Paper 950455 (1995)

[25] P. L. Mtui, P. G. Hill, "Ignition Delay and Combustion Duration with Natural Gas Fueling of Diesel Engines," SAE Technical Paper 961933 (1996)

[26] J. Eismark, M. Balthasar, A. Karlsson, T. Benham, M. Christensen, I. Denbratt, "Role of Late Soot Oxidation for Low Emission Combustion in a Diffusion-controlled, High-EGR, Heavy Duty Diesel Engine," SAE Technical Paper 2009-01-2813 (2009)

[27] T. Shiozaki, H. Nakajima, Y. Kudo, A. Miyashita, Y. Aoyagi, "The Analysis of Combustion Flame Under EGR Conditions in a Dl Diesel Engine," SAE Technical Paper 960323 (1996)

[28] M. Bakenhus, R. D. Reitz, "Two-Color Combustion Visualization of Single and Split Injections in a Single-Cylinder Heavy-Duty D.I. Diesel Engine Using an Endoscope-Based Imaging System," SAE Technical Paper 1999-01-1112 (1999)

[29] U. Dierksheide, P. Meyer, T. Hovestadt, W. Hentschel, "Endoscopic 2D particle image velocimetry (PIV) flow field measurements in IC engines," *Experiments in Fluids,* 33 (2002), 794–800

[30] K.-M. Han, A. Velji, U. Spicher, "A New Approach for Three-Dimensional High-Speed Combustion Diagnostics in Internal Combustion Engines," SAE Technical Paper 2006-01-3315 (2006)

[31] T. Kato, K. Akiyama, T. Nakashima, R. Shimizu, "Development of Combustion Behavior Analysis Techniques in the Ultra High Engine Speed Range," SAE Technical Paper 2007-01-0643 (2007)

[32] S. Palaveev, H. Kubach, U. Spicher, M. Magar, R. Schiessl, U. Maas, "Premature Flame Initiation in a Turbocharged DISI Engine - Numerical and Experimental Investigations," *SAE International Journal of Engines,* 6 (2013), 54-66

[33] R. Reichle, C. Pruss, C. Gessenhardt, C. Schulz, W. Osten, "Diffractive/refractive (hybrid) UV-imaging system for minimally-invasive metrology: Design, performance, and application experiments," *Applied Optics,* 51 (2012), 1982-1996

[34] M. Goschütz, C. Schulz, S. A. Kaiser, "Endoscopic imaging of early flame propagation in a near-production engine," *SAE International Journal of Engines,* 7 (2014), 351-365

[35] C. Gessenhardt, C. Schulz, S. A. Kaiser, "Endoscopic temperature imaging in a four-cylinder IC engine via two-color toluene fluorescence," *Proceedings of the Combustion Institute,* 35 (2015), 3697–3705

[36] V. Weber, J. Brübach, R. L. Gordon, A. Dreizler, "Pixel-based characterisation of CMOS high-speed camera systems," *Applied Physics B,* 103 (2011), 421–433

[37] H. R. Ricardo, *Engines of high output: thermo-dynamic considerations*. Macdonald and Evans, 1926

[38] J. B. Heywood, *Internal combustion engine fundamentals*. New York, N.Y.: McGraw-Hill (in English), 1988

[39] J. A. Gatowski, E. N. Balles, K. M. Chun, F. E. Nelson, J. A. Ekchian, J. B. Heywood, "Heat release analysis of engine pressure data," SAE Technical Paper 841359 (1984)

[40] H. M. Cheung, J. B. Heywood, "Evaluation of a One-Zone Burn-Rate Analysis Procedure Using Production SI Engine Pressure Data," SAE Technical Paper 932749 (1993)

[41] K. M. Chun, J. B. Heywood, "Estimating Heat-Release and Mass-of-Mixture Burned from Spark-Ignition Engine Pressure Data," *Combustion Science and Technology,* 54 (1987), 133-143

[42] R. Ebrahimi, "Effect of specific heat ratio on heat release analysis in a spark ignition engine," *Scientia Iranica,* 18 (2011), 1231-1236

[43] G. Woschni, "A Universally Applicable Equation for the Instantaneous Heat Transfer Coefficient in the Internal Combustion Engine," *SAE Transactions,* 76 (1968), 3065-3083

[44] N. Ozdor, M. Dulger, E. Sher, "Cyclic Variability in Spark Ignition Engines A Literature Survey," *SAE Transactions,* 103 (1994), 1514-1552

[45] S. B. Han, "Cycle-to-cycle variations under cylinder-pressure-based combustion analysis in spark ignition engines," *KSME International Journal,* 14 (2000), 1151-1158

[46] J. C. Keck, J. B. Heywood, "Early Flame Development and Burning Rates in Spark Ignition Engines and Their Cyclic Variability," SAE Technical Paper 870164 (1987)

[47] P. G. Aleiferis, Y. Hardalupas, A. M. K. P. Taylor, K. Ishii, Y. Urata, "Flame chemiluminescence studies of cyclic combustion variations and air-to-fuel ratio of the

reacting mixture in a lean-burn stratified-charge spark-ignition engine," *Combustion and Flame,* 136 (2004), 72–90

[48] P. G. Aleiferis, A. M. K. P. Taylor, J. H. Whitelaw, K. Ishii, Y. Urata, "Cyclic Variations of Initial Flame Kernel Growth in a Honda VTEC-E Lean-Burn Spark-Ignition Engine," SAE Technical Paper 2000-01-1207 (2000)

[49] B. Krishna, J. Mallikarjuna, "Effect of Intake Manifold Orientation on In-Cylinder Tumble Flow Structure in an Internal Combustion Engine - An Analysis Using Particle Image Velocimetry," SAE Technical Paper 2009-28-0004 (2009)

[50] M. Wörner, G. Rottenkolber, "Voltage rise anemometry in turbulent flows applied to internal combustion engines," *Experiments in Fluids,* 62 (2021), 132

[51] D. Kim, L. Rao, H. Oh, S. Kook, "Endoscopic high-speed particle image velocimetry (eHS-PIV) in a high tumble production engine," *Experiments in Fluids,* 61 (2020), 219

[52] N. Peters, "The turbulent burning velocity for large-scale and small-scale turbulence," *Journal of Fluid Mechanics,* 384 (1999), 107-132

[53] J. F. Le Coz, "Cycle-to-Cycle Correlations Between Flow Field and Combustion Initiation in an S.I. Engine," *SAE Transactions,* 101 (1992), 954-966

[54] P. G. Aleiferis, A. M. K. P. Taylor, K. Ishii, Y. Urata, "The nature of early flame development in a lean-burn stratified-charge spark-ignition engine," *Combustion and Flame,* 136 (2004), 283–302

[55] K. Le Minh, T. Furui, A. Nishiyama, Y. Ikeda, "The Interaction of Flow-Field and Turbulence on Flame Development using High-Speed Combustion PIV," *Proceedings of the International Symposium on Diagnostics and Modeling of Combustion in Internal Combustion Engines,* 2017.9 (2017), B315

[56] Y. Wang, Zhang, J., Yang, Z., Wang, X. et al., "Investigation of Flow Conditions and Tumble near the Spark Plug in a DI Optical Engine at Ignition," SAE Technical Paper 2018-01-0208 (2018)

[57] N. Nishio, T. Aochi, N. Yokoo, K. Nakata, Y. Abe, K. Hanashi, "Design of a High Ignitability Spark Plug with a Flow Guide Plate," SAE Technical Paper 2015-01-0780 (2015)

[58] J. D. Smith, V. Sick, "A Multi-Variable High-Speed Imaging Study of Ignition Instabilities in a Spray-Guided Direct-Injected Spark-Ignition Engine," SAE Technical Paper 2006-01-1264 (2006)

[59] J. Kashdan, B. Thirouard, "Optical Engines as Representative Tools in the Development of New Combustion Engine Concepts," *Oil & Gas Science and Technology, Revue d IFP Energies nouvelles,* 66 (2011), 759-777

[60] J. Serras-Pereira, P. G. Aleiferis, D. Richardson, S. Wallace, "Mixture Preparation and Combustion Variability in a Spray-Guided DISI Engine," SAE Technical Paper 2007-01-4033 (2007)

[61] W. F. Colban, D. Kim, P. C. Miles, S. Oh, R. Opat, R. Krieger, D. Foster, R. P. Durrett, M. A. Gonzalez D, "A Detailed Comparison of Emissions and Combustion Performance Between Optical and Metal Single-Cylinder Diesel Engines at Low Temperature Combustion Conditions," *SAE International Journal of Fuels and Lubricants,* 1 (2009), 505-519

[62] P. Janas, M. Dias Ribeiro, A. Kempf, M. Schild, S. Kaiser, "Penetration of the Flame Into the Top-Land Crevice - Large-Eddy Simulation and Experimental High-Speed Visualization," SAE Technical Paper 2015-01-1907 (2015)

[63] J. A. Gatowski, J. B. Heywood, C. Deleplace, "Flame photographs in a spark-ignition engine," *Combustion and Flame,* 56 (1984), 71-81

[64] A. R. A. Aziz, Y. T. Anbese, F. Y. Hagos, M. R. Heikal, Firmansyah, "Characteristics of Early Flame Development in a Direct-Injection Spark-Ignition CNG Engine Fitted with a Variable Swirl Control Valve," *Energies,* 10 (2017), 964

[65] D. P. Sczomak, A. Zhao, M. S. Simon, Y. Zeng, "High Speed Endoscope Imaging to Supplement CFD Analysis and Combustion Testing for SIDI Engine Startup Development," SAE Technical Paper 2010-01-0347 (2010)

[66] A. Nauwerck, J. Gindele, U. Spicher, H. Rosskamp, G. Landwehr, "Investigation of the Transient In-Cylinder Flow Inside a Two Stroke Engine with Particle-Image-Velocimetry," SAE Technical Paper 2000-01-0902 (2000)

[67] D. Kim, L. Rao, S. Kook, H. Oh, S. W. Lee, H.-k. Baek, "Flow directed spark stretch and flame propagation in a high-tumble production engine," *International Journal of Engine Research,* 23, 2046–2059

[68] M. Kegalj, H.-P. Schiffer, "Endoscopic PIV measurements in a low pressure turbine rig," *Experiments in Fluids,* 47 (2009), 689

[69] Camera endoscope VIS 8 mm, LaVision GmbH. https://www.digitalimagecorrelation.com/en/products/enginemaster/endoscopes/index.php

[70] R. Yuan, J. Camm, T. Knight, M. Parker, S. Sogbesan, E. Long, V. Page, G. K. Hargrave, "Evaluation of in-cylinder endoscopic two-colour soot pyrometry of diesel combustion," *Combustion and Flame,* 242 (2022), 112207

[71] G. Mao, K. Shi, C. Zhang, S. Chen, P. Wang, "Experimental research on effects of biodiesel fuel combustion flame temperature on NOX formation based on endoscope high-speed photography," *Journal of the Energy Institute,* 93 (2020), 1399-1410

[72] K. Cung, S. Ciatti, S. Tanov, Ö. Andersson, "Low-Temperature Combustion of High Octane Fuels in a Gasoline Compression Ignition Engine," *Frontiers in Mechanical Engineering,* 3 (2017), 22

[73] AVL List GmbH. *Indicating and Combustion Development Tools*, 2009

[74] R. Reichle, C. Pruss, C. Gessenhardt, C. Schulz, W. Osten, "Diffractive/refractive (hybrid) UV-imaging system for minimally invasive metrology: design, performance, and application experiments," *Applied Optics,* 51 (2012)

[75] C. Gessenhardt, R. Reichle, C. Pruss, W. Osten, C. Schulz, "In-cylinder imaging diagnostics with highly efficient UV-transparent endoscopes," *7th International Symposium Towards Clean Diesel Engines*, Aachen, 5 (2009)

[76] C. Gessenhardt, F. Zimmermann, C. Schulz, R. Reichle, C. Pruss, W. Osten, "Endoscopic imaging LIF diagnostics in IC engines," *Proceedings of the European Combustion Meeting Vienna* (2009)

[77] R. Reichle, C. Pruss, W. Osten, H. J. Tiziani, F. Zimmermann, C. Schulz, "Hybrid excitation and imaging optics for minimal invasive multiple-band UV-LIF-measurements in engines," *VDI-Berichte 1959,* (2006), 223-235

[78] M. A. Shahbaz, M. Goschütz, S. A. Kaiser, "Endoscopic Anisole-LIF Imaging of Flame Propagation and Temperature Fluctuations in a Production SI Engine," *8th European Combustion Meeting,Dubrovnik* (2017)

[79] M. A. Shahbaz, S. A. Kaiser, M. Schütte, T. Berg, "Characterization of different endoscopic imaging systems in ultraviolet range for combustion applications," *Applied Optics,* 62 (2023), 4949-4957

[80] M. A. Shahbaz, N. Jüngst, R. Grzeszik, S. A. Kaiser, "Endoscopic fuel film, chemiluminescence, and soot incandescence imaging in a direct-injection spark-ignition engine," *Proceedings of the Combustion Institute,* 38 (2021), 5869-5877

[81] M. Vacher, I. Fdez Galván, B. W. Ding, S. Schramm, R. Berraud-Pache, P. Naumov, N. Ferré, Y. J. Liu, I. Navizet, D. Roca-Sanjuán, W. J. Baader, R. Lindh, "Chemi- and Bioluminescence of Cyclic Peroxides," (in eng), *Chemical Reviews,* 118 (2018), 6927-6974

[82] A. G. Gaydon, H. G. Wolfhard, "Mechanism of formation of CH, C2, OH and HCO radicals in flames," *Symposium (International) on Combustion,* 4 (1953), 211-218

[83] Y. Hidaka, S. Takahashi, H. Kawano, M. Suga, W. C. Gardiner, Jr., "Shock-tube measurement of the rate constant for excited hydroxyl(A2.SIGMA.+) formation in the hydrogen-oxygen reaction," *The Journal of Physical Chemistry,* 86 (1982), 1429-1433

[84] T. Kathrotia, U. Riedel, A. Seipel, K. Moshammer, A. Brockhinke, "Experimental and numerical study of chemiluminescent species in low-pressure flames," *Applied Physics B,* 107 (2012), 571-584

[85] M. Goschütz, C. Schulz, S. A. Kaiser, "Endoscopic Imaging of Early Flame Propagation in a Near-Production Engine," *SAE International Journal of Engines,* 7 (2014), 351-365

[86] R. Collin, J. Nygren, M. Richter, M. Aldén, L. Hildingsson, B. Johansson, "Simultaneous OH- and Formaldehyde-LIF Measurements in an HCCI Engine," SAE Technical Paper 2003-01-3218 (2003)

[87] S. H. R. Müller, B. Böhm, M. Gleißner, S. Arndt, A. Dreizler, "Analysis of the temporal flame kernel development in an optically accessible IC engine using high-speed OH-PLIF," *Applied Physics B,* 100 (2010), 447–452

[88] B. Peterson, E. Baum, B. Bohm, A. Dreizler, "Early flame propagation in a spark-ignition engine measured with quasi 4D-diagnostics," (in English), *Proceedings of the Combustion Institute,* 35 (2015), 3829-3837

[89] R. N. Dahms, M. C. Drake, T. D. Fansler, T.-W. Kuo, N. Peters, "Understanding Ignition Processes in Spray-guided Gasoline Engines using High-speed Imaging and the Extended Spark-ignition Model SparkCIMM: Part B: Importance of Molecular Fuel Properties in Early Flame Front Propagation," *Combustion and Flame,* 158 (2011), 2229–2244

[90] M. C. Drake, T.D. Fansler, K. H. Peterson, "Stratified Ignition Processes in Spray- Guided SIDI Engines," 9th International Symposium Internal Combustion Diagnostics, Baden-Baden, (2010)

[91] C. Gessenhardt, F. Zimmermann, C. Schulz, R. Reichle, C. Pruss, W. Osten, "Hybrid endoscopes for laser-based imaging diagnostics in IC engines," SAE Technical Paper 2009-01-0655 (2009)

[92] C. Gessenhardt, C. Meffert, S. A. Kaiser, C. Schulz, A. Birkigt, L. Beckmann, "Laser-based endoscopic high-speed diagnostics to visualize irregular combustion events in a near-production engine," *Proceedings of the European Combustion Meeting, Cardiff* (2011)

[93] M. Moslemin Koupaie, A. Cairns, J. Xia, H. Vafamehr, T. Lanzanova, "Cyclically resolved flame and flow imaging in an alcohol fuelled SI engine," *Fuel,* 237 (2019), 874-887

[94] X. Ma, Z. Wang, C. Jiang, Y. Jiang, H. Xu, J. Wang, "An optical study of in-cylinder CH2O and OH chemiluminescence in flame-induced reaction front propagation using high speed imaging," *Fuel,* 134 (2014),603-610

[95] M. Goschütz, M. Shahbaz, S. Shawal, S. Kaiser, "Endoscopic visualization of the early premixed flame kernel in an SI engine by high-speed chemiluminescence imaging and tracer-LIF," Congress Engine Combustion Processes, (2017)

[96] J. Laichter, S. A. Kaiser, "Optical Investigation of the Influence of In-cylinder Flow and Mixture Inhomogeneity on Cyclic Variability in a Direct-Injection Spark Ignition Engine," *Flow, Turbulence and Combustion,* (2022)

[97] B. Peterson, D. L. Reuss, V. Sick, "On the ignition and flame development in a spray-guided direct-injection spark-ignition engine," *Combustion and Flame,* 161 (2014), 240-255

[98] M. A. Attar, H. Zhao, M. R. Herfatmanesh, A. Cairns, "Turbulent flame boundary and structure detection in an optical DISI engine using tracer-based two-line PLIF technique," *Experimental Thermal and Fluid Science,* 68 (2015), 545-558

[99] R. J. Adrian, "Scattering particle characteristics and their effect on pulsed laser measurements of fluid flow: speckle velocimetry vs particle image velocimetry," *Applied Optics,* 23 (1984), 1690-1691

[100] C. E. Willert, M. Gharib, "Digital particle image velocimetry," *Experiments in Fluids,* 10 (1991), 181-193

[101] F. T. Nieuwstadt, *Flow visualization and image analysis*. Springer Science & Business Media, 2012

[102] Measurement Principles of PIV, Dantec Dynamics A/S. https://www.dantecdynamics.com/solutions/fluid-mechanics/particle-image-velocimetry-piv/measurement-principles-of-piv/

[103] W. Thielicke, E. Stamhuis, "PIVlab–towards user-friendly, affordable and accurate digital particle image velocimetry in MATLAB," *Journal of open research software,* 2 (2014)

[104] W. Thielicke, R. Sonntag, "Particle Image Velocimetry for MATLAB: Accuracy and Enhanced Algorithms in PIVlab," *Journal of open research software,* 9 (2021)

[105] H. Ben-Gida, R. Gurka, A. Liberzon, "OpenPIV-MATLAB — An open-source software for particle image velocimetry; test case: Birds' aerodynamics," *SoftwareX,* 12 (2020)

[106] Y. Yu, C. Wang, Q. Fu, R. Kou, F. Huang, B. Yang, T. Yang, M. Gao, "Techniques and Challenges of Image Segmentation: A Review," *Electronics,* 12 (2023), 1199

[107] M. Costa, D. Piazzullo, U. Sorge, S. Merola, A. Irimescu, V. Rocco, "Image Processing for Early Flame Characterization and Initialization of Flamelet Models of Combustion in a GDI Engine," SAE Technical Paper 2015-24-2405 (2015)

[108] I. Bankman, *Handbook of medical image processing and analysis*. Elsevier, 2008

[109] F. Merchant, K. Castleman, *Microscope image processing*. Academic press, 2022

[110] N. Otsu, "A Threshold Selection Method from Gray-Level Histograms," *IEEE Transactions on Systems, Man, and Cybernetics,* 9 (1979), 62-66

[111] J. Canny, "A Computational Approach to Edge Detection," *IEEE Transactions on Pattern Analysis and Machine Intelligence,* PAMI-8 (1986), 679-698

[112] I. Sobel, G. M. Feldman, "An Isotropic 3×3 image Gradient Operator for Image Processing," *Pattern Classification and Scene Analysis,* (1973), 271-272

[113] J. M. S. Prewitt, "Parametric and Nonparametric Recognition by Computer: An Application to Leukocyte Image Processing," *Advances in Computers,* 12 (1972), 285-414

[114] R. Gonzalez, R. Woods, *Digital image processing. An imprint of Pearson Education*. Addison-Wesley, 2002

[115] Alan Todd, Alasdair Cairns, Hermann Hoffman, Pavlos Aleiferis, J. Malcolm, "An Optical Study of Spray Development and Combustion of Ethanol, Iso-Octane and Gasoline Blends in a DISI Engine," SAE Technical Paper 2008-01-0073 (2008)

[116] A. Hanuschkin, S. Zündorf, M. Schmidt, C. Welch, J. Schorr, S. Peters, A. Dreizler, B. Böhm, "Investigation of cycle-to-cycle variations in a spark-ignition engine based on a machine learning analysis of the early flame kernel," *Proceedings of the Combustion Institute,* 38 (2021), 5751-5759

[117] S. K. Chen, A. Mandal, L.-C. Chien, E. Ortiz-Soto, "Machine Learning for Misfire Detection in a Dynamic Skip Fire Engine," *SAE International Journal of Engines,* 11 (2018), 965-976

[118] C. Gessenhardt, "Endoskopische Bestimmung des Temperaturfeldes im Brennraum eines Ottomotors mittels laserinduzierter Fluoreszenz," PhD Thesis, University of Duisburg-Essen: Duisburg, 2013

[119] M. Goschütz, S. Shawal, M. Schild, C. Schulz, S. Kaiser, "Comparison of flame-front visualization in internal combustion engines using different imaging systems via endoscopic and full optical access," *Proceedings of the European Combustion Meeting,* (2015)

[120] S. Shawal, J. Saedon, M. S. Meon, N. H. Mohamad, H. Husain, M. Mahat, M. R. M. Nawi, "A comparative study of various binarization schemes for flame-front detection in a S.I engine," *IOP Conference Series: Materials Science and Engineering,* 834 (2020)

[121] S. Shawal, M. Krzanowski , S. A. Kaiser, "Improved imaging and post-processing of early combustion in a spark-ignition engine via endoscopic high-speed imaging," *Proceedings of the European Combustion Meeting, Dubrovnik* (2017)

[122] S. Shawal, M. S. Meon, J. B. Saedon, M. F. Remeli, N. H. Mohamad Nor, S. A. Kaiser, "Imaging and Post-Processing of Early Combustion in a Spark- Ignition Engine via Endoscopic Access," *Journal of Mechanical Engineering,* SI 9 (2020), 217-227

[123] L. Engelmann, J. Laichter, P. Wollny, M. Klein, S. A. Kaiser, A. M. Kempf, "Cyclic Variations in the Flame Propagation in an Spark-Ignited Engine: Multi Cycle Large Eddy Simulation Supported by Imaging Diagnostics," *Flow, Turbulence and Combustion,* 110 (2023), 91-104

[124] L. Petrucci, F. Ricci, F. Mariani, G. Discepoli, "A Development of a New Image Analysis Technique for Detecting the Flame Front Evolution in Spark Ignition Engine under Lean Condition," *Vehicles,* 4 (2022), 145-166

[125] P. G. Aleiferis, A. M. K. P. Taylor, K. Ishii, Y. Urata, "The nature of early flame development in a lean-burn stratified-charge spark-ignition engine," *Combustion and Flame,*136 (2004), 283–302

[126] W. W. Pulkrabek, *Engineering Fundamentals of the Internal Combustion Engine (2nd Edition)*. Prentice Hall, 2003

[127] V. M. Salazar, "Unburned hydrocarbon emission mechanisms in small engines," PhD Thesis, University of Wisconsin-Madison, 2009

[128] J. Borée, S. Maurel, R. Bazile, "Disruption of a compressed vortex," *Physics of Fluids,*14 (2002), 2543-2556

[129] R. Stiehl, J. Bode, J. Schorr, C. Krüger, A. Dreizler, B. Böhm, "Influence of intake geometry variations on in-cylinder flow and flow–spray interactions in a stratified direct-injection spark-ignition engine captured by time-resolved particle image velocimetry," *International Journal of Engine Research,*17 (2016), 983-997

Author contributions

This thesis contains work that I jointly contributed together with other authors. My contributions to each publication are stated below, using the CRediT system (https://www.elsevier.com/researcher/author/policies-and-guidelines/credit-author-statement).

1. S. Shawal, M. Goschütz, M. Schild, S. Kaiser, M. Neurohr, J. Pfeil, and T. Koch, "High-Speed Imaging of Early Flame Growth in Spark-Ignited Engines Using Different Imaging Systems via Endoscopic and Full Optical Access," *SAE Int. J. Engines,* vol. 9 (2016), pp. 704-718 [14]

S. Shawal: Software, Formal analysis, Writing – original draft

2. S. Shawal, M. Krzanowski, and S. A. Kaiser, "Improved Imaging and Post-Processing of Early Combustion in a Spark-Ignition Engine via Endoscopic High-Speed Imaging," *Proceedings of the European Combustion Meeting, Dubrovnik* (2017) [121]

S. Shawal: Investigation, Formal analysis, Writing – original draft

3. M. Goschütz, S. Shawal, M. Schild, C. Schulz, and S. Kaiser, "Comparison of Flame-Front Visualization in Internal Combustion Engines Using Different Imaging Systems Via Endoscopic and Full Optical Access," *Proceedings of the European Combustion Meeting, Budapest* (2015) [119]

S. Shawal: Software, Formal analysis, Writing – original draft

4. M. Goschütz, M. Shahbaz, S. Shawal, and S. Kaiser, "Endoscopic Visualization of The Early Premixed Flame Kernel in An SI Engine By High-Speed Chemiluminescence Imaging And Tracer-LIF," *Congress Engine Combustion Processes, Ludwigsburg* (2017) [95]

S. Shawal: Formal analysis, Resources

5. S. Shawal, J. Saedon, M. S. Meon, N. H. Mohamad, H. Husain, M. Mahat, M. R. M. Nawi, "A comparative study of various binarization schemes for flame-front detection in a S.I engine," *IOP Conference Series: Materials Science and Engineering,* vol. 834 (2020) [120]

S. Shawal: Investigation, Formal analysis, Writing – original draft

6. S. Shawal, M. S. Meon, J. B. Saedon, M. F. Remeli, N. H. Mohamad Nor, S. A. Kaiser, "Imaging and Post-Processing of Early Combustion in a Spark- Ignition Engine via Endoscopic Access," *Journal of Mechanical Engineering,* vol. SI 9 (2020), pp. 217-227 [122]

S. Shawal: Investigation, Formal analysis, Writing – original draft

DOI: 10.17185/duepublico/82249
URN: urn:nbn:de:hbz:465-20240814-143020-1